Stability analysis and transition prediction of wall-bounded flows.

by

Ori Levin

Dec 2003
Technical Reports from
KTH Mechanics
SE-100 44 Stockholm, Sweden

Typsatt i $\mathcal{A}\mathcal{M}\mathcal{S}$-LaTeX.

Akademisk avhandling som med tillstånd av Kungliga Tekniska Högskolan i Stockholm framlägges till offentlig granskning för avläggande av teknologie licentiatexamen onsdagen den 17:e december 2003 kl 10.15 i sal E3, Huvudbyggnaden, Kungliga Tekniska Högskolan, Osquars Backe 14, Stockholm.

Universitetsservice US-AB, Stockholm 2003

Till minne av Jonna

Må du vila i ro

Stability analysis and transition prediction of wall-bounded flows.

Ori Levin 2003
KTH Mechanics
SE-100 44 Stockholm, Sweden.

Abstract

Disturbances introduced in wall-bounded flows can grow and lead to transition from laminar to turbulent flow. In order to reduce losses or enhance mixing in energy systems, a fundamental understanding of the flow stability is important. In low disturbance environments, the typical path to transition is an exponential growth of modal waves. On the other hand, in large disturbance environments, such as in the presence of high levels of free-stream turbulence or surface roughness, algebraic growth of non-modal streaks can lead to transition. In the present work, the stability of wall-bounded flows is investigated by means of linear stability equations valid both for the exponential and algebraic growth scenario. An adjoint-based optimization technique is used to optimize the algebraic growth of streaks. The exponential growth of waves is maximized in the sense that the envelope of the most amplified eigenmode is calculated. Two wall-bounded flows are investigated, the Falkner–Skan boundary layer subject to favorable, adverse and zero pressure gradients and the Blasius wall jet. For the Falkner–Skan boundary layer, the optimization is carried out over the initial streamwise location as well as the spanwise wave number and the angular frequency. Furthermore, a unified transition-prediction method based on available experimental data is suggested. The Blasius wall jet is matched to the measured flow in an experimental wall-jet facility. Linear stability analysis with respect to the growth of two-dimensional waves and streamwise streaks are performed and compared to the experiments. The nonlinear interaction of introduced waves and streaks and the flow structures preceding the flow breakdown are investigated by means of direct numerical simulations.

Descriptors: Boundary layer, wall jet, algebraic growth, exponential growth, *lift-up* effect, streamwise streaks, Tollmien-Schlichting waves, free-stream turbulence, roughness element, transition prediction, Parabolized Stability Equations, Direct Numerical Simulation.

Preface

This thesis considers the study of exponentially growing waves and algebraically growing streaks in wall-bounded flows. The thesis is divided in two parts, the first part is a short introduction to the field and a summary of the two following papers. The papers are re-set in the present thesis format and included in the second part of the thesis.

Paper 1. Levin, 0., & Henningson, D. S. 2003 Exponential vs Algebraic Growth and Transition Prediction in Boundary Layer Flow. *to appear in Flow, Turbulence and Combustion*.

Paper 2. Levin, 0., Chernoray, V. G., Litvinenko, M. V., Löfdahl, L. & Henningson, D. S. 2003 A numerical and experimental study of the Blasius wall jet. *submitted to Journal of Fluid Mechanics*.

Division of work between authors

The first paper deals with the energy growth of eigenmodes and non-modal optimal disturbances in the Falkner–Skan boundary layer with favorable, adverse and zero pressure gradients. The numerical codes are based on already existing codes at KTH Mechanics (DM). The numerical implementations needed for this work was performed by Ori Levin (OL). The theory and writing was done by OL with help from Dan Henningson (DH).

The second paper is a numerical and experimental study of the stability of the Blasius wall jet. The work is a cooperation between DM and Thermo and Fluid Dynamics at Chalmers University of Technology (TFD). The numerical codes for the linear analysis are the same as for the first paper with new subroutines for the base flow. The Direct Numerical Simulations were performed with a numerical code, already in use for many research projects. The code is based on a pseudo-spectral technique and is developed originally by Anders Lundbladh and DH at DM. The numerical implementations needed for this work was performed by OL with the help of Mattias Chevalier. The experimental work was done by Valery Chernoray (VC) and Maria Litvinenko (ML) at TFD. The writing was done by OL, VC and ML with the help of Lennart Löfdahl (LL) and DH.

Contents

Part 1

Summary

CHAPTER 1

Introduction

A solid material possesses the property of rigidity, implying that it can withstand moderate shear stress without a permanent deformation. A true fluid, on the other hand, is by definition a material with no rigidity at all. Subjected to shear stress, no matter how small this stress may be, a fluid is bound to continuously deform. The fluids that all of us are most familiar with are water and air. Water is a liquid, while air is a gas, but that distinction is less important than might be imagined when it comes to fluid dynamics.

A fluid flow is usually defined as either laminar or turbulent. The laminar flow is characterized by an ordered, layered and predictable motion while the turbulent state consists of a chaotic, swirly and fluctuating motion. The difference between the two kinds of motions can easily be visualized in the kitchen while poring water from the tap. If the tap is opened only a bit, the water that flows from the faucet will be smooth and glassy, because the flow is laminar. When the tap is opened further, the flow speed increases and the water all of a sudden becomes white with small bubbles, accompanied by a louder noise. The water flow has then become irregular and turbulent and air is mixed into it. The same phenomenon can be seen in the smoke streaming upward into still air from a burning cigarette. Immediately above the cigarette, the flow is laminar. A little higher up, it becomes rippled and diffusive as it becomes turbulent.

The two above everyday examples illustrate the effect of flow speed and distance on the cause of turbulence. As the flow velocity or the characteristic length of the flow problem increases, small disturbances introduced in the flow amplify and the laminar flow break down to turbulence. This phenomenon is called *transition*. There is one more quantity affecting the state of the flow, namely the viscosity of the fluid. For sufficiently large viscosity, motions that would cause turbulence are damped out and the flow stays laminar.

The basic difference between laminar and turbulent flows was dramatically demonstrated by Osborne Reynolds in a classical experiment at the hydraulics laboratory of the Engineering Department at Manchester University. Reynolds (1883) studied the flow inside a glass tube by injecting ink at the centerline of the pipe inlet. At low flow rates, the flow stayed laminar and the dye stream was observed to follow a well-defined straight path inside the tube. As the flow rate was increased, at some point in the tube, the dye streak broke up into a turbulent motion and spread throughout the cross section of the tube.

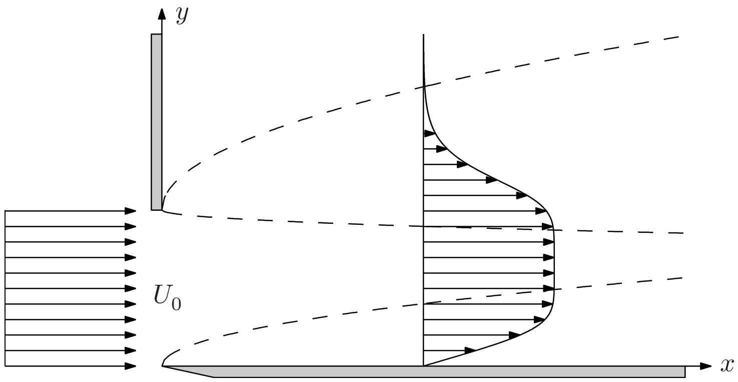

FIGURE 1.1. Wall bounded and free shear layer flow that together form a wall jet.

He found that the value of a dimensionless parameter, now called Reynolds number, $Re = Ud/\nu$, where U is the mean velocity of the water through the tube, d the diameter of the tube and ν the kinematic viscosity of the water, governs the transition from laminar to turbulent flow. Reynolds made it quite clear, however, that there is no single *critical* value of Re, above which the flow becomes unstable and transition may occur. The whole matter is much more complicated and very sensitive to disturbances from the surroundings entering the pipe inlet. In fact, transition and its triggering mechanisms are even today not fully understood.

In a laminar flow, the shear stresses are smaller than in a turbulent flow and as a consequence, the friction drag over the surface of a wing is much lower. On the other hand, a laminar flow can not stay attached to the wing surface as far downstream as a turbulent flow since the pressure increases downstream. Instead, laminar separation occurs resulting in the formation of a wake and increased pressure drag. However, for a turbulent flow, separation is delayed due to the mixing provided of the chaotic motion and the total drag force decreases. That is also the reason why golf balls have dimples over the surface, to enforce turbulence and a smaller wake behind it. Due to the excellent mixing of a turbulent flow, it is required in chemical reactors and combustion engines. In some applications, it is important to keep the flow laminar and in others to enforce turbulence. Therefore an increased understanding of the triggering mechanisms of transition from laminar to turbulent flow and its foregoing amplification of introduced disturbances is important.

For transition to take place, some part of the flow has to be unstable to introduced disturbances. Such flows usually possess some kind of velocity shear, like the boundary layer and the free shear layer shown in figure 1.1. The boundary layer is the flow, in the lower part of the figure, over the horizontal flat plate subjected to a uniform oncoming flow with velocity U_0. Due to viscosity, the flow velocity varies from zero at the wall to the free-stream velocity a distance of the boundary layer thickness above the wall. The free shear layer, in the upper part of the figure, evolves from the difference in the streamwise velocity below the vertical wall and behind it. The streamwise velocity varies from the maximum velocity U_0 below the shear flow to zero above it. The thickness of the shear layers grow as the flow develops downstream. The combined flow field in figure 1.1 and the downstream interaction of the shear layers is defined as a wall jet.

The whole transition process consists of three stages: receptivity, disturbance growth and breakdown. In the *receptivity* stage, disturbances are initiated in the part of the flow where velocity shear is present. Typical sources from which disturbances can enter the shear flow are free-stream vortical structures, free-stream turbulence, acoustic waves, and for the case of wall-bounded shear flows, surface roughness and vibrations. Once a disturbance is introduced in the shear flow, it may *grow* or decay according to the stability characteristics of the base flow. When the disturbances are yet small compared to the base flow, one can study linearized stability equations to determine the disturbance growth. In fact, the linear mechanisms are responsible for any disturbance energy growth, while the nonlinear effects only redistribute energy among different frequencies and scales of the flow (Henningson 1996). As the disturbances amplifies, nonlinear effects starts to be important and the base-flow distortion begins to be apparent. The disturbances usually saturate when they have reached a large enough amplitude and a new laminar base flow, which usually is unstable to new disturbances, is established. In this stage, the usually rapid final nonlinear *breakdown* begins, followed by a multitude of scales and frequencies typical for a turbulent flow.

CHAPTER 2

Small disturbances

2.1. Time-periodic waves

The prediction of the stability of a given flow and the amplification of small disturbances have been of interest to the fluid dynamics community for more than a century. An equation for the evolution of a disturbance, linearized around a mean velocity were first derived by Reyleigh (1980) for parallel inviscid flow. He also derived the criterion that for an unstable mode to exist in an inviscid flow, the mean velocity profile has to possess an inflection point. Fjørtoft (1950) later derived that a necessary condition for instability is that the inflection point has to be a maximum (rather than a minimum) of the shear stress. The traditional stability-analysis technique for viscous flow, independently derived by Orr (1907) and Sommerfeld (1908), is to solve the eigenvalue problem of the Orr–Sommerfeld equation, which is the linearized stability equation based on the assumption of parallel flow with wave-like disturbances. The unstable eigenmodes are historically referred to as Tollmien–Schlichting (TS) waves, after the work by Tollmien (1929) and Schlichting (1933), usually taking the form of exponentially growing two-dimensional waves. In fact, Squire (1933) stated that parallel shear flows first become unstable to two-dimensional waves at a value of the Reynolds number that is smaller than any value for which unstable three-dimensional waves exist. The stability of such waves depends on their frequency and the Reynolds number of the flow.

The first successful experimental study of TS-waves was carried out by Schubauer & Skramstad (1947) who showed that wave disturbances may occur naturally in a Blasius boundary layer on a flat plate. The streamwise amplitude function of TS-waves in boundary layers has one large peak in the boundary layer and one smaller peak in the free stream. For wall jets, one more peak can be found. The temporal linear stability of a wall jet was examined theoretically by Chun & Schwarz (1967) by solving the Orr–Sommerfeld equation. The streamwise velocity fluctuation was found to exhibit two large peaks, one peak on each side of the wall-jet core and one smaller peak in the ambient flow. Bajura & Szewczyk (1970) performed hot-wire measurements in an air wall jet and found that the amplification rate of the outer peak is larger, and hence, the instability of the wall jet is controlled by the outer region. By solving the Orr–Sommerfeld equation, Mele *et al.* (1986) clarified the existence of two unstable modes in the wall jet. One mode, unstable at low disturbance frequencies, shows the highest amplitude close to the inflection point in the outer region of the wall jet, while the other mode, unstable at higher frequencies, attains the highest amplitude close to the wall. They concluded that the inviscid instability in the outer region governs the large-scale disturbances while the viscous instability governs the small-scale disturbances close to the wall. Tumin & Aizatulin (1997) numerically investigated the instability and receptivity of a laminar wall jet and concluded that the high-frequency viscous mode can be exited more easily by periodic blowing and suction through the wall than the low-frequency inviscid mode.

The drawback of the assumption of parallel flow in the Orr–Sommerfeld problem is that it does not account for the growth of the thickness of a shear layer as the flow develops downstream. The idea of solving the parabolic evolution of disturbances in non-parallel boundary layers was first introduced by Floryan & Saric (1979) and later also by Hall (1983) for steady Görtler vortices. Bertolotti *et al.* (1992) developed the method of parabolic evolution of eigenmodes in boundary layers and derived the parabolized stability equations (PSE). The method is computationally very fast and has been shown to be in excellent agreement with direct numerical simulations (DNS) of the Navier–Stokes equations and experiments (see e.g. Hanifi 1995).

2.2. Steady streaks

In low disturbance environments, the transition is usually preceded by the exponential growth and breakdown of TS-waves. However, exponential instability involving unstable eigenmodes is not the only transition scenario. For a sufficiently large disturbance amplitude, algebraic non-modal growth can lead to so-called bypass-transition, not associated with exponential instabilities. At a moderate or high lever of free-stream turbulence, many experiments have observed streaky structures, taking the form of elongated streamwise structures with narrow spanwise scales and much larger streamwise scales. This type of disturbance is historically denoted as the Klebanoff mode after the boundary-layer experiments of Klebanoff (1971). More recent experiments displaying streaky structures in boundary layers, subject to various levels of free-stream turbulence, have been performed by e.g. Westin *et al.* (1994) and Matsubara & Alfredsson (2001). Ellingsen & Palm (1975) performed linear stability analysis of inviscid channel flow. They showed that finite three-dimensional disturbances without streamwise variation can lead to instability, even though the basic velocity does not possess any inflection point. The instability leads to an increase linearly with time of the streamwise disturbances, producing alternating low and high velocity streaks. Landahl (1980) demonstrated that all parallel inviscid shear flows can be unstable to three-dimensional disturbances, which lead to a growth of the disturbance energy at least as fast as linearly in time. The physical interpretation of the formation of the streaks is the lift-up effect, i.e. that fluid elements initially retain their horizontal momentum when displaced in the wall-normal direction, hence causing a streamwise disturbance. Andersson *et al.* (1999) solved the linear stability equations for the Blasius boundary layer, taking the non-parallel effects into account, to optimize the input disturbance at the leading edge giving rise to the largest disturbance energy gain at the final downstream location. By going to the limit of large Reynolds number, it was shown that the optimal initial disturbance consists of a streamwise vortex developing into streamwise streaks with zero frequency. The results agreed remarkably well with experimental data produced by Westin *et al.* (1994), irrespective of the absent optimization procedure in the experiments.

2.3. Disturbance equations

Waves and streaks are associated with different scales. Waves propagating in the downstream direction have a wave length in the order of the thickness of the shear layer while streaks usually have much larger streamwise scales. The result is that the corresponding frequency is much larger for waves than for streaks. The associated spanwise scales are the opposite with narrow scales for the streaks and much larger scales for the waves. Yet, the exponential growth of waves and the algebraic growth of streaks can be described by a common set of stability equations.

2.3.1. *Scaling*

Consider an incompressible wall-bounded flow over a flat plate, such as the boundary layer and the wall jet illustrated in figure 1.1. Fluid is blown tangentially along a wall. The scalings are originating from the boundary-layer approximations. The streamwise coordinate x is scaled with the length scale l, which is a fixed distance from the leading edge of the wall. The wall-normal and spanwise coordinates y and z, respectively, are scaled with the boundary-layer parameter $\delta = \sqrt{\nu l / U_l}$, where ν is the kinematic viscosity of the fluid and U_l is the undisturbed streamwise velocity in the free stream above the boundary layer and in the wall jet core, at the location l. In the case of a boundary layer without a pressure gradient, the free-stream velocity is constant, thus $U_l = U_0$, where U_0 is the free-stream velocity at the leading edge. The streamwise velocity U is scaled with U_l, while the wall-normal and spanwise velocities V and W, respectively, are scaled with $U_l \delta / l$. The pressure P is scaled with $\rho U_l^2 \delta^2 / l^2$, where ρ is the density of the fluid, and the time t is scaled with l / U_l. The Reynolds numbers used here are defined as $Re_l = U_l l / \nu$ and $Re_\delta = U_l \delta / \nu$. It is useful to note the relations $l / \delta = Re_\delta = \sqrt{Re_l}$.

2.3.2. *Linear disturbance equations*

We want to study the linear stability of a flow at high Reynolds number. The non-dimensional Navier–Stokes equations for an incompressible flow are linearized around a two-dimensional, steady base flow $\big(U(x,y),\ V(x,y),\ 0\big)$ to obtain the stability equations for the spatial evolution of three-dimensional, time-dependent disturbances $\big(u(x,y,z,t), v(x,y,z,t), w(x,y,z,t), p(x,y,z,t)\big)$. The disturbances, that are scaled as the base flow, are taken to be periodic in the spanwise direction and in time and are decomposed into a weak varying amplitude function and a phase function

$$\boldsymbol{f} = \hat{\boldsymbol{f}}(x,y)\exp\Big(\mathrm{i}Re_\delta\int_{x_0}^{x}\alpha(x)\,dx + \mathrm{i}\beta z - \mathrm{i}\omega t\Big), \tag{2.1}$$

where $\boldsymbol{f} = (u,v,w,p)^T$. The complex streamwise wave number α captures the fast wave-like variation of the modes and is therefore scaled with $1/\delta$ and α itself is assumed to vary slowly with x. The real spanwise wave number β and the real disturbance angular frequency ω are scaled in a consistent way with z and t, respectively. By introducing (2.1) in the linearized Navier–Stokes equations, the parabolized stability equations in boundary-layer scalings can be written

$$\frac{\partial\hat{\boldsymbol{f}}}{\partial x} = \mathcal{L}\hat{\boldsymbol{f}}, \tag{2.2}$$

where $\mathcal{L}$ is a linear operator. The initial conditions and the boundary conditions are specified for the disturbance velocities. The boundary conditions are, no-slip conditions at the wall and homogeneous conditions far above the wall. The state equation (2.2) is integrated in the downstream direction from the location x_0, where initial conditions are specified, to the location x_1. The solution may be written in an input-output formulation

$$\hat{\boldsymbol{f}}_1 = \mathcal{A}\hat{\boldsymbol{f}}_0, \tag{2.3}$$

where $\mathcal{A}$ is a linear operator. The disturbance growth is generally measured by the average change in the kinetic energy of the fluid. In spatially evolving investigations, a commonly used quantity to represent this change is the disturbance energy defined as

$$E(x,\beta,\omega,Re_l) = \int_0^\infty\big(Re_l|u|^2 + |v|^2 + |w|^2\big)\,\mathrm{d}y. \tag{2.4}$$

2.3.3. *Exponential growth*

Consider solutions to (2.2) associated with wave-like disturbances, i.e. where α in the phase function is order unity. As both the amplitude function and the phase function depend on x, one more equation is required. We require both the amplitude function and the wave number α to change slowly in the streamwise direction, and specify a normalization condition on the amplitude function

$$\int_0^\infty\big(Re_l\overline{\hat{u}}\hat{u}_x + \overline{\hat{v}}\hat{v}_x + \overline{\hat{w}}\hat{w}_x\big)\,\mathrm{d}y = 0, \tag{2.5}$$

where the bar denotes complex conjugate. Other conditions are possible and are presented in the paper by Bertolotti *et al.* (1992). The normalization condition specifies how much growth and sinusoidal variation are represented by the amplitude function and the phase function, respectively. The initial condition is taken as the least stable eigenfunction from parallel theory with corresponding eigenvalue $\alpha(x_0)$. The exponential growth is maximized in the sense that the envelope of the most amplified eigenmode is calculated.

2.3.4. *Optimal disturbances*

Consider solutions to (2.2) with weak streamwise variations. Since the amplitude function captures weak variations, the streamwise wave number is set to zero. We are interested of maximizing the disturbance energy (2.4), in the downstream location x_1 by optimizing the initial disturbance in the initial location x_0 with given initial energy. That is, we want to maximize the disturbance growth

$$G(x_0, x_1, \beta, \omega, Re_l) = \frac{E(x_1)}{E(x_0)}. \tag{2.6}$$

The optimization procedure is based on the adjoint equation to the state equation (2.2). By multiplying an adjoint state vector $\boldsymbol{g}$ by the state equation and integrating by parts

$$\int_{x_0}^{x_1}\int_0^{\infty} \boldsymbol{g}^T \left(\frac{\partial \hat{\boldsymbol{f}}}{\partial x} - \mathcal{L}\hat{\boldsymbol{f}} \right) \mathrm{d}y\,\mathrm{d}x = \mathrm{BT} - \int_{x_0}^{x_1}\int_0^{\infty} \hat{\boldsymbol{f}}^T \left(\frac{\partial \boldsymbol{g}}{\partial x} + \mathcal{L}^*\boldsymbol{g} \right) \mathrm{d}y\,\mathrm{d}x, \tag{2.7}$$

the adjoint equation follows

$$-\frac{\partial \boldsymbol{g}}{\partial x} = \mathcal{L}^*\boldsymbol{g}, \tag{2.8}$$

where $\mathcal{L}^*$ denotes the adjoint operator to $\mathcal{L}$. The appropriate boundary conditions and initial conditions to the adjoint state equation (2.8) follows from the boundary terms BT and are specified in paper 1. The adjoint state equation is integrated in the upstream direction and the solution may be written

$$\boldsymbol{g}_0 = \mathcal{A}^*\boldsymbol{g}_1, \tag{2.9}$$

where $\mathcal{A}^*$ denotes the adjoint operator to $\mathcal{A}$. The maximum growth, where the energy is evaluated as an inner product, can be written

$$G_{\max} = \max \frac{(\hat{\boldsymbol{f}}_1, \hat{\boldsymbol{f}}_1)}{(\hat{\boldsymbol{f}}_0, \hat{\boldsymbol{f}}_0)} = \max \frac{(\mathcal{A}^*\mathcal{A}\hat{\boldsymbol{f}}_0, \hat{\boldsymbol{f}}_0)}{(\hat{\boldsymbol{f}}_0, \hat{\boldsymbol{f}}_0)}, \tag{2.10}$$

and is attained as the largest eigenvalue of the eigenvalue problem

$$\mathcal{A}^*\mathcal{A}\hat{\boldsymbol{f}}_0 = G\hat{\boldsymbol{f}}_0 \tag{2.11}$$

The most natural attempt to calculate the optimal initial disturbance and its associated maximum growth is by power iterations

$$\hat{\boldsymbol{f}}_0^{n+1} = \mathcal{A}^*\mathcal{A}\hat{\boldsymbol{f}}_0^{n}, \tag{2.12}$$

where the initial disturbance is scaled to the given initial energy in each iteration. For a high Reynolds number flow, a Reynolds-number-independent growth can be defined to simplify the optimization procedure

$$\overline{G} = \lim_{Re_l \to \infty} \frac{G}{Re_l} \tag{2.13}$$

In the limit of large Reynolds number, the maximum growth will be obtained for initial disturbances with a zero streamwise component resulting in streamwise streaks with negligible cross-flow components. See paper 1 for details.

2.4. Application to the Falkner–Skan boundary layer

In the first paper, the stability of the Falkner–Skan boundary layer to exponentially growing waves and non-modal streaks is analyzed. A comparison of the algebraic growth with the exponential growth is performed and a unified transition-prediction method based on available experimental data is suggested.

2.4.1. *Comparison of algebraic and exponential growth*

Linear stability analysis is performed with the Falkner–Skan boundary layer as the base flow. The acceleration of the free-stream velocity driven by the pressure gradient is described by the Hartree parameter β_H in the formulation of the similarity solution. The stability of optimal disturbances and exponentially growing waves is examined for three base flows with favorable, adverse and zero pressure gradients. The corresponding Hartree parameters are $\beta_H = 0.1$, $\beta_H = -0.1$ and $\beta_H = 0$, respectively. The stability of the flow can be evaluated by looking at the disturbance amplification

$$N = \ln \sqrt{G} = \ln \sqrt{\frac{E(x_1)}{E(x_0)}}. \tag{2.14}$$

The initial streamwise location, where the disturbance is introduced in the boundary layer, has a significant impact on the algebraic growth. Figure 2.1(*a*) shows the amplification of the optimal disturbances as a function of initial location for $\beta = 0.5$ and $\omega = 0$. Disturbances introduced closer to the leading edge, than the optimal initial location, grow with a slower rate, while disturbances introduced further downstream grow in a larger rate but do not have distance enough to grow as much before the final location. The slower growth rate for disturbances introduced close to the leading edge is due to the influence of the boundary layer thickness. Upstream of the optimal initial location, the boundary layer is not thick enough for the lift-up effect to cause the optimal disturbance. The optimization of the initial location has the advantage of ensuring that the true optimal disturbances are found. Since the adjoint-based optimization technique optimizes the initial disturbance with respect to the disturbance energy in the final location and we are interested in the maximum energy in the whole domain, the true optimum only results when the maximum energy appears in the final location. The optimization of the initial location not only gives the optimal growth, it also ensures that the maximum energy is reached at the final location.

For algebraic growth of optimal disturbances, the optimal initial location moves downstream with increased spanwise wave number and angular frequency of the disturbance. Furthermore, the optimal spanwise wave number increases with decreased pressure gradient, while the optimal angular frequency is equal to zero. For exponential growth of modal disturbances, the optimal angular frequency increases with decreased pressure gradient, while the optimal spanwise wave number is equal to zero, as expected according to the Squire's theorem (Squire 1933).

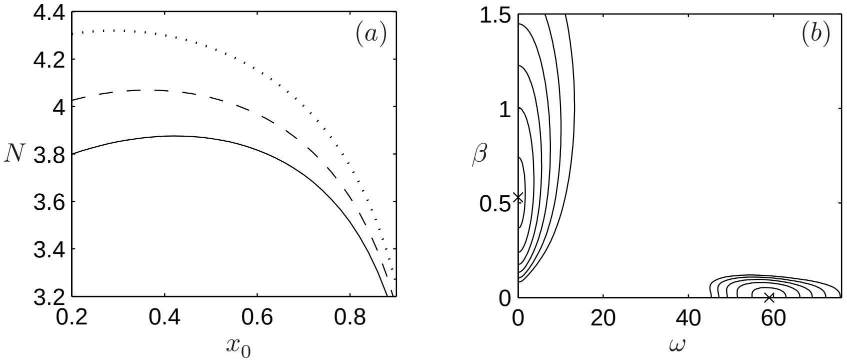

FIGURE 2.1. (*a*) Algebraic amplification as a function of initial location for Falkner–Skan flow with Hartree parameter $\beta_H = 0.1$ (—), $\beta_H = 0$ $(- - -)$ and $\beta_H = -0.1$ $(\cdots)$ for $Re_l = 10^6$ with $\beta = 0.5$ and $\omega = 0$. (*b*) Contours of constant algebraic and exponential amplification for the Blasius boundary layer at $Re_l = 10^6$. The contour spacing is 0.2 and the peak values are indicated with crosses. The optimal disturbances are calculated with the optimal initial locations.

In both the algebraic and exponential growth scenarios, the growth increases with decreased pressure gradient, although the effect is much more pronounced for the exponential growth. Therefore, in a comparison of the two different growth scenarios at $Re_l = 10^6$, the algebraic growth is much larger for the base flow with a favorable pressure gradient and the exponential growth is much larger for the base flow with a adverse pressure gradient, while they are comparable for the Blasius boundary layer. Figure 2.1(*b*) shows the contours of constant algebraic and exponential amplification for the Blasius boundary layer at $Re_l = 10^6$. The optimal disturbances are calculated with the optimal initial locations.

2.4.2. *Transition prediction based on linear theory*

In the transition community, the e^N-method is a well known transition-prediction tool and has been shown to fairly accurately predict transition for simple flows. It was developed independently by Smith & Gamberoni (1956) and van Ingen (1956) and empirically correlates the exponentially growing amplification of linear eigenmodes with the onset of transition. Transition takes place when the amplitude of the most amplified disturbance reaches e^N times its initial amplitude. The e^N-method does not account for the receptivity process. However, Smith & Gamberoni (1956) and van Ingen (1956) reported, after analyzing data from a large number of low-disturbance experiments, that the amplification between 8 and 11 fairly well describs the onset and end of the transition region.

They also concluded that those values decrease with increasing free-stream turbulence. A modification of the e^N-method in order to account for free-stream turbulence was proposed by Mack (1977). The free-stream turbulence level Tu was correlated to the amplification N by comparing the transition Reynolds number Re_T from experimental flat-plate boundary layer data collected by Dryden (1959) with parallel, linear stability theory for the Blasius boundary layer. Mack (1977) suggested the following relation for the amplification at transition

$$N = -8.43 - 2.4 \ln Tu, \tag{2.15}$$

which he claims is valid in the range $0.1\% < Tu < 2\%$. For a free-stream turbulence level less than 0.1%, he mentioned that the dominant disturbance source is thought to be wind-tunnel noise rather than turbulence.

Andersson *et al.* (1999) made an attempt at prediction of bypass-transition due to algebraic growth by correlating the transition Reynolds number and the free-stream turbulence level

$$\sqrt{Re_T}\,Tu = K, \tag{2.16}$$

where K should be constant for free-stream turbulence levels in the range $1\% < Tu < 5\%$. By comparison of different experimental studies, the constant was chosen as $K = 12$.

Other empirical transition-prediction correlations involving the effects of free-stream turbulence and streamwise pressure gradient have been developed. van Driest & Blumer (1963) postulated that transition occurs when the maximum vorticity Reynolds number reaches a critical value, to be correlated with the pressure gradient and free-stream turbulence level. In the case of zero pressure gradient, their formula correlated with experiments agrees well with (2.16). Another example is a model by Abu-Ghannam & Shaw (1980), which gives the Reynolds number based on the momentum thickness θ, at the start and end of the transition region. The only inputs to the model are the free-stream turbulence level and the pressure gradient parameter $\lambda_\theta = (\theta^2/\nu)\partial U_0/\partial x$. More advanced transition prediction and studies of the transition phenomena itself can be made by numerical simulations such as the nonlinear PSE technique (e.g. Hein *et al.* 1999) and DNS.

The transition model of Andersson *et al.* (1999) can be complemented with the addition of base flows with various pressure gradients. The model is based on three assumptions.

1. Assume that the initial disturbance energy is proportional to the free-stream turbulence energy

   $$E(x_0) = Tu^2, \tag{2.17}$$

   for isotropic turbulence with the free-stream turbulence level defined as $Tu = \sqrt{\overline{u'^2}}/U_\infty$. Here u' is the fluctuating streamwise velocity in the free stream and the overbar denotes the temporal mean.

2. Assume that the initial disturbance grows with the optimal rate

$$E(x_1) = GE(x_0) = \overline{G} Re_l E(x_0). \tag{2.18}$$

3. Assume that transition occurs when the final energy reaches a specific value E_T, regardless of the pressure gradient of the base flow

$$E(x_1) = E_T. \tag{2.19}$$

Combining assumptions (2.17–2.19) yields the transition model

$$\sqrt{Re_T} Tu = \frac{k}{\sqrt{\overline{G}}}, \tag{2.20}$$

where k should be constant. Using the same correlation as Andersson *et al.* (1999) and the optimal growth in the Blasius boundary layer gives $k = 0.70$. This model differs from the one of Andersson *et al.* (1999) in the sense that the growth is optimized over the initial location and the disturbances does not evolve from the leading edge.

The influence of free-stream turbulence on the generation of TS-waves is not conclusive. In fact, Boiko *et al.* (1994) made experiments on the behavior of controlled TS-waves, introduced by means of a vibrating ribbon, in a boundary layer subjected to $Tu = 1.5\%$. The measured amplification rates for the waves in the presence of the turbulence generating grid were smaller than for regular TS-waves, and damping set in further upstream than in the absence of the turbulence generating grid. Thus, we make the simple assumption that transition resulting from exponentially growing disturbances occurs at $N = 8$, the dashed line in figure 2.2(a), irrespective of the free-stream turbulence level.

Figure 2.2(b) shows the transition Reynolds number based on the results from the linear stability analysis and the transition model discussed above for free-stream turbulence. The straight part of the lines represents the transition Reynolds number for exponentially growing modal disturbances and the curved part represents bypass-transition. For high free-stream turbulence levels, transition occurs as a result of the breakdown of streaky structures and for low free-stream turbulence levels as a result of exponentially growing disturbances. The cross-over point occurs where the bypass-transition model predicts a higher transition Reynolds number than for the exponentially growing disturbances. According to the model, bypass-transition occurs in the Blasius boundary layer (dashed lines) for a free-stream turbulence level higher than 0.76%. Similar results has been found in experiments. Suder *et al.* (1988) found in their experiment that the bypass mechanism prevailed for free-stream turbulence levels of 0.65% and higher. Kosorygin & Polyakov (1990) suggested that TS-waves and streaks can co-exist and interact for free-stream turbulence levels up to approximately 0.7%. However, the model does not account for the interaction between TS-waves and streaks.

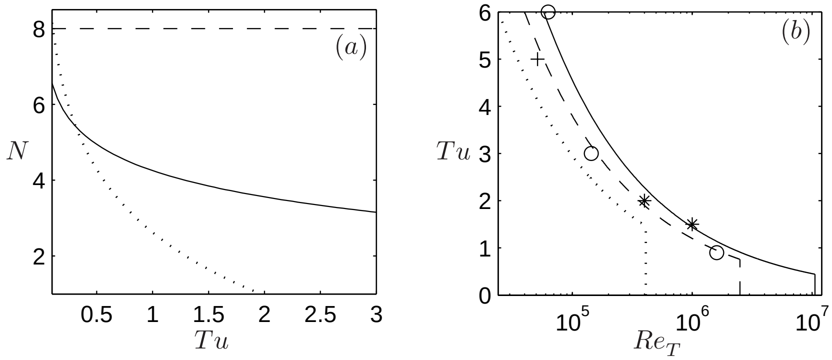

FIGURE 2.2. (a) Predicted amplification at transition as a function of free-stream turbulence level given in percent for algebraic (—) and exponential (− − −) growth. Dotted line: Model by Mack (1977). (b) Lines as in figure 2.1(a). Predicted transition contour in the Re_T-Tu plane. Tu is given in percent. Experimental data for the Blasius boundary layer from Matsubara & Alfredsson (2001) ($*$) and Roach & Brierley (1992) ($\circ$). Numerical data from Yang & Voke (1991) ($+$).

2.5. Application to the Blasius wall jet

In the second paper, the Blasius wall jet is developed and matched to an experimental setup. The stability of the flow to eigenwaves and non-modal streaks is analyzed and compared to the experiments.

2.5.1. *Comparison of linear theory with experiments*

Linear stability analysis is performed with the Blasius wall jet as the base flow. The stability of optimal disturbances and exponential growing waves is examined and compared to measurements performed in the wall-jet facility at Chalmers University of Technology. The base flow is matched to the experiment with the maximum outlet velocity $U_l = 15.4\,\mathrm{m\,s^{-1}}$, corresponding to the Reynolds number $Re_\delta = 173$. Due to growing boundary layers in the experimental nozzle, a virtual slot is placed the distance $l = 29\,\mathrm{mm}$ upstream of the experimental nozzle opening and the virtual slot height is $b^* = 2.06\,\mathrm{mm}$ corresponding to the non-dimensional value $b = 12.3$. A comparison of the base flow with the measured hot-wire data is shown in figure 2.3(a). The agreement increases downstrem of the nozzle opening. The largest disagreement is observed in the upper part of the wall jet and there are two reasons for that. First, a jump of the boundary conditions occur on the top lip of the nozzle as the flow leaves and a kink in the experimental velocity data can be observed. With increased downstream distance, the influence of the nozzle disappears. Secondly, a secondary flow is set up in the experiment, which is not taken into account in the computed base flow.

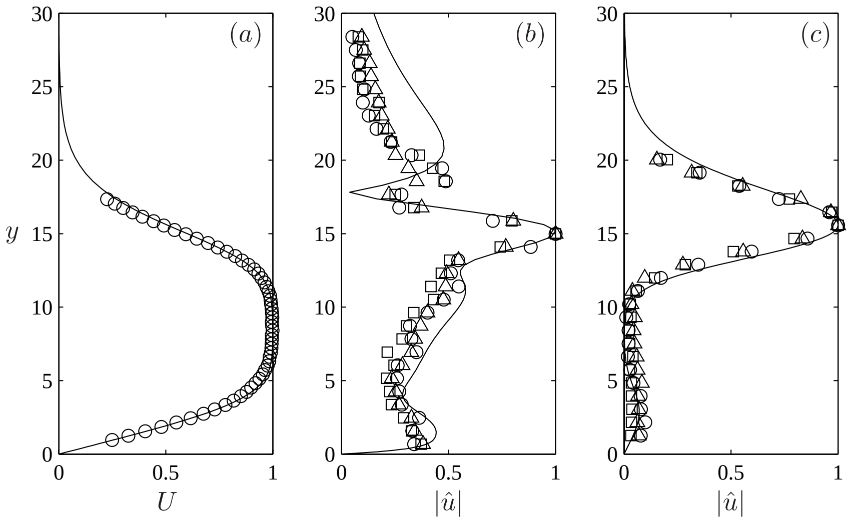

FIGURE 2.3. Comparison of computations (—) and measurements of the Blasius wall jet at $x = 1.55$ for $Re_\delta = 173$. The disturbance amplitudes are normalized with their maximum value. (*a*) Computed and measured (○) base flow. (*b*) Streamwise wave amplitude for $F = 482$. The disturbance are triggered in the experiment by a loudspeaker and have the amplitudes 0.3% (○), 1.1% (□) and 1.7% (△). (*c*) Streamwise streak amplitude. The optimal disturbance are calculated for $\beta = 0.211$, $\omega = 0$, $x_0 = 0.403$ and $x_1 = 1.55$. The experimental results are taken from three spanwise scales corresponding to $\beta = 0.176$ (○), $\beta = 0.218$ (□) and $\beta = 0.264$ (△).

The stability analysis reveals a very high instability of the flow to two-dimensional eigenmodes and a rather high instability to non-modal streaks. The waves are triggered by a loudspeaker in the experiment and the frequency was chosen close to the natural dominating flow frequency, namely 1221 Hz corresponding to $\omega = 14.4$, or $F = 482$, where the reduced frequency is defined by $F = 10^6\omega/Re_l$. Both in the experiment and in the computation, the most amplified frequency decreases with increased streamwise location. Figure 2.3(*b*) shows a comparison of the computed streamwise amplitude distribution and the measurement at the location $x = 1.55$. The measurement was performed with three different forcing amplitudes, 0.3%(○), 1.1% (□) and 1.7% (△), and the agreement in the results between the different forcing amplitudes indicates the linearity of the disturbance. The disturbance has a very typical shape and the peak in the shear layer part is in antiphase to the peak near the wall. The deviation between the linear stability analysis and the experiment in the upper part of the wall jet is most likely due to the difference in the base flow and because the waves in the experiment are not fully developed eigenmodes so close to the nozzle opening, however, the agreement improves downstream.

The computed optimal disturbance consists of streamwise vortices developing into streamwise streaks. Between two vortices, the flow is either moving upward or downward. Where the flow is moving upward between two vortices, high-momentum fluid is moved up from the jet core, producing a high-velocity streak in the shear layer region of the wall jet. In the boundary layer region, a weak low-velocity streak is formed below the high-velocity streak, since the upward motion of fluid there carries low-momentum fluid from the wall region. The opposite motion results, half a wavelength away, where the flow is moving downward between two vortices, producing a low-velocity streak in the shear layer region and a weak high-velocity streak in the boundary layer region. In figure 2.3(*c*), the resulting normalized streak from the optimal disturbance, calculated for $\beta = 0.211$, $\omega = 0$, $x_0 = 0.403$ and $x_1 = 1.55$ is compared with the measured streaks with spanwise scales $\beta = 0.264$ ($\circ$), $\beta = 0.218$ ($\Box$) and $\beta = 0.176$ ($\triangle$). In the experiment, the streaks are introduced in the flow by periodically distributed roughness elements that are located onto the top lip of the nozzle. Both in the computation and in the experiment, the streak remains very similar for different spanwise wave number β. The same is true in the computation for different initial location, x_0.

CHAPTER 3

Large disturbances

3.1. DNS of the Blasius wall jet

In the second paper, the waves and streaks is introduced in the Blasius wall jet and the nonlinear interaction is studied by means of experiments and DNS.

3.1.1. *Numerical method and disturbance generation*

The in-house numerical code at KTH Mechanics (see Lundbladh *et al.* 1999) uses spectral methods to solve the three-dimensional, time-dependent, incompressible Navier–Stokes equations. The discretization in the streamwise and spanwise directions makes use of Fourier series expansions, which enforces periodic solutions. The discretization in the normal direction is represented with Chebyshev polynomial series. A pseudo-spectral treatment of the nonlinear terms is used. The time advancement used is a second-order Crank–Nicolson method for the linear terms and a four-step low-storage third-order Runge–Kutta method for the nonlinear terms. The Blasius wall jet is spatially growing and to fulfill the necessary periodic boundary condition in the streamwise direction, required by the spectral discretization, a fringe region (see Nordström *et al.* 1999) is added in the downstream end of the computational domain. In this region, the flow is smoothly forced to the desired inflow solution. The waves and streaks computed by the linear theory (see figure 2.3) are also added to the desired solution in the end of the fringe region. The forcing of the disturbances is turned on smoothly in both space and time. The amplitudes of the waves and streaks are prescribed at the end of the fringe region to 0.001 and 0.03, respectively.

3.1.2. *Spectral analysis and flow structures*

The primary instability in inflectional base flows such as free shear layers and wall jets is a strong inviscid exponential instability resulting in the roll-up of waves into strong spanwise vortices. These two-dimensional vortices can experience two different types of secondary instability. For low initial three-dimensional excitation, the secondary instability is subharmonic and associated with vortex pairing, like that observed by Bajura & Catalano (1975). If the initial three-dimensional excitation is large enough, a three-dimensional secondary instability is predominant, which suppresses the vortex pairing. In this study, the interaction of waves and streaks is studied and the initial amplitude

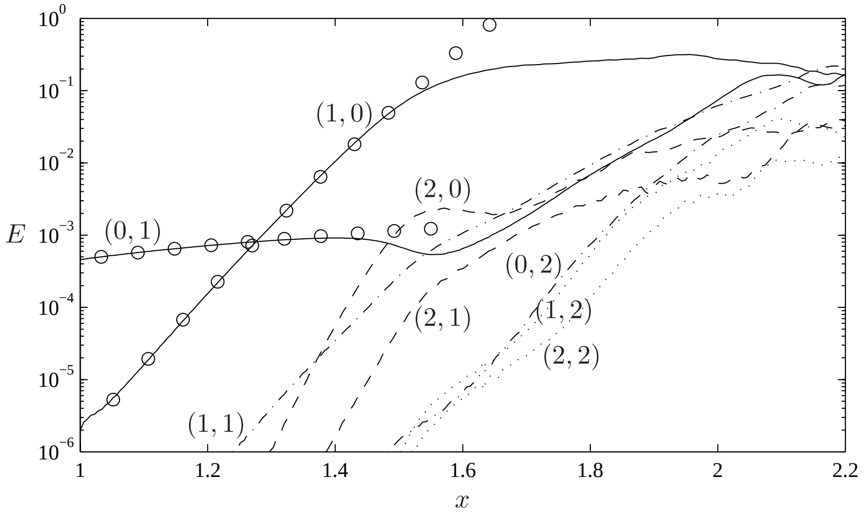

FIGURE 3.1. Energy in different Fourier modes (ω, β) from the DNS. The initially excited modes (waves and streaks) are shown by solid lines, the nonlinearly generated modes are shown by dashed and dotted lines. The modes are indicated in the figure. Results from the PSE ($\circ$) are shown for comparison.

of the streaks is rather large. A convenient way to study the behavior is to look at the energy development of the Fourier components shown in figure 3.1. The velocity components are Fourier transformed in time and in the spanwise direction and the notation (ω, β), where ω and β are the frequency and spanwise wavenumber, each normalized with the corresponding fundamental frequency and wavenumber, is used. Thus, the waves and the streaks are represented by $(1,0)$ and $(0,1)$, respectively, the solid lines in figure 3.1. Before nonlinear interaction sets in, the instability modes amplify in agreement with the linear theory as observed in the beginning of the computational box, where the results from the PSE ($\circ$) are shown for comparison. The waves grow according to the linear theory for surprisingly large amplitudes while the nonlinear interaction for the streaks is encountered earlier. At about $x = 1.3$ to $x = 1.4$, nonlinear effects start to be apparent when energy is transferred to the modes $(1,1)$, $(2,0)$ and $(2,1)$. Further downstream, the streak mode $(1,0)$ is decaying and a dip in the energy can be observed at approximately $x = 1.55$. At that location, the time-periodic mode $(1,0)$ starts to saturate and an abrupt change of the breakdown process happens, namely, an exponential growth of the streak mode. The exponentially growing two-dimensional waves break down due to what appears to be a three-dimensional secondary instability triggered by the presence of the streaks.

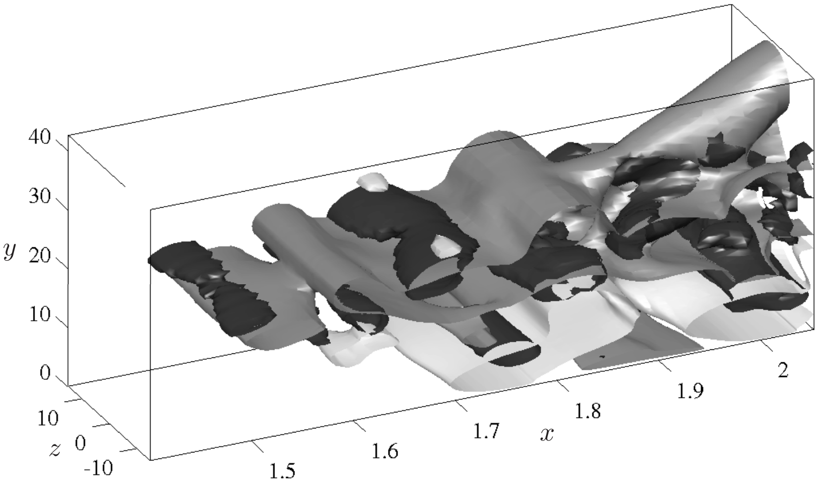

FIGURE 3.2. Isosurfaces of positive streamwise disturbance velocity (medium grey), negative disturbance velocity (light grey) and λ_2 (dark grey). The waves and streaks are forced with initial amplitudes 0.1% and 3%, respectively, in the Blasius wall jet at $Re_\delta = 173$. The levels of the isosurfaces are 0.15, -0.15 and -0.005, respectively.

The simulated flow is visualized in figure 3.2, where positive and negative isosurfaces of the instantaneous streamwise disturbance velocity are represented in medium grey and light grey, respectively. Vortical structures can be identified in the flow by plotting regions where the second largest eigenvalue λ_2 of the Hessian of the pressure assumes negative values (Jeong *et al.* 1997). The vortical structures in figure 3.2 are represented by dark grey isosurfaces. Very typical mushroom-shaped structures appear, at around $x = 2$, when the high-velocity streaks become dominant and are lifted up from the shear layer region. In a comparison to the experimental smoke visualization presented in paper 2, a staggered formation of mushroom-shaped streaks can be observed both in the experiment and in the simulation. Such structures were also observed by e.g. Wernz & Fasel (1996, 1997) and Gogineni & Shih (1997). Just downstream of those pronounced structures, the flow breaks down to turbulence.

CHAPTER 4

Conclusions and outlook

The stability of wall-bounded flows has been investigated by means of linear parabolized stability equations valid both for exponential growing waves and algebraically growing streaks. An adjoint-based optimization technique was used to optimize the growth of non-modal streaks. The growth of modal waves was maximized in the sense that the envelope of the most amplified eigenmode was calculated. Two wall-bounded flows has been investigated, the Falkner–Skan boundary layer subjected to favorable, adverse and zero pressure gradients and the Blasius wall jet.

In the first paper, the Falkner–Skan boundary layer is considered. The optimization of the algebraic growth is carried out over the initial streamwise location as well as the spanwise wave number and the angular frequency. It is found that the initial streamwise location, where the disturbance is introduced in the boundary layer, has a significant impact on the growth and moves downstream with decreased pressure gradient of the base flow. In both the algebraic and exponential growth scenarios, the growth is found to increase with decreased pressure gradient, although the effect is much more pronounced for the exponential growth. Furthermore, a unified transition-prediction method incorporating the influence of free-stream turbulence is suggested.

In the second paper, the Blasius wall jet is matched to the measured flow in an experimental wall-jet facility. Linear stability analysis with respect to the growth of two-dimensional waves and streamwise streaks is performed and compared to the experiments. The flow reveals a very high instability to two-dimensional waves and a rather high instability to non-modal streaks. The theory agrees well with the measurements. Furthermore, the nonlinear interaction of introduced waves and streaks and the flow structures preceding the flow breakdown are investigated by means of direct numerical simulations. It is demonstrated that the streaks play an important role in the breakdown process, where their growth is transformed from algebraic to exponential as they become part of the secondary instability of the two-dimensional waves.

The next step is to perform a more detailed investigation of the Blasius wall jet and deepen the fundamental understanding of the transition process. Control strategies will be applied to both postpone transition and enhance mixing.

Acknowledgment

First of all, I want to thank my supervisor, Professor Dan Henningson, for giving me the opportunity to work as his student and to develop my knowledge within the subject fluid dynamics. He is always very helpful and brings joy into good as well as bad days at the office. In particular, I value his professional way to work and his personal way to be a friend.

I want to thank Doctor Jan Pralits, my previous colleague and office mate, for all the time he spent to help me to get started with the project. He was always very helpful and encouraging when ever I needed help.

I also want to thank Mattias Chevalier for the help with various modifications of the spectral code and Doctor Luca Brandt for the guidance with the direct numerical simulations.

Many thanks to the people at KTH Mechanics for providing a very nice atmosphere at the department. In particular I want to thank Arnim Brüger, Astrid Herbst, Erik Stålberg, Jan Pralits, Jens Fransson, Jérôme Hœpffner, Martin Skote, Mattias Chevalier and Olle Törnblom. I also want to thank the department for providing the gym card and the opportunity to play indoor bandy.

This work has been funded by the Swedish Energy Agency (Energimyndigheten).

Finally, I want to thank my mother Doris and my father Robert for all the support that made this possible, my niece Jolin for her delight, my grandmother Gertrud, my grandfather Harry and all my friends.

Bibliography

Abu-Ghannam, B. & Shaw, R. 1980 Natural transition of boundary layers - the effects of turbulence, pressure gradient, and flow history. *J. Mech. Eng. Sci.* **22** (5), 213–228.

Andersson, P., Berggren, M. & Henningson, D. 1999 Optimal disturbances and bypass transition in boundary layers. *Phys. Fluids* **11** (1), 134–150.

Bajura, R. A. & Catalano, M. R. 1975 Transition in a two-dimensional plane wall jet. *J. Fluid Mech.* **70** (4), 773–799.

Bajura, R. A. & Szewczyk, A. A. 1970 Experimental investigation of a laminar two-dimensional plane wall jet. *Phys. Fluids A* **13** (7), 1653–1664.

Bertolotti, F. P., Herbert, T. & Spalart, P. R. 1992 Linear and nonlinear stability of the Blasius boundary layer. *J. Fluid Mech.* **242**, 441–474.

Boiko, A., Westin, K., Klingmann, B., Kozlov, V. & Alfredsson, P. 1994 Experiments in a boundary layer subjected to free stream turbulence. Part 2. The role of TS-waves in the transition process. *J. Fluid Mech.* **281**, 219–245.

Chun, D. H. & Schwarz, W. H. 1967 Stability of the plane incompressible viscous wall jet subjected to small disturbances. *Phys. Fluids A* **10** (5), 911–915.

van Driest, E. & Blumer, C. 1963 Boundary layer transition: Freestream turbulence and pressure gradient effects. *AIAA J.* **1**, 1303–1306.

Dryden, H. 1959 Transition from laminar to turbulent flow. In *Turbulent flows and heat transfer* (ed. C. Lin), pp. 1–74. N.J.: Princeton Univ. Press.

Ellingsen, T. & Palm, E. 1975 Stability of linear flow. *Phys. Fluids* **18** (4), 487–488.

Fjørtoft, R. 1950 Application of integral theorems in deriving criteria for instability for laminar flows and for the baroclinic circular vortex. *Geofys. Publ., Oslo* **17** (6), 1–52.

Floryan, J. & Saric, W. 1979 Stability of Görtler vortices in boundary layers. *AIAA J.* **20** (3), 316–324.

Gogineni, S. & Shih, C. 1997 Experimental investigation of the unsteady structure of a transitional plane wall jet. *Experiments in Fluids* **23**, 121–129.

Hall, P. 1983 The linear development of Görtler vortices in growing boundary layers. *J. Fluid Mech.* **130**, 41–58.

Hanifi, A. 1995 Local and non-local stability analysis and transition prediction of compressible boundary layer flows. PhD thesis, Royal Institute of Technology, Stockholm, Sweden.

Hein, S., Stolte, A. & Dallmann, U. 1999 Identification and analysis of nonlinear transition scenarios using NOLOT/PSE. *Z. Angew. Math. Mech.* **79**, S109–S112.

Henningson, D. 1996 Comment on "Transition in shear flows. Nonlinear normality versus non-normal linearity" [Phys. Fluids 7, 3060 (1995)]. *Phys. Fluids* **8** (8), 2257–2258.

van Ingen, J. 1956 Suggested semi-emperical method for the calculation of the boundary layer transition region. *Tech. Rep.* UTH-74. Dep. of Aero. Eng., University of Technology, Delft.

Jeong, J., Hussain, F., Schoppa, W. & Kim, J. 1997 Coherent structures near the wall in a turbulent channel flow. *J. Fluid Mech.* **332**, 185–214.

Klebanoff, P. 1971 Effect of freestream turbulence on the laminar boundary layer. *Bull. Am. Phys. Soc.* **10**, 1323.

Kosorygin, V. & Polyakov, N. 1990 Laminar boundary layers in turbulent flows. In *Laminar-Turbulent Transition* (eds. D. Arnal & R. Michel), pp. 573–578. Springer-Verlag.

Landahl, M. 1980 A note on an algebraic instability of inviscid parallel shear flows. *J. Fluid Mech.* **98** (2), 243–251.

Lundbladh, A., Berlin, S., Skote, M., Hildings, C., Choi, J., Kim, J. & Henningson, D. S. 1999 An efficient spectral method for simulation of incompressible flow over a flat plate. *Tech. Rep.*. KTH, Department of Mechanics, Stockholm.

Mack, L. 1977 Transition prediction and linear stability theory. In *AGARD-CP-224*, pp. 1–1 to 1–22. NATO, Paris.

Matsubara, M. & Alfredsson, P. 2001 Disturbance growth in boundary layers subjected to free-stream turbulence. *J. Fluid Mech.* **430**, 149–168.

Mele, P., Morganti, M., Scibilia, M. & Lasek, A. 1986 Behavior of wall jet in laminar-to-turbulent transition. *AIAA Journal* **24** (6), 938–939.

Nordström, J., Nordin, N. & Henningson, D. S. 1999 The fringe region technique and the fourier method used in the direct numerical simulation of spatially evolving viscous flows. *SIAM J. Sci. Comput.* **20** (4), 1365–1393.

Orr, W. M. F. 1907 The stability or instability of the steady motions of a perfect liquid and of a viscous liquid. Part I: A perfect liquid. Part II: A viscous liquid. *Proc. R. Irish Acad. A* **27**, 9–138.

Reyleigh, L. 1980 On the stability of certain fluid motions. *Proc. Math. Soc. Lond.* **11**, 57–70.

Reynolds, O. 1883 An experimental investigation of the circumstances which determine whether the motion of water shall be direct or sinuous, and of the law of resistance in parallel channels. *Phil. Trans. Royal Soc.* **174**, 935–982.

Roach, P. & Brierley, D. 1992 The influence of a turbulent free-stream on zero pressure gradient transitional boundary layer development. I. Test cases T3A and T3B. In *Numerical Simulation of Unsteady Flows and Transiton to Turbulence* (eds. O. Pironneau, W. Rodi, I. Ryhming, A. Savill & T. Truong), pp. 303–316. Cambridge University Press.

Schlichting, H. 1933 Berechnung der anfachung kleiner störungen bei der plattenströmung. *ZAMM* **13**, 171–174.

Schubauer, G. B. & Skramstad, H. F. 1947 Laminar boundary layer oscillations and stability of laminar flow. *J. Aero. Sci.* **14**, 69–78.

Smith, A. & Gamberoni, N. 1956 Transition, pressure gradient and stability theory. *Tech. Rep.* ES 26388. Douglas Aircraft Co., EL Segundo, Calif.

Sommerfeld, A. 1908 Ein beitrag zur hydrodynamischen erklärung der turbulenten flüssigkeitbewegungen. In *Atti del 4 Congr. Internat. dei Mat. III*, pp. 116–124. Roma.

Squire, H. B. 1933 On the stability for three-dimensional disturbances of viscous fluid flow between parallel walls. *Proc. Roy. Soc. Lond. Ser. A* **142**, 621–628.

Suder, K., O'Brien, J. & Reshotko, E. 1988 Experimental study of bypass transition in a boundary layer. *NASA TM* **100913**.

Tollmien, W. 1929 Über die entstehung der turbulenz. Nachr. Ges. Wiss Göttingen, 21–44, (English translation NACA TM 609, 1931).

Tumin, A. & Aizatulin, L. 1997 Instability and receptivity of laminar wall jets. *Theoret. Comput. Fluid Dynamics* **9**, 33–45.

Wernz, S. & Fasel, H. F. 1996 Numerical investigation of unsteady phenomena in wall jets. *AIAA Paper* 96-0079.

Wernz, S. & Fasel, H. F. 1997 Numerical investigation of forced transitional wall jets. *AIAA Paper* 97-2022.

Westin, K., Boiko, A., Klingmann, B., Kozlov, V. & Alfredsson, P. 1994 Experiments in a boundary layer subjected to free stream turbulence. Part 1. Boundary layer structure and receptivity. *J. Fluid Mech.* **281**, 193–218.

Yang, Z. Y. & Voke, P. R. 1991 Numerical simulation of transition under turbulence. *Tech. Rep.* ME-FD/91.01. Dept. Mech. Eng. University of Surrey.

Part 2

Papers

Paper 1

Exponential vs Algebraic Growth and Transition Prediction in Boundary Layer Flow

By Ori Levin[1]**, and Dan S. Henningson**[1,2]

[1]Department of Mechanics, Royal Institute of Technology (KTH), SE-100 44 Stockholm, Sweden
[2]The Swedish Defence Research Agency (FOI), Aeronautics Division (FFA), SE-172 90 Stockholm, Sweden

For applications regarding transition prediction, wing design and control of boundary layers, the fundamental understanding of disturbance growth in the flat-plate boundary layer is an important issue. In the present work we investigate the energy growth of eigenmodes and non-modal optimal disturbances. We present a set of linear governing equations for the parabolic evolution of wavelike disturbances valid both for the exponential and algebraic growth scenario. The base flow is taken as the Falkner–Skan similarity solution with favorable, adverse and zero pressure gradients. The optimization is carried out over the initial streamwise position as well as the spanwise wave number and frequency. The exponential growth is maximized in the sense that the envelope of the most amplified eigenmode is calculated. In the case of algebraic growth, an adjoint-based optimization technique is used. We find that the optimal algebraic disturbance introduced at a certain downstream position gives rise to a larger growth than for the optimal disturbance introduced at the leading edge. The exponential and algebraic growth is compared and a unified transition-prediction method based on available experimental data is suggested.

1. Introduction

Fundamental understanding is important as a basis for engineering applications. In the aviation industry one wishes to decrease wing drag and lower operation costs for aircraft. One critical parameter is the streamwise transition position on the wing from laminar to turbulent flow. The fundamental understanding of the instabilities in the flat-plate boundary layer serve as a basis for the generation of tools for transition prediction, wing design and control of boundary layers.

The prediction of the stability of a given flow and the amplification of small disturbances have been of interest to the fluid dynamics community for more than a century. The traditional stability-analysis technique is to solve the eigenvalue problem of the Orr–Sommerfeld and Squire equations, which are the linearized stability equations based on the assumption of parallel flow with wavelike disturbances. The unstable eigenmodes are historically referred to as Tollmien–Schlichting (TS) waves, usually taking the form of exponentially growing 2D waves.

The idea of solving the parabolic evolution of disturbances in non-parallel boundary layers was first introduced by Floryan & Saric (1979) and later also by Hall (1983) for steady Görtler vortices. Bertolotti *et al.* (1992) developed the method of parabolic evolution of eigenmodes in boundary layers and derived the parabolized stability equations (PSE). The method is computationally very fast and has been shown to be in excellent agreement with direct numerical simulations (DNS) of the Navier–Stokes equations and experiments.

In the transition community, the e^N-method is a well known transition-prediction tool and has been shown to fairly accurately predict transition for simple flows. It was developed independently by Smith & Gamberoni (1956) and van Ingen (1956) and empirically correlates the exponentially growing amplification of linear eigenmodes with the onset of transition. Transition takes place when the amplitude of the most amplified disturbance reaches e^N times its initial amplitude. The method does not account for the receptivity process. However, they reported, after analyzing data from a large number of low-disturbance experiments, that the N-factors between 8 and 11 fairly well described the onset and end of the transition region. They also concluded that those values decreased with increasing freestream turbulence. A modification of the e^N-method in order to account for freestream turbulence was proposed by Mack (1977). The freestream-turbulence level Tu was correlated to the N-factor by comparing the transition Reynolds number from experimental flat-plate boundary layer data collected by Dryden (1959) with parallel, linear stability theory for the Blasius boundary layer. Mack suggested the following relation for the N-factor at transition

$$N = -8.43 - 2.4 \ln Tu, \tag{1}$$

which he claims is valid in the range $0.1\% < Tu < 2\%$. For a freestream-turbulence level less than 0.1%, he mentioned that the dominant disturbance source is thought to be wind-tunnel noise rather than turbulence.

Exponential instability involving unstable eigenmodes is not the only transition scenario. For a sufficiently large disturbance amplitude, algebraic non-modal growth can lead to so-called bypass transition, not associated with exponential instabilities. At a moderate or high lever of freestream turbulence, many experiments have observed streaky structures, taking the form of elongated streamwise structures with narrow spanwise scales and much larger streamwise scales. This type of disturbance is historically denoted as the Klebanoff mode after the boundary-layer experiments of Klebanoff (1971). More recent experiments displaying streaky structures in boundary layers, subject to various levels of freestream turbulence, have been performed by e.g. Westin *et al.* (1994) and Matsubara & Alfredsson (2001). Ellingsen & Palm (1975) performed linear stability analysis of inviscid channel flow. They showed that finite three-dimensional disturbances without streamwise variation can lead to instability, even though the basic velocity does not possess any inflection point. The instability leads to an increase linearly with time of the streamwise disturbances, producing alternating low and high velocity streaks. Landahl (1980) demonstrated that all parallel inviscid shear flows can be unstable to three-dimensional disturbances, which lead to a growth of the disturbance energy at least as fast as linearly in time. The physical interpretation of the formation of the streaks is the lift-up effect, i.e. that fluid elements initially retain their horizontal momentum when displaced in the wall-normal direction, hence causing a streamwise disturbance. The combination of inviscid, algebraic growth and viscous dissipation has been known as transient growth (see Hultgren & Gustavsson 1981; Butler & Farrell 1992; Henningson *et al.* 1993; Reddy & Henningson 1993). In those papers, the optimal transient growth and associated disturbances were computed, in various parallel flows, by optimizing over the eigenmodes of the Orr–Sommerfeld operator.

Luchini (1996) considered steady spanwise periodic disturbances, with a spanwise scale much larger than the boundary layer thickness and much smaller than the streamwise scale. An eigenvalue problem in the Sturm–Liouville form was formulated for the Blasius boundary layer and it was concluded that there is a mode that possesses unbounded growth of the streamwise velocity. Tumin (2001) made an extension of Luchini's theory to the Falkner–Skan boundary layer and found that the unbounded growth may be suppressed by a favorable pressure gradient.

Andersson *et al.* (1999) and Luchini (2000) adopted an input-output methodology to calculate the optimal disturbance in the Blasius boundary layer, taking the non-parallel effects into account. The governing equations used are parabolic in the streamwise direction and were obtained from the linearized Navier–Stokes equations subject to the boundary-layer scalings. The disturbances were assumed to be slowly varying in the streamwise direction and periodic in the spanwise direction and time. An adjoint-based optimization technique was used to optimize the input disturbance at the leading edge giving rise to the largest disturbance energy gain at the final downstream position. By going to the limit of large Reynolds number (based on the final streamwise position), Luchini (2000) motivated the assumption that the optimal initial disturbance has a zero streamwise component, while the final downstream disturbance only consist of the streamwise component. That assumption simplifies the optimization procedure considerably. Andersson *et al.* (1999) and Luchini (2000) independently calculated the spanwise wave number $\beta = 0.45$ and a zero frequency for the optimal disturbance in the large-Reynolds-number limit giving rise to a growth $G = 0.0022 Re_l$. Their results agreed remarkably well with experimental data produced by Westin *et al.* (1994), irrespective of the absent optimization procedure in the experiments. Tumin & Reshotko (2003) made an extension of the model by Luchini (2000) to the case of compressible boundary layers. They also investigated the effect of different initial positions of the optimal disturbance.

Corbett & Bottaro (2000) used an direct-adjoint technique similar to the one used by Andersson *et al.* (1999) and Luchini (2000) to calculate optimal disturbances to the temporal problem for the Falkner–Skan boundary layer. The main advantage of the parallel-flow assumption, in contrast to the spatial approach, is that it permits the study of oblique disturbances with comparable streamwise and spanwise scales. It was found that optimal disturbances in flows subject to adverse pressure gradients experience greater amplifications and those in accelerated flows less amplification in comparison to the Blasius boundary layer. It was also found, as in the case for the Blasius boundary layer, that the most amplified disturbances are streamwise elongated structures.

Andersson *et al.* (1999) made an attempt at prediction of bypass-transition due to algebraic growth by correlating the transition Reynolds number Re_T and the freestream-turbulence level

$$\sqrt{Re_T}Tu = K, \tag{2}$$

where K should be constant for freestream-turbulence levels in the range $1\% < Tu < 5\%$. By comparison of different experimental studies the constant was chosen as $K = 12$.

Other empirical transition-prediction correlations involving the effects of freestream turbulence and streamwise pressure gradient have been developed. van Driest & Blumer (1963) postulated that transition occurs when the maximum vorticity Reynolds number reaches a critical value, to be correlated with the pressure gradient and freestream-turbulence level. In the case of zero pressure gradient their formula correlated with experiments agrees well with (2). Another example is a model by Abu-Ghannam & Shaw (1980), which gives the Reynolds number based on the momentum thickness θ, at the start and end of the transition region. The only inputs to the model are the freestream-turbulence level and the pressure gradient parameter $\lambda_\theta = (\theta^2/\nu)\partial U_0/\partial x$. More advanced transition prediction and studies of the transition phenomena itself can be made by numerical simulations such as the non-linear PSE technique (e.g. Hein *et al.* 1999).

In the present paper we first introduce governing equations valid for both linear exponential instability and algebraic instability analysis. We follow the work done by Andersson *et al.* (1999) in the algebraic-instability regime and calculate optimal disturbances in the large-Reynolds-number limit for flat-plate boundary layers with favorable, adverse and zero pressure gradients. The optimization is carried out over the initial streamwise position as well as the spanwise wave number and frequency. We present an energy growth for the optimal disturbance introduced at a certain downstream position, more than 50% larger than for the optimal disturbance introduced at the leading edge.

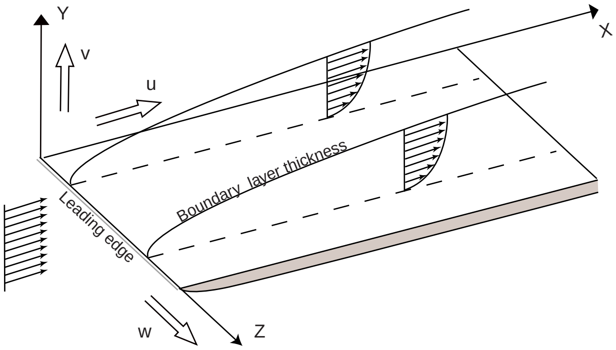

FIGURE 1. Flat-plate boundary layer flow.

Furthermore, we calculate the exponential growth of the most amplified eigenmodes for the same base flows and Reynolds number. We conclude with comparing the two different instability scenarios and assess their impact on the transition Reynolds number by using a generalized version of (2) and the assumption that exponentially growing disturbances have a weak receptivity to freestream turbulence.

2. General Formulation

2.1. *Governing equations*

In this part we will discuss a set of equations that is valid for both algebraically and exponentially growing disturbances, even though the problems are associated with different scales. The well-known PSE technique (Bertolotti *et al.* 1992; Herbert 1997) uses the so called PSE-scaling (see Table 1), which is suitable for exponentially growing eigenmodes. Here we follow the work by Andersson *et al.* (1999) and use a scaling appropriate for algebraically growing non-modal disturbances.

Consider an incompressible boundary layer over a flat plate as illustrated in Figure 1. The scalings originate from the boundary-layer approximations and are also summarized in Table 1. The streamwise coordinate x is scaled with the length scale l, which is a fixed distance from the leading edge. The wall-normal and spanwise coordinates y and z, respectively, are scaled with the boundary-layer parameter $\delta = \sqrt{\nu l / U_\infty}$, where ν is the kinematic viscosity of the fluid and U_∞ is the streamwise freestream velocity at the distance l from the leading edge. The streamwise velocity u is scaled with U_∞, while the wall-normal and spanwise velocities v and w, respectively, are scaled with $U_\infty \delta / l$. The pressure p is scaled with $\rho U_\infty^2 \delta^2 / l^2$ and the time t is scaled with l / U_∞. The Reynolds numbers used here are defined as $Re_l = U_\infty l / \nu$ and $Re_\delta = U_\infty \delta / \nu$. It is useful to note the relations $l/\delta = Re_\delta = \sqrt{Re_l}$.

We want to study the linear stability of a high Reynolds number flow. The non-dimensional Navier–Stokes equations for an incompressible flow are

Var.	x	y, z	t	$\hat{u}$	$\hat{v}, \hat{w}$	$\hat{p}$	α	β	ω
BL	l	δ	l/U_∞	U_∞	$U_\infty \delta/l$	$\rho U_\infty^2 \delta^2/l^2$		$1/\delta$	U_∞/l
PSE	δ	δ	δ/U_∞	U_∞	U_∞	ρU_∞^2	$1/\delta$	$1/\delta$	U_∞/δ
Ratio	Re_δ	1	Re_δ	1	$1/Re_\delta$	$1/Re_\delta^2$		1	$1/Re_\delta$

Table 1. The boundary-layer and PSE-scalings of the variables and their ratio.

linearized around a two-dimensional, steady base flow $\big(U(x,y), V(x,y), 0\big)$ to obtain the stability equations for the spatial evolution of three-dimensional, time-dependent disturbances $\big(u(x,y,z,t), v(x,y,z,t), w(x,y,z,t), p(x,y,z,t)\big)$. The base flow and the disturbances are scaled in the same way. The disturbances are taken to be periodic in the spanwise direction and time, which allows us to assume solutions of the form

$$f = \hat{f}(x,y) e^{\displaystyle iRe_\delta \int_{x_0}^{x} \alpha(x)\, dx + i\beta z - i\omega t}, \tag{3}$$

where f represents either one of the disturbances u, v, w or p. The complex streamwise wave number α captures the fast wavelike variation of the modes and is therefore scaled with $1/\delta$. α itself is assumed to vary slowly with x. Since x is scaled with l, the factor Re_δ appears in front of the integral. The x-dependence in the amplitude function $\hat{f}$ includes the weak variation of the disturbances. The real spanwise wave number β and angular frequency ω are scaled in a consistent way with z and t, respectively. Introducing the assumption (3) in the linearized Navier–Stokes equations and neglecting all third order terms in $1/Re_\delta$ or higher, we arrive at the parabolized stability equations in boundary-layer scalings

$$\hat{u}_x + iRe_\delta \alpha \hat{u} + \hat{v}_y + i\beta \hat{w} = 0, \tag{4}$$

$$(U_x + iRe_\delta \alpha U - i\omega)\hat{u} + U\hat{u}_x + V\hat{u}_y + U_y \hat{v} + \frac{\hat{p}_x}{Re_\delta^2} + \frac{i\alpha \hat{p}}{Re_\delta} = \hat{u}_{yy} - k^2 \hat{u}, \tag{5}$$

$$(V_y + iRe_\delta \alpha U - i\omega)\hat{v} + U\hat{v}_x + V_x \hat{u} + V\hat{v}_y + \hat{p}_y = \hat{v}_{yy} - k^2 \hat{v}, \tag{6}$$

$$(iRe_\delta \alpha U - i\omega)\hat{w} + U\hat{w}_x + V\hat{w}_y + i\beta \hat{p} = \hat{w}_{yy} - k^2 \hat{w}, \tag{7}$$

where $k^2 = \alpha^2 + \beta^2$. Since we are considering both algebraically and exponentially growing disturbances, where the appropriate scales differ, the determination of which terms are of higher order needs a discussion. The boundary-layer and PSE-scalings of the variables and their ratio are presented in Table 1. The last line in Table 1 can also be interpreted as the relative difference in order between the algebraic and exponential disturbances.

Consider the algebraic instability problem. The order of magnitude of all amplitude functions, the spanwise wave number and angular frequency are the same. For algebraically growing disturbances, only weak streamwise variations

Instability	$\mathcal{O}(1)$	$\mathcal{O}(Re_\delta)$	$\mathcal{O}(Re_\delta^2)$
algebraic	$\hat{u}, \hat{v}, \hat{w}, \hat{p}, \beta, \omega$		
exponential	$\hat{u}, \alpha, \beta$	$\hat{v}, \hat{w}, \omega$	$\hat{p}$

TABLE 2. Orders of the variables relative to the boundary-layer scalings.

are considered, captured by the amplitude functions themselves, so the streamwise wave number α is set to zero. After disregarding terms including α there is only one term of higher order kept in (4–7). That term is the $\hat{p}_x/Re_\delta^2$ term in the streamwise momentum equation (5). It is needed for the exponential instability problem, but is obviously $\mathcal{O}(1/Re_\delta^2)$ for the algebraic instability problem. Note that all the other terms are $\mathcal{O}(1)$ and there are no $\mathcal{O}(1/Re_\delta)$ terms left in the equations.

For the exponential instability problem we need to reconsider the orders of magnitude of the terms in (4–7). Note that we will be comparing the relative order between the terms within each equation and consider the two lowest orders as important for the problem. Now we include a fast oscillatory streamwise variation in the disturbances, implying that α is $\mathcal{O}(1)$ and ω is $\mathcal{O}(Re_\delta)$, since $\omega = \alpha c$ (c is the complex phase speed). A balance of terms in the continuity equation implies that $\hat{v}$ and $\hat{w}$ is $\mathcal{O}(Re_\delta)$. The total time derivative should balance the pressure gradient in the normal momentum equation (6) and $\hat{p}$ changes to $\mathcal{O}(Re_\delta^2)$. The second, third, sixth and eighth term in the streamwise momentum equation (5) are $\mathcal{O}(Re_\delta)$, the other terms are $\mathcal{O}(1)$. In the normal momentum equation (6), the second, third and seventh term are $\mathcal{O}(Re_\delta^2)$, the other terms are $\mathcal{O}(Re_\delta)$ except the $V_x\hat{u}$ term, which is only $\mathcal{O}(1)$. Hence, that term is negligible for the exponential instability problem. In the spanwise momentum equation (7) the first, second and fifth term are $\mathcal{O}(Re_\delta^2)$, while the rest of the terms are $\mathcal{O}(Re_\delta)$.

As a summary, the different orders of magnitude of the amplitude functions, wave numbers and angular frequency based on the scaling used are presented in Table 2. We can conclude that all the terms in (4–7) are generally of the first or the second order except the $\hat{p}_x/Re_\delta^2$ term, in the streamwise momentum equation (5), which is of the third order for the algebraic instability problem and the $V_x\hat{u}$ term, in the normal momentum equation (6), which is of the third order for the exponential instability problem. Both of those terms, however, have to be included in a general formulation of the problem. Unfortunately, the $\hat{p}_x/Re_\delta^2$ term introduces numerical instability, setting a lower limit on the streamwise step size.

We are interested in solutions to (4–7) subject to no-slip conditions at the plate and vanishing at the wall-normal position $y_{\max}$ well outside the boundary layer. The boundary conditions in the wall-normal direction can then be written

$$\begin{aligned} \hat{u} = \hat{v} = \hat{w} = 0 \quad \text{at} \quad y = 0, \\ \hat{u} = \hat{v} = \hat{w} = 0 \quad \text{at} \quad y = y_{\max}. \end{aligned} \tag{8}$$

The set of equations (4–7) is nearly parabolic in the streamwise coordinate and are marched forward from an initial position x_0 to a final position x_1. Given the initial conditions

$$\hat{u} = \hat{u}_0(y), \quad \hat{v} = \hat{v}_0(y), \quad \hat{w} = \hat{w}_0(y) \quad \text{at} \quad x = x_0, \tag{9}$$

the wave number β and the angular frequency ω, the initial-boundary-value problem (4–9), can be solved from x_0 to x_1 to obtain the downstream development of the disturbance. In addition, an additional equation for the streamwise wave number α is needed in the exponential instability problem, see Section 4.1

2.2. *Mathematical characteristics*

The large computational gain of the PSE technique is a result of the assumption that the disturbance can be decomposed into a rapidly varying wavelike component and a slowly varying amplitude function. The equations governing the evolution of the amplitude functions are parabolized and can be solved economically using a marching procedure. However, although there are no second streamwise derivatives left in the stability equations (4–7), still some ellipticity remains causing numerical stability problems. This is demonstrated by a rapid oscillation of the solution when the streamwise marching step becomes too small. The sources of ellipticity arise from the upstream propagation of acoustic waves and viscous diffusion. Haj-Hariri (1994) suggested the suppression of the upstream propagation of acoustic waves by either removing the streamwise derivative of the pressure or the streamwise velocity amplitude function in the streamwise momentum or continuity equation after analysis of disturbances with a fixed angular frequency in a parallel boundary layer. Li & Malik (1994, 1996) showed that numerical stability in the marching procedure is achieved by putting a requirement of the step size to be

$$\Delta x > \frac{1}{Re_\delta |\alpha_r|}, \tag{10}$$

where the Reynolds number appears here due to the present difference in scaling of x and α. They also mentioned that dropping of $\hat{p}_x$ relaxes the step-size restriction. Andersson *et al.* (1998) made the equations well-posed and removed the step-size restriction by adding a term proportional to the truncation error to the first-order backward Euler scheme. They performed several numerical examples and showed a stable marching procedure for arbitrarily small step sizes. However, they pointed out, if the streamwise variation of the amplitude function becomes rapid, the error from the added term may become significant.

2.3. *Energy norm*

In investigations of spatial growth a commonly used measure of the disturbance energy at a specific streamwise position is defined by

$$E(x) = \int_0^{y_{\max}} (Re_l|\hat{u}|^2 + |\hat{v}|^2 + |\hat{w}|^2)dy\, e^{-2Re_\delta \int_{x_0}^{x} \alpha_i dx}. \tag{11}$$

In order to cancel the influence of the difference in scaling and obtain similar weighting of the velocity components, the streamwise term in the energy is scaled with Re_l. Consequently, the streamwise term is $\mathcal{O}(Re_l)$ while the wall-normal and spanwise terms are $\mathcal{O}(1)$ for the algebraic instability problem, while they are of the same order for the exponential instability problem. The disturbance growth is defined by

$$G(x_0, x_1, \beta, \omega, Re_l) = \frac{E(x_1)}{E(x_0)}. \tag{12}$$

In order to compare the growth of the both instability problems in a convenient way and discuss transition prediction we need to introduce the N-factor defined as

$$N = \ln \sqrt{G} = \ln \sqrt{\frac{E(x_1)}{E(x_0)}}. \tag{13}$$

3. Algebraic Instability

3.1. *Linear scaling with Reynolds number*

As we will see in the next section, the spatial transient growth scales linearly with the Reynolds number in the large-Reynolds-number limit. This allows us to derive a transformation between the growth obtained for different parameter combinations. Let us define a Reynolds number independent growth as

$$\overline{G}(x_0, x_1, \beta, \omega) = \lim_{Re_l \to \infty} \frac{G(x_0, x_1, \beta, \omega, Re_l)}{Re_l}. \tag{14}$$

Consider the same physical problem scaled with two different length scales l and l' and the corresponding freestream velocities $U_\infty = U_\infty(l)$ and $U'_\infty = U_\infty(l')$. The dimensional quantities, denoted with a star, and the Reynolds numbers associated with the different scales can then be expressed as

$$\begin{gathered} x^* = xl = x'l', \quad \beta^* = \beta\sqrt{\frac{U_\infty}{\nu l}} = \beta'\sqrt{\frac{U'_\infty}{\nu l'}}, \\ \omega^* = \omega\frac{U_\infty}{l} = \omega'\frac{U'_\infty}{l'}, \quad Re_l = \frac{U_\infty l}{\nu}, \quad Re_{l'} = \frac{U'_\infty l'}{\nu}. \end{gathered} \tag{15}$$

Since the growth is independent of how we choose to scale the problem we have

$$G(x_0, x_1, \beta, \omega, Re_l) = G(x'_0, x'_1, \beta', \omega', Re_{l'}). \tag{16}$$

Introducing the scale ratios $c^2 = l/l'$ and $d^2 = U_\infty/U'_\infty$ and rewriting the right-hand side of (16) in the unprimed quantities using the relations in (15) yields

$$G(x_0, x_1, \beta, \omega, Re_l) = G(c^2 x_0, c^2 x_1, \frac{d}{c}\beta, \frac{d^2}{c^2}\omega, \frac{1}{c^2 d^2} Re_l). \tag{17}$$

Multiplying both sides of (17) by $c^2 d^2/Re_l$ and letting Reynolds number tend to infinity we obtain a transformation formula for the Reynolds-number-independent growth

$$c^2 d^2 \overline{G}(x_0, x_1, \beta, \omega) = \overline{G}(c^2 x_0, c^2 x_1, \frac{d}{c}\beta, \frac{d^2}{c^2}\omega). \tag{18}$$

Looking at the x-dependence in the growth, it is obvious that such a transformation is only possible when keeping the ratio x_0/x_1 constant.

3.2. *Optimal disturbances*

Now we consider solutions to (4–7) giving rise to disturbances with weak streamwise variations and α is set to zero. We are interested in maximizing the energy of the disturbance, given by (11), in the downstream position x_1 by optimizing the initial disturbance at x_0 with given initial energy. That is, we want to maximize the spatial transient growth defined by (12). Clearly, in the large-Reynolds-number limit, the maximum growth will, because of the difference in order between the terms, be obtained for initial disturbances with a zero streamwise component. Furthermore, provided that $\hat{u}_1$ is non-zero, even here because of the difference in order, $\hat{v}_1$ and $\hat{w}_1$ are neglected and the Reynolds-number-independent growth (14) can be simplified to

$$\overline{G} = \lim_{Re_l \to \infty} \frac{G}{Re_l} = \frac{\displaystyle\int_0^{y_{\max}} |\hat{u}_1|^2 dy}{\displaystyle\int_0^{y_{\max}} (|\hat{v}_0|^2 + |\hat{w}_0|^2) dy}. \tag{19}$$

Obviously, in the large-Reynolds-number limit, the optimal initial disturbance becomes independent of Re_l, which only appears as a proportional factor in the growth. If we introduce the norms

$$\|\hat{u}_1\|^2 = (\hat{u}_1, \hat{u}_1) = \int_0^{y_{\max}} |\hat{u}_1|^2 dy, \tag{20}$$

$$\|\mathbf{q}\|^2 = (\mathbf{q}, \mathbf{q}) = \int_0^{y_{\max}} (|\hat{v}_0|^2 + |\hat{w}_0|^2) dy, \tag{21}$$

where $\mathbf{q} = (\hat{v}_0, \hat{w}_0)^T$, the Reynolds-number-independent growth can be written as

$$\overline{G} = \frac{\|\hat{u}_1\|^2}{\|\mathbf{q}\|^2}. \tag{22}$$

Since the initial-boundary-value problem (4–7) is linear and homogeneous, we may adopt an input-output formulation

$$\hat{u}_1 = \mathcal{A}\mathbf{q}, \tag{23}$$

where $\mathcal{A}$ is a linear operator. The maximum Reynolds-number-independent growth may then be written

$$\overline{G}_{\max} = \max_{\mathbf{q} \neq 0} \frac{\|\hat{u}_1\|^2}{\|\mathbf{q}\|^2} = \max_{\mathbf{q} \neq 0} \frac{(\mathcal{A}^* \mathcal{A}\mathbf{q}, \mathbf{q})}{(\mathbf{q}, \mathbf{q})}. \tag{24}$$

Here $\mathcal{A}^*$ denotes the adjoint operator to $\mathcal{A}$ with respect to the chosen inner product. The maximum of $(\mathcal{A}^* \mathcal{A}\mathbf{q}, \mathbf{q})/(\mathbf{q}, \mathbf{q})$ is attained for some vector $\mathbf{q}$. In view of some basic facts from operator theory, that vector is the eigenvector corresponding to the largest eigenvalue of the eigenvalue problem

$$\mathcal{A}^* \mathcal{A}\mathbf{q} = \lambda \mathbf{q}, \tag{25}$$

and $\overline{G}_{\max}$ is the maximum eigenvalue $\lambda_{\max}$, necessarily real and non-negative. The most natural attempt to calculate the optimal initial disturbance and its associated maximum Reynolds-number-independent growth is by power iterations

$$\mathbf{q}^{n+1} = \mathcal{A}^* \mathcal{A}\mathbf{q}^n, \tag{26}$$

where the initial disturbance is scaled to the given initial energy in each iteration.

3.3. *Adjoint equations*

In order to perform the power iterations we need to know the action of the adjoint operator $\mathcal{A}^*$ on some function $\psi_1(y)$. By definition of the adjoint operator $\mathcal{A}^*$, we have

$$(\psi_1, \mathcal{A}\mathbf{q}) = (\mathcal{A}^* \psi_1, \mathbf{q}). \tag{27}$$

If we denote $\mathcal{A}^* \psi_1 = \Phi = \big(\phi_2(y), \phi_3(y)\big)^T$, the inner products can explicitly be written

$$(\psi_1, \mathcal{A}\mathbf{q}) = \int_0^{y_{\max}} \overline{\psi}_1 \hat{u}_1 dy, \tag{28}$$

$$(\mathcal{A}^* \psi_1, \mathbf{q}) = \int_0^{y_{\max}} (\overline{\phi}_2 \hat{v}_0 + \overline{\phi}_3 \hat{w}_0) dy, \tag{29}$$

where the bar denotes complex conjugate. The following adjoint system is derived in the appendix

$$\begin{array}{l} -v^*_y + i\beta w^* = 0, \\ -i\omega u^* - U u^*_x - V_y u^* - V u^*_y + V_x v^* - p^*_x = u^*_{yy} - \beta^2 u^*, \\ -i\omega v^* - U v^*_x - U_x v^* - V v^*_y + U_y u^* - p^*_y = v^*_{yy} - \beta^2 v^*, \\ -i\omega w^* - U w^*_x - V w^*_y + i\beta p^* = w^*_{yy} - \beta^2 w^*, \end{array} \tag{30}$$

where $p^*(x,y)$, $u^*(x,y)$, $v^*(x,y)$ and $w^*(x,y)$ are the adjoint variables with boundary conditions

$$\begin{array}{lll} \overline{u}^* = \overline{v}^* = \overline{w}^* = 0 & \text{at} & y = 0, \\ \overline{u}^* = \overline{w}^* = \overline{p}^* + 2V\overline{v}^* = 0 & \text{at} & y = y_{\max}. \end{array} \tag{31}$$

The individual values of $\overline{p}^*$ and $\overline{v}^*$ do not matter as long as the combination $\overline{p}^* + 2V\overline{v}^* = 0$ is fulfilled. The x-derivative in the parabolic set of equations (30) has opposite sign compared to (4–7) and is to be solved in the backward direction from the final position x_1 to the initial position x_0. Therefore the initial conditions are specified at x_1

$$\begin{array}{lll} U_1\overline{u}_1^* + \overline{p}_1^* = \overline{\psi}_1(y) & \text{at} & x = x_1, \\ \overline{v}_1^* = \overline{w}_1^* = 0 & \text{at} & x = x_1. \end{array} \tag{32}$$

The action of the adjoint operator is then given by

$$\begin{array}{lll} \overline{\phi}_2 = U_0(y)\overline{v}_0^*(y) & \text{at} & x = x_0, \\ \overline{\phi}_3 = U_0(y)\overline{w}_0^*(y) & \text{at} & x = x_0. \end{array} \tag{33}$$

3.4. *Optimization algorithm*

The adjoint-based optimization algorithm is very efficient and converges often within three or four iterations, indicating the existence of a well-separated dominating mode. The optimization problem in the large-Reynolds-number limit is defined by (24) and concerns the optimization of the initial disturbance $\mathbf{q}$ for given values of x_0, x_1, β and ω. It may be solved with the power iteration (26) and involves the following three steps.

1. Given a current guess of the initial condition $(\hat{v}_0^n, \hat{w}_0^n)$, initially arbitrary, solve equations (4–7) subject to the boundary conditions (8) and the initial conditions (9) with $\hat{u}_0 = 0$, $\hat{v}_0 = \hat{v}_0^n$ and $\hat{w}_0 = \hat{w}_0^n$.
2. Solve the adjoint equations (30) subject to the boundary conditions (31) and the initial conditions (32) with $\psi_1 = \hat{u}_1^n$ obtained from step 1.
3. Assign the new initial disturbance as the action of the adjoint operator (33) with v_0^* and w_0^* obtained from step 2 and where $\phi_2 = \hat{v}_0^{n+1}$ and $\phi_3 = \hat{w}_0^{n+1}$. After scaling the initial disturbance, making (21) to a given value, insert it into step 1 for the next iteration.

Terminate the iterations when $(G^{n+1} - G^n)/G^{n+1}$ falls below a small prescribed value.

The initial position can then be optimized with a simple polynomial optimization technique. Initially the optimal disturbances with associated growth are calculated for three initial positions. A second order polynomial is fitted to the points and the next guess of the optimal initial position is attained from the maximum of the polynomial. A new polynomial is fitted to the last three points and the procedure is proceeded until requested accuracy is achieved.

The numerical method solving the forward problem (4–9) and the backward problem (30–32) is based on a spectral collocation method involving Chebyshev polynomials. Details about the numerical scheme can be found in the papers of Andersson *et al.* (1999) and Hanifi *et al.* (1996). The numerical code is developed from the linear PSE code used by Pralits *et al.* (2002).

4. Exponential Instability

4.1. *Normalization condition*

Here we consider solutions to (4–7) giving rise to disturbances with strong streamwise variations and no terms are disregarded. As both the amplitude and phase function depend on x, one more equation is required. We also wish to satisfy the assumption that both the amplitude function and the wave number change slowly in the streamwise direction. We achieve this by specifying a normalization condition on the amplitude function

$$\int_0^{y_{\max}} (Re_l \overline{\hat{u}} \hat{u}_x + \overline{\hat{v}} \hat{v}_x + \overline{\hat{w}} \hat{w}_x) dy = 0, \tag{34}$$

where the bar again denotes complex conjugate. Other normalizations are possible and are presented in the paper by Bertolotti *et al.* (1992). The normalization condition specifies how much growth and sinusoidal variation is represented by the amplitude and phase function, respectively. The stability problem (4–9) and the normalization condition (34) have to be solved iteratively in each streamwise step. As mentioned in the previous section, details about the numerical scheme can be found in the papers of Andersson *et al.* (1999) and Hanifi *et al.* (1996) and the numerical code is developed from the linear PSE code used by Pralits *et al.* (2002). The initial conditions (9) are taken from the local theory as the least stable eigenfunction of Orr–Sommerfeld & Squire equations with corresponding eigenvalue $\alpha(x_0)$. Since the initial conditions then do not capture non-parallel effects there will be a region in the beginning of the domain that includes some errors. The size of those errors and the length of that region are dependent of how non-parallel the base flow is and will of course increase for lower Reynolds numbers.

Note that no optimization is made over the initial conditions as was done for the algebraically growing disturbances. Rather, the exponential growth is maximized in the sense that the envelope of the most amplified eigenmode is calculated. Within the PSE approximation it is difficult to incorporate the influence of mode non-normality. However an assessment of these effects for exponentially growing disturbances can be made by comparing to the work of Corbett & Bottaro (2000). They show that there is at most an additional factor of 10 contribution to the energy growth from those effects. This may add a value of one to our N-factor (13). However, the non-modal growth of TS-waves are due to the so called Orr-mechanism (Farrell 1988), which is based on initial conditions not too likely to occur in boundary layers in applications.

5. Results

5.1. *Base flow*

The linear stability analysis is done with the Falkner–Skan boundary layer as the base flow. Falkner–Skan similarity equation reads

$$f''' + ff'' + \beta_H(1 - f'^2) = 0, \tag{35}$$

subject to the boundary conditions

$$f(0) = f'(0) = 0, \quad f(\infty) = 1, \tag{36}$$

where f is the non-dimensional stream function and the prime denotes derivatives with respect to the similarity variable η. The base flow can then be

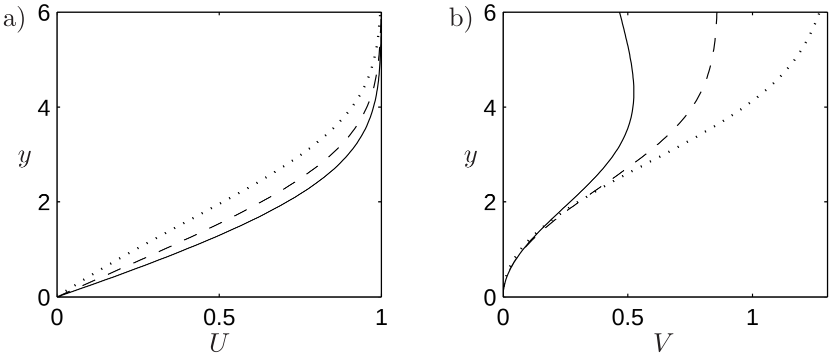

FIGURE 2. Base flow velocities from the Falkner–Skan similarity solution. Solid line: $\beta_H = 0.1$. Dashed line: $\beta_H = 0$. Dotted line: $\beta_H = -0.1$. a) Streamwise velocity. b) Wall-normal velocity.

written

$$U = U_e f', \quad V = \frac{1}{g}\big((1-\beta_H)\eta f' - f\big), \tag{37}$$

associated with the non-dimensional coordinates in the following way

$$y = g\eta, \quad U_e = x^{\frac{\beta_H}{2-\beta_H}}, \tag{38}$$

where $U_e = U_e(x)$ is the freestream velocity and

$$g = \sqrt{(2-\beta_H)\frac{x}{U_e}}. \tag{39}$$

The Hartree parameter β_H describes the freestream acceleration, as seen in (38), driven by the pressure gradient. In this work we have used three base flows with favorable, adverse and zero pressure gradients. The Hartree parameters are $\beta_H = 0.1$, $\beta_H = -0.1$ and $\beta_H = 0$, respectively. The streamwise and wall-normal base-flow velocities are shown in Figure 2. Throughout this paper, figures showing results comparing the base flows have the same line type, with solid lines for the favorable pressure gradient, dotted lines for the adverse pressure gradient and dashed lines for the zero pressure gradient.

5.2. *Optimal disturbances and streaks*

We study the optimal algebraic growth (12) of disturbances in the large-Reynolds-number limit, and its dependence of the initial position x_0, spanwise wave number β and angular frequency ω. The final position is set to $x_1 = 1$, thus the dimensional final position is l and the Reynolds number there is set to $Re_l = 10^6$. When presenting results of the β and ω-dependency, the optimal initial position is used and the growth is represented in the N-factor (13).

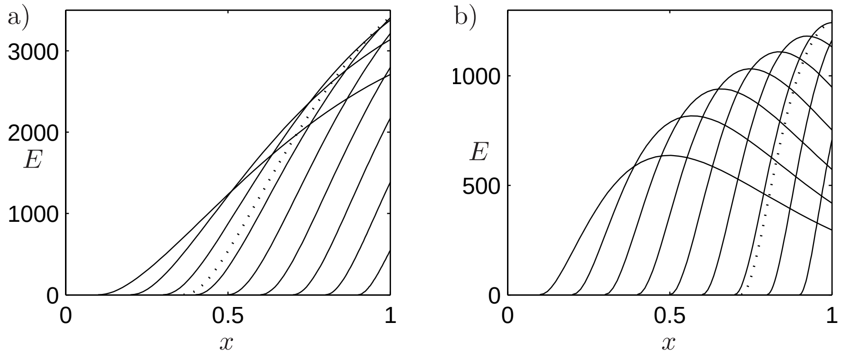

FIGURE 3. Energy growth along the plate in the Blasius boundary layer at $Re_l = 10^6$ for different initial positions, optimal case (dotted line). a) $\beta = 0.5$ and $\omega = 0$. b) $\beta = 1$ and $\omega = 5$.

Andersson *et al.* (1999) and Luchini (2000) used the leading edge as the initial position in their calculations. However, in base flows with non-zero pressure gradients it is not possible to perform accurate calculations starting very close to the leading edge due to the behavior of the similarity solution. Besides that problem we wish to investigate the impact of different x_0 on the growth. Figure 3a shows the energy growth along the plate for different initial positions for optimal disturbances with $\beta = 0.5$ and $\omega = 0$ in the Blasius boundary layer. The dotted line shows the optimal growth originating from the optimal initial position $x_0 = 0.36$. Disturbances introduced closer to the leading edge grow in a slower rate. On the other hand, disturbances introduced further downstream do not have distance enough to grow as much before the final position. An interpretation of the slower growth rate for disturbances introduced close to the leading edge is the influence of the boundary layer thickness on the lift-up effect. Upstream of the optimal initial position the boundary layer is not thick enough for the optimal distortion of fluid elements. Furthermore, the optimal disturbance introduced upstream will not have the optimal shape at a position further downstream. The growth rate seems to increase for disturbances introduced further downstream where the boundary layer is thicker.

Figure 3b again shows the energy growth in the Blasius boundary layer for different initial positions but for optimal disturbances with $\beta = 1$ and $\omega = 5$. Here it is seen that the viscous dissipation is more dominat and the energy soon starts to decay. The dotted line showing the optimal growth originates in this case from the initial position $x_0 = 0.72$. Since the adjoint-based optimization technique optimizes the initial disturbance with respect to the disturbance energy in the final position and we are interested in the maximum energy in the domain, the true optimum only results when the maximum energy appears in the final position. The optimization of the initial position not only gives

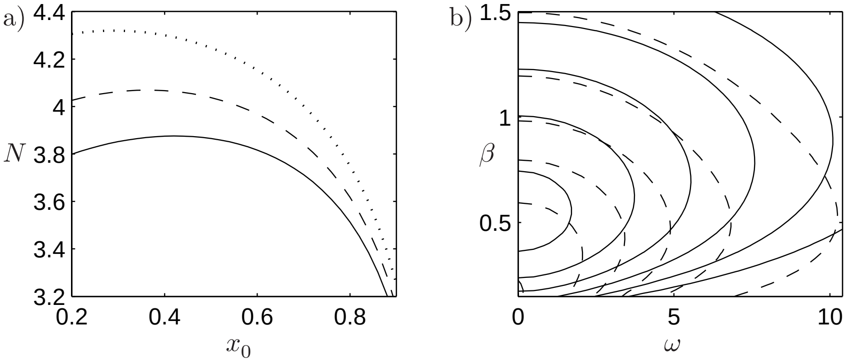

FIGURE 4. a) N-factor vs x_0 at $Re_l = 10^6$ with $\beta = 0.5$ and $\omega = 0$. Lines as in Figure 2. b) Contours of constant N-factor (solid lines) with values, from right to left, 3 to 4 with contour spacing 0.2 and contours of constant optimum x_0 (dashed lines) with values, from left to right, 0.3 to 0.8 with contour spacing 0.1, for optimal disturbances in the Blasius boundary layer. $Re_l = 10^6$.

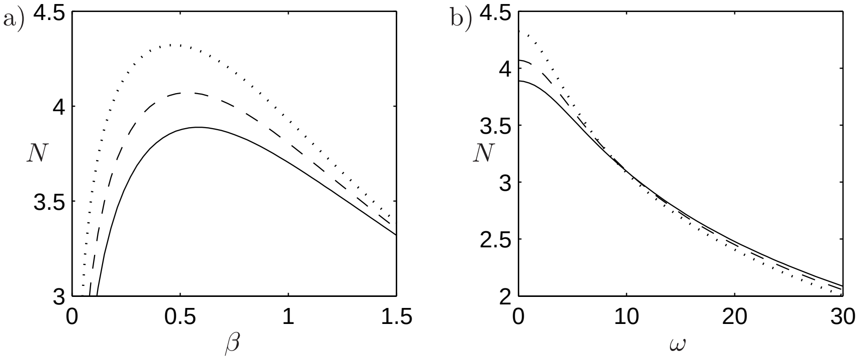

FIGURE 5. Lines as in Figure 2. $Re_l = 10^6$. a) N-factor vs β. $\omega = 0$. b) N-factor vs ω. $\beta = 0.47, 0.53, 0.58$.

the optimal growth, it also ensures that the maximum energy is reached at the final position.

Figure 4a shows the x_0-dependence of the N-factor for optimal disturbances with $\beta = 0.5$ and $\omega = 0$ in the different base flows. The optimal initial position moves downstream with decreased pressure gradient. The particular values in this case are $x_0 = 0.29$ for the adverse-pressure-gradient base flow and $x_0 = 0.42$ for the favorable-pressure-gradient base flow. Contours of constant N-factor (solid lines) and constant optimal initial position (dashed lines) for optimal disturbances in the Blasius boundary layer can be seen in Figure 4b.

β_H	x_0	β	ω	N	G
0.1	0.45	0.58	0	3.9	$0.0024Re_l$
0	0.37	0.53	0	4.1	$0.0034Re_l$
-0.1	0.28	0.47	0	4.3	$0.0057Re_l$

TABLE 3. Optimal parameters for algebraically growing disturbances in the three base flows at $Re_l = 10^6$.

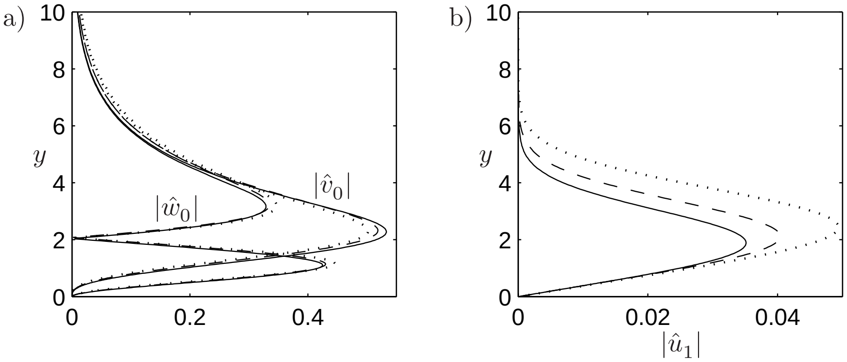

FIGURE 6. Lines as in Figure 2. $Re_l = 10^6$. Parameters as in Table 3. a) Optimal initial disturbances. b) Final disturbance.

The optimal initial position moves downstream with increasing spanwise wave number and angular frequency.

From now on the optimized initial position will be used and we turn our attention to the β and ω-dependency. First we investigate how the N-factor depends on β for the different base flows and the results are presented in Figure 5a. The optimal angular frequency $\omega = 0$ is used. The optimal β increases with decreased pressure gradient and the particular values are $\beta = 0.47$, $\beta = 0.53$ and $\beta = 0.58$. Secondly, Figure 5b shows how the N-factors in the different base flows depend on ω. Here the optimal β-value for the respective flow case is used.

The results in Figures 4a and 5a also show the effect of streamwise pressure gradient. The algebraic energy growth increases with decreased streamwise pressure gradient of the base flow. That is consistent with the work by Tumin (2001), which used a slightly different spatial model, and the temporal stability analysis by Corbett & Bottaro (2000).

The optimal x_0, β and ω and their corresponding growth in terms of N and G for the three base flows are summarized in Table 3. The associated optimal initial disturbances are shown in Figure 6a and when the spanwise periodic dependence is incorporated they take the form of vortices in the crossflow plane. Their shape, especially the normal scale, is rather insensitive to the change of

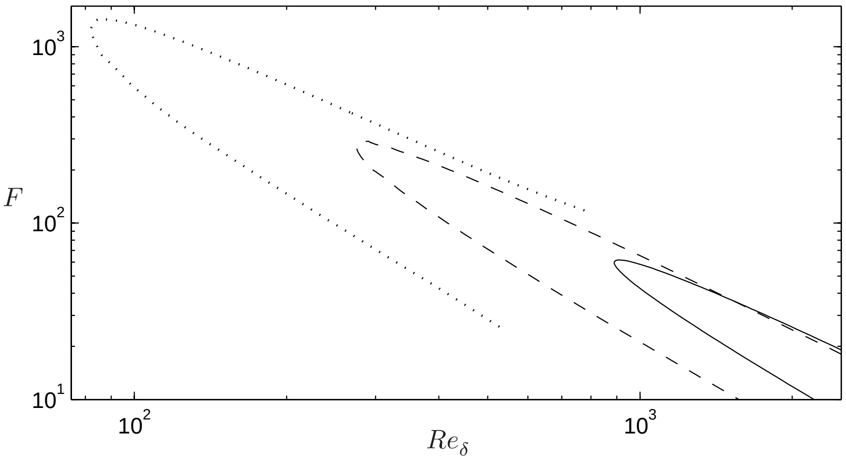

FIGURE 7. Lines as in Figure 2. Neutral curves in the $Re_\delta - F$ plane for $\beta = 0$.

pressure gradient in the base flow. The downstream response of the optimal disturbances, shown in Figure 6b, take the form of streamwise elongated streaks when the spanwise periodic dependence is incorporated.

5.3. *Tollmien–Schlichting waves*

We study the exponential growth (12) of modal disturbances, historically referred to as Tollmien–Schlichting waves, and its dependence of the spanwise wave number β and angular frequency ω. The Reynolds number is $Re_l = 10^6$. In the case of optimal disturbances we studied the dependence of the initial position of the disturbance. Here, the growth is maximized in the sense that the most amplified eigenmode is calculated within the unstable region of $x \in [0, 1]$. That means that x_0 is chosen as the lower-branch neutral point and x_1 is either equal to 1 or the upper-branch neutral point, if it appears for a lower value. However, since the initial condition does not capture non-parallel effects and introduces a region of errors, the equations are solved from an initial position sufficiently upstream of x_0 in order to remove those errors.

The disturbance is said to be unstable if the physical growth rate defined as

$$\sigma = \frac{1}{Re_\delta} \frac{1}{\sqrt{\hat{E}}} \frac{\partial \sqrt{\hat{E}}}{\partial x} - \alpha_i, \tag{40}$$

where $\hat{E}$ is the amplitude function energy, is greater than zero and the neutral point is defined as the location where $\sigma = 0$. Figure 7 shows the neutral curves in the $Re_\delta - F$ plane, where $F = 10^6\omega/Re_l$ is the reduced frequency. The critical Reynolds numbers for the favorable, zero and adverse-pressure-gradient base flows are $Re_\delta = 889$, $Re_\delta = 275$ and $Re_\delta = 82$, respectively.

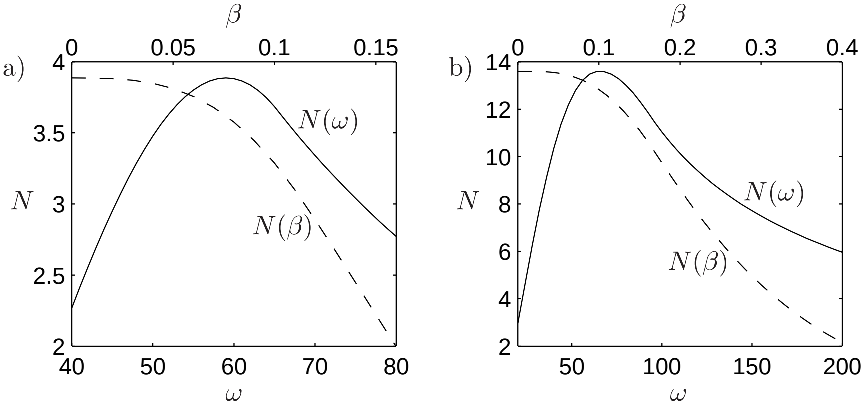

FIGURE 8. N-factor as function of ω (solid lines) and β (dashed lines) at $Re_l = 10^6$. a) Blasius boundary layer. $N(\beta)$: $\omega = 59$, $N(\omega)$: $\beta = 0$ b) Adverse-pressure-gradient base flow. $N(\beta)$: $\omega = 66$, $N(\omega)$: $\beta = 0$.

β_H	x_0	β	ω	N
0	0.31	0	59	3.9
-0.1	0.11	0	66	13.6

TABLE 4. Optimal parameters for exponentially growing disturbances for the zero and adverse-pressure-gradient base flows at $Re_l = 10^6$.

Since the favorable-pressure-gradient base flow is quite stable for exponentially growing disturbances, we will not investigate it further in this section. Instead we turn our attention to the β and ω-dependency of the two other base flows. Figures 8a and 8b show the results for the zero and adverse-pressure-gradient base flow, respectively. The solid lines show the N-factor as a function of ω and the optimal wave number $\beta = 0$ is used. The ω-labels are shown on the lower axis. The dashed lines show the N-factor as function of β and the optimal angular frequencies $\omega = 59$ and $\omega = 66$ in respective case are used. The β-labels are shown on the upper axis.

The optimal β and ω and their corresponding N-factors and lower-branch neutral points are summarized in Table 4. The associated streamwise amplitude functions at x_0 and x_1, which is equal to 1 for the optimal cases, are shown in Figures 9a and 9b, respectively.

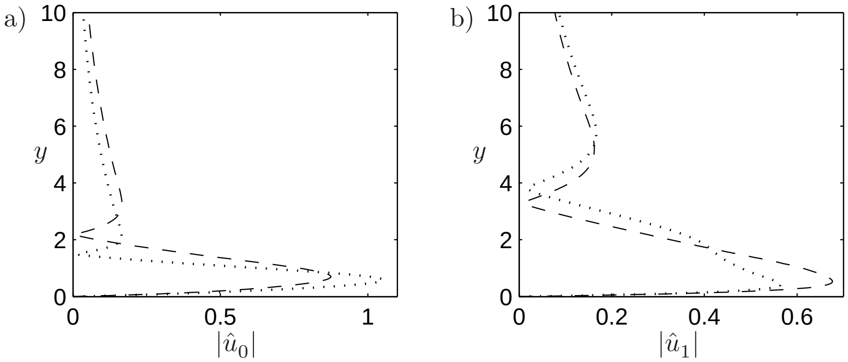

FIGURE 9. Lines as in Figure 2. $Re_l = 10^6$. Parameters as in Table 4. The most amplified streamwise amplitude functions at a) x_0 and b) x_1.

5.4. *Comparison of algebraic and exponential growth*

Now that we have studied the two different growth scenarios we compare the growth of optimal and modal disturbances. Figure 10a shows the envelope curves of the maximal algebraic and exponential N-factors vs Re_l. The algebraic growth in the large-Reynolds-number limit is proportional to Re_l and thus represented as the straight lines.

Figures 10b, 10c and 10d show contours of constant N-factor in the ω-β plane at $Re_l = 10^6$ for the favorable, zero and adverse-pressure-gradient base flow, respectively. The locations of the peak values are indicated by crosses ($\times$) in the figures. In the case of the favorable-pressure-gradient base flow, only the algebraic growth appears, whereas for the Blasius boundary layer, the algebraic and exponential growth are comparable. For the adverse-pressure-gradient base flow on the other hand, the exponential growth is dominating. The parameters for the maximum growth of optimal and modal disturbances are summarized in Table 3 and 4, respectively.

5.5. *Transition prediction*

So far we have compared the growth of the disturbances and not their actual energy value. To draw any conclusions about when transition occurs, one has to know the initial disturbance energy, and thus know the receptivity process. Typical sources from which disturbances can enter the boundary layer are freestream turbulence, surface roughness, acoustic waves and vibrations. At low disturbance levels transition occurs at a N-factor between 8 and 11, depending of the definition of transition. At higher disturbance levels that number decreases. TS-wave receptivities to surface roughness, acoustic waves and vibrations are stronger than the receptivity to freestream turbulence, while streaks mainly are created through receptivity to freestream turbulence. Here

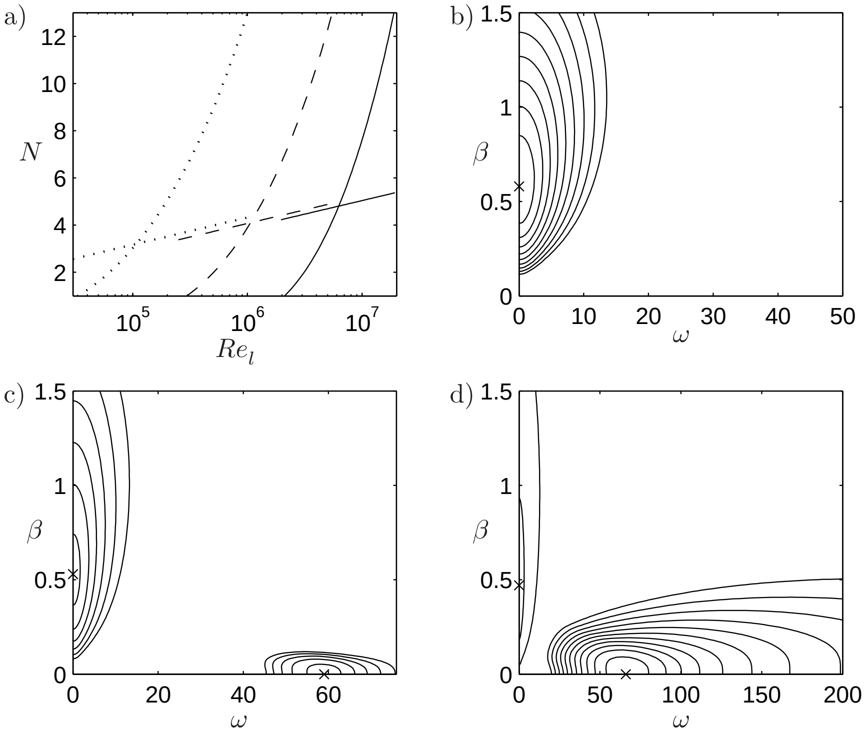

FIGURE 10. a) Envelope curves of the maximal algebraic and exponential growth. Lines as in Figure 2. $Re_l = 10^6$. b) Contours of constant N-factor for the favorable-pressure-gradient base flow with contour spacing 0.1. The maximum growth has $N = 3.9$ at $\beta = 0.58$ and $\omega = 0$. c) Blasius boundary layer with contour spacing 0.2. The maximum algebraic growth has $N = 4.1$ at $\beta = 0.53$ and $\omega = 0$ and the maximum exponential growth has $N = 3.9$ at $\beta = 0$ and $\omega = 59$. d) Adverse-pressure-gradient base flow with contour spacing 1. The maximum algebraic growth has $N = 4.3$ at $\beta = 0.47$ and $\omega = 0$ and the maximum exponential growth has $N = 13.6$ at $\beta = 0$ and $\omega = 66$. $Re_l = 10^6$. Crosses ($\times$) indicate the locations of the peak values.

we will concern ourself with receptivity to freestream turbulence. As is usual in linear transition prediction we incorporate the receptivity in the N-factor at transition.

Mack (1977) proposed a receptivity model (1) for the N-factor at transition associated with exponentially growing disturbances. The model is based on parallel, linear stability analysis for exponentially growing TS-waves in the Blasius boundary layer, correlated with experiments collected by Dryden (1959). The model, shown as the dotted line in Figure 11a, is misleading, however, since the transition process in these experiments most likely is a result of bypass transition of streaky structures, not TS-waves. A more appropriate model is that of Andersson *et al.* (1999). That model, eq. (2), correlates the transition Reynolds number associated with bypass transition due to streamwise streaks, based on the maximum algebraic growth of optimal disturbances in the Blasius boundary layer. It is shown as the solid line in Figure 11a. Note that the model of Mack gives a lower N-value for transition than the model based on transient growth, something not supported by available experimental data. We will complement the transition model of Andersson *et al.* (1999) with the addition of base flows with various pressure gradients. The model is based on three assumptions.

1. We assume that the initial disturbance energy is proportional to the freestream-turbulence energy
$$E(x_0) = Tu^2, \tag{41}$$
for isotropic turbulence with the freestream-turbulence level defined as $Tu = \sqrt{\overline{u'^2}}/U_\infty$. Here u' is the fluctuating streamwise velocity in the freestream and the overbar denotes the temporal mean.
2. We assume that the initial disturbance grows with the optimal rate
$$E(x_1) = GE(x_0) = \overline{G}Re_l E(x_0). \tag{42}$$
3. We assume that transition occurs when the final energy reaches a specific value E_T, regardless of the pressure gradient of the base flow
$$E(x_1) = E_T. \tag{43}$$

Combining assumptions (41)-(43) yields the transition model
$$\sqrt{Re_T}Tu = \frac{k}{\sqrt{\overline{G}}}, \tag{44}$$
where k should be constant. Using the same correlation as Andersson *et al.* (1999) and the optimal Reynolds-number-independent growth in the Blasius boundary layer gives $k = 0.70$. Note that our model differs in the sense that we have used the growth from the optimal initial position and not the leading edge.

The influence of freestream turbulence on the generation of TS-waves is not conclusive. In fact, Boiko *et al.* (1994) made experiments on the behavior of controlled TS-waves, introduced by means of a vibrating ribbon, in a boundary layer subjected to $Tu = 1.5\%$. The measured amplification rates for the waves in the presence of the turbulence generating grid were smaller that for regular TS-waves, and damping set in further upstream than in the absence of the turbulence generating grid. Thus we make the simple assumption that transition resulting from exponentially growing disturbances occurs at $N = 8$, the dashed line in Figure 11a, irrespective of the freestream turbulence level.

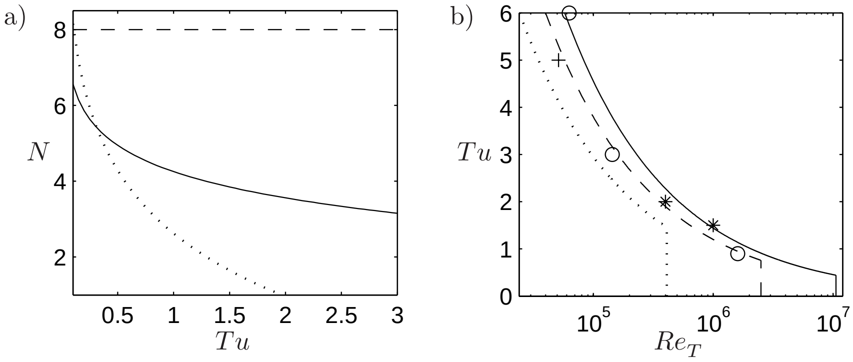

FIGURE 11. a) Predicted N-factor at transition vs Tu given in percent for algebraic (solid line) and exponential (dashed line) growth. Dotted line: Model by Mack (1977). b) Lines as in Figure 2. Predicted transition contour in the Re_T-Tu plane. Tu is given in percent. The straight part of the lines corresponds to transition due to modal growth and the curved part to bypass transition. Experimental data for the Blasius boundary layer from Matsubara & Alfredsson (2001) ($*$) and Roach & Brierley (1992) ($\circ$). Numerical data from Yang & Voke (1991) ($+$).

Figure 11b shows the transition Reynolds number based on the results from the linear stability analysis and the transition model discussed above for freestream turbulence. The straight part of the lines represents the transition Reynolds number for exponentially growing modal disturbances and the curved part represents bypass transition. For high freestream turbulence levels, transition occurs as a result of the breakdown of streaky structures and for low freestream turbulence levels as a result of exponentially growing disturbances. The cross-over point occurs where the bypass transition model predicts a higher transition Reynolds number than for the exponentially growing disturbances. According to the model, bypass transition occurs in the Blasius boundary layer (dashed lines) for a freestream-turbulence level higher than 0.76%. Similar results has been found in experiments. Suder *et al.* (1988) found in their experiment that the bypass mechanism prevailed for freestream-turbulence levels of 0.65% and higher. Kosorygin & Polyakov (1990) suggested that TS-waves and streaks can co-exist and interact for freestream-turbulence levels up to approximately 0.7%. However, our model does not account for the interaction between TS-waves and streaks.

6. Conclusions

The energy growth of eigenmodes and non-modal optimal disturbances has been investigated, by means of linear equations valid both for the exponential and algebraic growth scenarios, in the Falkner–Skan boundary layer with favorable, adverse and zero pressure gradients.

First, the algebraic growth of optimal disturbances in the large-Reynolds-number limit was studied. It was found that the initial streamwise position, where the disturbance is introduced in the boundary layer, has a significant impact on the growth. The optimal initial position moves downstream with increasing wave number and angular frequency of the disturbance and with decreasing pressure gradient of the base flow. Furthermore, the optimal spanwise wave number increases with decreased pressure gradient while the optimal angular frequency is equal to zero.

Secondly, the exponential growth of modal disturbances within the unstable region was studied. It was found that the optimal angular frequency increases with decreasing pressure gradient while the optimal spanwise wave number is equal to zero, as expected.

In both the algebraic and exponential growth scenarios, the growth increases with decreasing pressure gradient, although the effect is much more pronounced for the exponential growth. Therefore, in a comparison of the two different growth scenarios at $Re_l = 10^6$, the algebraic growth is much larger for the favorable-pressure-gradient base flow and the exponential growth is much larger for the adverse-pressure-gradient base flow, while they are comparable for the Blasius boundary layer.

Finally, a unified transition-prediction method incorporating the influence of freestream turbulence was presented. It was shown that bypass transition due to streamwise streaks occurs for flows with a moderate to high level of freestream turbulence. The freestream-turbulence level for which bypass transition occurs decreases with increased pressure gradient of the base flow.

Acknowledgment

This work was founded by the Swedish Energy Agency (Energimyndigheten). We also wish to thank Ardeshir Hanifi for letting us use his Fortran code and Jan Pralits for valuable discussions.

Appendix

Derivation of the adjoint equations

In order to derive the adjoint equations for the algebraic optimization problem, we disregard terms including α and the $\hat{p}_x/Re_\delta^2$ term in the streamwise momentum equation. We rewrite the forward equations (4–7) in matrix form

$$\mathbf{A}\mathbf{f} + \mathbf{B}\mathbf{f}_y + \mathbf{C}\mathbf{f}_{yy} + \mathbf{D}\mathbf{f}_x = 0, \tag{45}$$

where the state vector $\mathbf{f} = (\hat{u}, \hat{v}, \hat{w}, \hat{p})^T$ and

$$\mathbf{A} = \begin{bmatrix} 0 & 0 & i\beta & 0 \\ U_x + \beta^2 - i\omega & U_y & 0 & 0 \\ V_x & V_y + \beta^2 - i\omega & 0 & 0 \\ 0 & 0 & \beta^2 - i\omega & i\beta \end{bmatrix},$$

$$\mathbf{B} = \begin{bmatrix} 0 & 1 & 0 & 0 \\ V & 0 & 0 & 0 \\ 0 & V & 0 & 1 \\ 0 & 0 & V & 0 \end{bmatrix},$$

$$\mathbf{C} = \begin{bmatrix} 0 & 0 & 0 & 0 \\ -1 & 0 & 0 & 0 \\ 0 & -1 & 0 & 0 \\ 0 & 0 & -1 & 0 \end{bmatrix},$$

$$\mathbf{D} = \begin{bmatrix} 1 & 0 & 0 & 0 \\ U & 0 & 0 & 0 \\ 0 & U & 0 & 0 \\ 0 & 0 & U & 0 \end{bmatrix}.$$

Let us define an inner product between two vectors $\mathbf{u}$ and $\mathbf{v}$ as follows

$$(\mathbf{u}, \mathbf{v}) = \int_{x_0}^{x_1} \int_0^{y_{\max}} \mathbf{u}^* \mathbf{v} \, dy dx, \tag{46}$$

and the adjoint-state vector $\mathbf{g} = (p^*, u^*, v^*, w^*)^T$. The star on the adjoint-state variables is just traditional notation while a star on a vector or matrix denotes the conjugate transpose. Now we take the inner product between $\mathbf{g}$ and the left-hand side of the forward equation system (45) and move the derivatives from $\mathbf{f}$ to $\mathbf{g}$ by integration by parts

$$\begin{gathered} (\mathbf{g}, \mathbf{A}\mathbf{f} + \mathbf{B}\mathbf{f}_y + \mathbf{C}\mathbf{f}_{yy} + \mathbf{D}\mathbf{f}_x) = \\ \big((\mathbf{A}^* - \mathbf{B}_y^* - \mathbf{D}_x^*)\mathbf{g} - \mathbf{B}^*\mathbf{g}_y + \mathbf{C}^*\mathbf{g}_{yy} - \mathbf{D}^*\mathbf{g}_x, \mathbf{f}\big) + \\ \int_{x_0}^{x_1} \langle \mathbf{B}^*\mathbf{g}, \mathbf{f} \rangle \Big|_0^{y_{\max}} dx + \int_{x_0}^{x_1} \langle \mathbf{C}^*\mathbf{g}, \mathbf{f}_y \rangle \Big|_0^{y_{\max}} dx - \\ \int_{x_0}^{x_1} \langle \mathbf{C}^*\mathbf{g}_y, \mathbf{f} \rangle \Big|_0^{y_{\max}} dx + \int_0^{y_{\max}} \langle \mathbf{B}^*\mathbf{g}, \mathbf{f} \rangle \Big|_{x_0}^{x_1} dy. \end{gathered} \tag{47}$$

Since the left-hand side of the derivation (47) is equal to zero due to the state equations, the right-hand side also has to be zero. By setting each boundary term to zero we are ending up with a set of equations for the adjoint-state variables

$$(\mathbf{A}^* - \mathbf{B}_y^* - \mathbf{D}_x^*)\mathbf{g} - \mathbf{B}^*\mathbf{g}_y + \mathbf{C}^*\mathbf{g}_{yy} - \mathbf{D}^*\mathbf{g}_x = 0, \tag{48}$$

and the boundary terms can explicitly be written

$$\int_{x_0}^{x_1} \langle \mathbf{B}^*\mathbf{g}, \mathbf{f} \rangle \Big|_0^{y_{\max}} dx =$$

$$\int_{x_0}^{x_1} \left(V\overline{u}^*\hat{u} + (\overline{p}^* + V\overline{v}^*)\hat{v} + V\overline{w}^*\hat{w} + \overline{v}^*\hat{p}\right)\Big|_0^{y_{\max}} dx = 0, \tag{49}$$

$$\int_{x_0}^{x_1} \langle \mathbf{C}^*\mathbf{g}, \mathbf{f}_y\rangle \Big|_0^{y_{\max}} dx = \int_{x_0}^{x_1} (-\overline{u}^*\hat{u}_y - \overline{v}^*\hat{v}_y - \overline{w}^*\hat{w}_y)\Big|_0^{y_{\max}} dx = 0, \tag{50}$$

$$\int_{x_0}^{x_1} \langle \mathbf{C}^*\mathbf{g}_y, \mathbf{f}\rangle \Big|_0^{y_{\max}} dx = (-\overline{u}^*_y\hat{u} - \overline{v}^*_y\hat{v} - \overline{w}^*_y\hat{w})\Big|_0^{y_{\max}} dx = 0, \tag{51}$$

$$\begin{gathered}\int_0^{y_{\max}} \langle \mathbf{D}^*\mathbf{g}, \mathbf{f}\rangle \Big|_{x_0}^{x_1} dy = \\ \int_0^{y_{\max}} \left((\overline{p}^* + U\overline{u}^*)\hat{u} + U\overline{v}^*\hat{v} + U\overline{w}^*\hat{w}\right)\Big|_{x_0}^{x_1} dy = 0.\end{gathered} \tag{52}$$

The necessary boundary conditions can be determined by the three first boundary terms (49–51)

$$\begin{array}{lll} \overline{u}^* = \overline{v}^* = \overline{w}^* = 0 & \text{at} & y = 0, \\ \overline{u}^* = \overline{w}^* = \overline{p}^* + 2V\overline{v}^* = 0 & \text{at} & y = y_{\max}. \end{array} \tag{53}$$

Moreover, by identifying ψ_1 and Φ in the last boundary term (52) the initial conditions and the action of the adjoint operator can be stated

$$\begin{aligned} &U_1\overline{u}_1^* + \overline{p}_1^* = \overline{\psi}_1, \\ &\overline{v}_1^* = \overline{w}_1^* = 0, \end{aligned} \tag{54}$$

$$\begin{aligned} \overline{\phi}_2 &= U_0\overline{v}_0^*, \\ \overline{\phi}_3 &= U_0\overline{w}_0^*. \end{aligned} \tag{55}$$

References

Abu-Ghannam, B. & Shaw, R. 1980 Natural transition of boundary layers - the effects of turbulence, pressure gradient, and flow history. *J. Mech. Eng. Sci.* **22** (5), 213–228.

Andersson, P., Berggren, M. & Henningson, D. 1999 Optimal disturbances and bypass transition in boundary layers. *Phys. Fluids* **11** (1), 134–150.

Andersson, P., Henningson, D. & Hanifi, A. 1998 On a stabilization procedure for the parabolic stability equations. *J. Eng. Math.* **33**, 311–332.

Bertolotti, F. P., Herbert, T. & Spalart, P. R. 1992 Linear and nonlinear stability of the Blasius boundary layer. *J. Fluid Mech.* **242**, 441–474.

Boiko, A., Westin, K., Klingmann, B., Kozlov, V. & Alfredsson, P. 1994 Experiments in a boundary layer subjected to free stream turbulence. Part 2. The role of TS-waves in the transition process. *J. Fluid Mech.* **281**, 219–245.

Butler, K. & Farrell, V. 1992 Three-dimensional optimal pertubations in viscous shear flow. *Phys. Fluids A* **4** (8), 1637–1650.

Corbett, P. & Bottaro, A. 2000 Optimal pertubations for boundary layers subject to stream-wise pressure gradient. *Phys. Fluids* **12** (1), 120–130.

van Driest, E. & Blumer, C. 1963 Boundary layer transition: Freestream turbulence and pressure gradient effects. *AIAA J.* **1**, 1303–1306.

Dryden, H. 1959 Transition from laminar to turbulent flow. In *Turbulent flows and heat transfer* (ed. C. Lin), pp. 1–74. N.J.: Princeton Univ. Press.

Ellingsen, T. & Palm, E. 1975 Stability of linear flow. *Phys. Fluids* **18** (4), 487–488.

Farrell, B. 1988 Optimal exitation of pertubations in viscous shear flow. *Phys. Fluids* **31** (8), 2093–2102.

Floryan, J. & Saric, W. 1979 Stability of Görtler vortices in boundary layers. *AIAA J.* **20** (3), 316–324.

Haj-Hariri, H. 1994 Characteristics analysis of the parabolized stability equations. *Stud. Appl. Math.* **92**, 41–53.

Hall, P. 1983 The linear development of Görtler vortices in growing boundary layers. *J. Fluid Mech.* **130**, 41–58.

Hanifi, A., Schmid, P. & Henningson, D. 1996 Transient growth in compressible boundary layer flow. *Phys. Fluids* **8** (3), 826–837.

Hein, S., Stolte, A. & Dallmann, U. 1999 Identification and analysis of nonlinear transition scenarios using NOLOT/PSE. *Z. Angew. Math. Mech.* **79**, S109–S112.

Henningson, D., Lundbladh, A. & Johansson, A. 1993 A mechanism for bypass transition from localized disturbances in wall-bounded shear flows. *J. Fluid Mech.* **250**, 169–238.

Herbert, T. 1997 Parabolized stability equations. *Annu. Rev. Fluid Mech.* **29**, 245–283.

Hultgren, L. & Gustavsson, L. 1981 Algebraic growth of disturbances in a laminar boundary layer. *Phys. Fluids* **24** (6), 1000–1004.

van Ingen, J. 1956 Suggested semi-emperical method for the calculation of the boundary layer transition region. *Tech. Rep.* UTH-74. Dep. of Aero. Eng., University of Technology, Delft.

Klebanoff, P. 1971 Effect of freestream turbulence on the laminar boundary layer. *Bull. Am. Phys. Soc.* **10**, 1323.

Kosorygin, V. & Polyakov, N. 1990 Laminar boundary layers in turbulent flows. In *Laminar-Turbulent Transition* (eds. D. Arnal & R. Michel), pp. 573–578. Springer-Verlag.

Landahl, M. 1980 A note on an algebraic instability of inviscid parallel shear flows. *J. Fluid Mech.* **98** (2), 243–251.

Li, F. & Malik, M. R. 1994 Mathematical nature of parabolized stability equations. In *4th IUTAM Symp. on Laminar-Turbulent transition, Sendi, Japan* (ed. R. Kobayashi), pp. 205–212. Springer-Verlag.

Li, F. & Malik, M. R. 1996 On the nature of PSE approximation. *Theor. and Comp. Fluid Dyn.* **8**, 253–273.

Luchini, P. 1996 Reynolds-number-independent instability of the boundary layer over a flat surface. *J. Fluid Mech.* **327**, 101–115.

Luchini, P. 2000 Reynolds-number-independent instability of the boundary layer over a flat surface: optimal perturbations. *J. Fluid Mech.* **404**, 289–309.

Mack, L. 1977 Transition prediction and linear stability theory. In *AGARD-CP-224*, pp. 1–1 to 1–22. NATO, Paris.

Matsubara, M. & Alfredsson, P. 2001 Disturbance growth in boundary layers subjected to free-stream turbulence. *J. Fluid Mech.* **430**, 149–168.

Pralits, J., Hanifi, A. & Henningson, D. 2002 Adjoint-based optimization of steady suction for disturbance control in incompressible flows. *J. Fluid Mech.* **467**, 129–161.

Reddy, S. & Henningson, D. 1993 Energy growth in viscous channel flows. *J. Fluid Mech.* **252**, 209–238.

Roach, P. & Brierley, D. 1992 The influence of a turbulent free-stream on zero pressure gradient transitional boundary layer development. I. Test cases T3A and T3B. In *Numerical Simulation of Unsteady Flows and Transiton to Turbulence* (eds. O. Pironneau, W. Rodi, I. Ryhming, A. Savill & T. Truong), pp. 303–316. Cambridge University Press.

Smith, A. & Gamberoni, N. 1956 Transition, pressure gradient and stability theory. *Tech. Rep.* ES 26388. Douglas Aircraft Co., EL Segundo, Calif.

Suder, K., O'Brien, J. & Reshotko, E. 1988 Experimental study of bypass transition in a boundary layer. *NASA TM* **100913**.

Tumin, A. 2001 A model of spatial algebraic growth in a boundary layer subjected to a streamwise pressure gradient. *Phys. Fluids* **13** (5), 1521–1523.

Tumin, A. & Reshotko, E. 2003 Optimal disturbances in compressible boundary layers. *AIAA Paper* 2003-0792.

Westin, K., Boiko, A., Klingmann, B., Kozlov, V. & Alfredsson, P. 1994 Experiments in a boundary layer subjected to free stream turbulence. Part 1. Boundary layer structure and receptivity. *J. Fluid Mech.* **281**, 193–218.

Yang, Z. Y. & Voke, P. R. 1991 Numerical simulation of transition under turbulence. *Tech. Rep.* ME-FD/91.01. Dept. Mech. Eng. University of Surrey.

Paper 2

A Numerical and Experimental Study of the Blasius Wall Jet

By Ori Levin[1], Valery G. Chernoray[2], Maria V. Litvinenko[2], Lennart Löfdahl[2] & Dan S. Henningson[1,3]

[1]Department of Mechanics, Royal Institute of Technology, SE-100 44 Stockholm, Sweden
[2]Thermo and Fluid Dynamics, Chalmers University of Technology, SE-412 96 Göteborg, Sweden
[3]The Swedish Defence Research Agency (FOI), Aeronautics Division (FFA), SE-172 90 Stockholm, Sweden

A plane wall-jet flow is investigated experimentally, theoretically and numerically. The measured base flow is matched to a boundary-layer solution developing from a coupled Blasius boundary layer and shear layer downstream of the slot. Linear stability analysis is performed, revealing high instability of two-dimensional eigenmodes and non-modal streaks. It is shown that the calculated characteristics agree well with the experiments. The nonlinear stage of laminar flow breakdown is studied with both three-dimensional direct numerical simulations and experimentation. In the direct numerical simulation, an investigation of the nonlinear interaction between the eigenmodes and the streaks is made. It is demonstrated that the streaks play an important role in the breakdown process, where their growth is transformed from algebraic to exponential as they become part of the secondary instability of the two-dimensional waves.

---

1. Introduction

1.1. *The wall jet*

A wall jet may generally be considered as a flow field that is produced by the injection of a high-velocity fluid in a thin layer close to a surface. The ambient fluid may be either quiescent or moving at a certain velocity, which typically is lower than the velocity of the injected jet. Such flows are of great interest to engineers, for instance in film cooling of gas turbine blades and combustion chambers, in defrosters for automobiles, and in boundary layer control of airfoils and flaps. Fundamentally, a wall jet may in principle be treated as a two-layer flow with an inner region that reaches, in the normal direction, up to the point of maximum velocity and an outer region above. The inner region is most similar to a wall boundary layer and the outer region has a flow pattern that is closely related to a free shear layer. The major characteristics of these layers are different, and in a wall jet, the interaction between these regions forms a complex flow field.

Two-dimensional wall jets have been considered since the mid fifties and in a classical work by Glauert (1956), it was found that a similarity solution exists for the laminar wall jet. This solution was obtained explicitly and is valid far downstream from the position of the fluid injection. Glauert's solution has provided a good basis for a number of subsequent stability investigations.

1.2. *Two-dimensional behavior*

The temporal linear stability of the Glauert wall jet was examined theoretically by Chun & Schwarz (1967) by solving the Orr–Sommerfeld equation. Bajura & Szewczyk (1970) performed hot-wire measurements in an air wall jet and confirmed the existence of the Glauert wall jet. Furthermore, the stability of the flow to natural disturbances was studied and the streamwise velocity fluctuation was found to exhibit two large peaks, one peak on each side of the wall jet core. The amplification rate of the outer peak was found to be larger, and hence, the instability of the wall jet is controlled by the outer region. The results are in qualitative agreement with the linear stability theory by Chun & Schwarz (1967). The dominance of the outer region was also reported by Bajura & Catalano (1975), who investigated the whole transition process of a water wall jet. By using flow visualization, they observed the following five stages in natural transition: (i) formation of discrete vortices in the outer region; (ii) vortex pairing in the outer region, resulting in a doubling of the disturbance wavelength, coupled with the possible pairing of vortex-like motions in the inner region; (iii) lift-off of the wall jet into the ambient fluid; (iv) onset of turbulent motion; (v) re-laminarization of the upstream flow, until the next vortex pairing.

By solving the Orr–Sommerfeld equation, Mele *et al.* (1986) clarified the existence of two unstable modes in the wall jet. One mode, unstable at low disturbance frequencies, shows the highest amplitude close to the inflection point in the outer region of the wall jet, while the other mode, unstable at higher frequencies, attains the highest amplitude close to the wall. They concluded that the inviscid instability in the outer region governs the large-scale disturbances while the viscous instability governs the small-scale disturbances close to the wall. Tumin & Aizatulin (1997) numerically investigated the instability and receptivity of a laminar wall jet and concluded that the high-frequency viscous mode can be exited more easily by periodic blowing and suction through the wall than the low-frequency inviscid mode. Cohen *et al.* (1992) found a new family of laminar self-similar solutions describing the mean flow of an incompressible two-dimensional wall jet subjected to steady wall blowing or suction. By applying linear stability theory in the temporal framework for the family of solutions, it was shown that blowing stabilizes the inviscid mode while destabilizing the viscous one. The opposite effect was found when suction is applied. These self-similar profiles were later confirmed experimentally by Amitay &

Cohen (1993). Amitay & Cohen (1997) investigated the interaction of the two different modes in the wall jet subject to steady wall blowing or suction.

In a low disturbance environment, the initial stage of the transition process is indeed defined by two-dimensional eigenmodes growing in the outer layer. Two-dimensional direct numerical simulations (DNS) have been successfully employed and the transitional process has been studied e.g. by Gogineni *et al.* (1999) and Seidel & Fasel (2001) for forced laminar wall jets. The simulations demonstrate good agreement with the supporting experiments, at least for the initial stages of transition, where the three-dimensional activity was relatively weak. Seidel & Fasel (2001) adopted a two-dimensional DNS-solver to analyze the effect of periodical forcing by a blowing and suction slot on a laminar wall jet over a heated flat plate. For very low disturbance amplitudes, the simulations show a good agreement with linear stability theory. For an increased amplitude, a strong nonlinear distortion of the mean flow was observed. In particular, the skin friction is reduced markedly, the local maximum velocity is decreased and the wall heat transfer is increased. It was shown that the large structures, generated by the forcing, are the main cause for the strong mean flow distortion of both velocity and temperature. The wall heat transfer was found to increase as large structures entrain cold fluid from the ambient fluid and hot fluid is convected away from the wall.

1.3. *Three-dimensional behavior*

Gogineni *et al.* (1993) and Gogineni & Shih (1997) investigated a laminar wall jet undergoing transition using particle image velocimetry (PIV). Their results show that the transition process is dominated by formation and development of discrete vortices in both the inner and outer regions and the interaction between them. Three-dimensionality initiated in the outer region spreads to the inner region and the emergence of large three-dimensional structures inside the shear layer triggers the complete breakdown of the flow. The importance of the three-dimensional effects on the transition process has also been numerically demonstrated. Wernz & Fasel (1996, 1997) studied the transition process of the wall jet numerically for both two-dimensional and three-dimensional disturbances and found that when forcing of high amplitude disturbances are introduced, mushroom shaped structures are ejected into the ambient fluid. Visbal *et al.* (1998) investigated the breakdown process in a finite aspect ratio wall jet by means of DNS and high-resolution experimental measurements. In the simulation, the experimental base flow were matched to a parabolic profile at the nozzle outlet. In the spanwise direction, an incoming sidewall boundary layer was simulated using a hyperbolic tangent distribution. Two-dimensional forcing was applied by varying the whole base-flow amplitude. They observed a rapid spanwise breakdown of the two-dimensional rollers into streamwise vortices and streaks that start near the sidewalls and propagate toward the midspan of the wall jet.

The primary instability in inflectional base flows such as free shear layers and wall jets is a strong inviscid exponential instability resulting in the roll-up of waves into strong spanwise vortices. These two-dimensional vortices can experience two different types of secondary instability. For low initial three-dimensional excitation, the secondary instability is subharmonic and associated with vortex pairing, like that observed by Bajura & Catalano (1975). If the initial three-dimensional excitation is large enough, a three-dimensional secondary instability is predominant, which suppress the vortex pairing.

It is well-known that in a free shear layer, the development of two-dimensional motion is coupled with secondary streamwise coherent structures, see Ho & Huerre (1984), Bernal & Roshko (1986) and Lasheras *et al.* (1986). The three-dimensional instabilities manifest themselves mainly as counter-rotating streamwise vortices and are formed in the braids between the coherent two-dimensional modes. Numerical studies support these results, see Metcalfe *et al.* (1987) and Balaras *et al.* (2001). The location of the formation of the three-dimensionalities is strongly dependent on the location of the origin and the magnitude of the upstream three-dimensional perturbations. In fact, the observed three-dimensional small scales may destroy the two-dimensional large-scale structures for the case of a high level of random initial disturbances, as it is clearly shown by Balaras *et al.* (2001).

1.4. *Outline of the paper*

The wall jet constitutes an excellent flow case for studying how a free shear layer and a wall bounded flow interacts through a detailed investigation of the interplay between two and three-dimensional structures in the flow breakdown to turbulence. For stability investigations of a high-Reynolds-number wall jet, a description of the laminar base flow is needed, and here this flow is analyzed using the boundary layer equations. For the case of a non-interacting boundary layer and top shear layer, a simple solution exists that consists of a coupling of the Blasius boundary layer and the Blasius shear layer. Hereinafter, a wall jet of this type and its downstream development is referred to as a *Blasius wall jet*.

In the current work, the Blasius wall jet is studied. Linear stability analysis is used and in particular, emphasis is given to the mechanism of non-modal algebraic growth, which leads to the formation of three-dimensional streaks. Furthermore, three-dimensional DNS are carried out and the flow is experimentally visualized. In § 2 of the paper, the equipment and methodology of the experiment is described. In § 3, the numerical techniques used are presented and in § 4, the results obtained are presented. First, the measured base flow is matched to the boundary layer solution. Results of the linear stability theory for both eigenmodes and non-modal streaks are demonstrated and compared with the experiment. Finally, the nonlinear breakdown process is highlighted by the experiment and DNS.

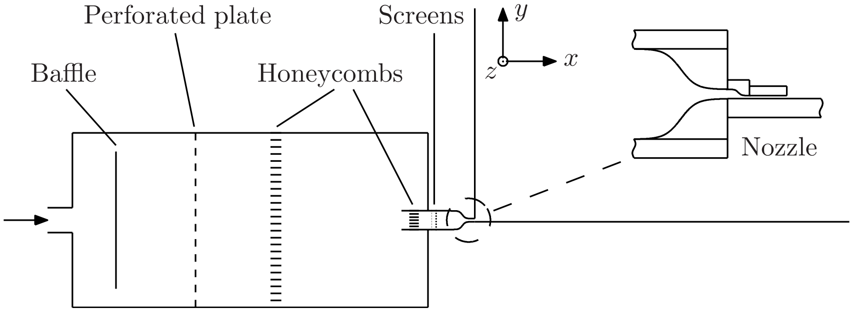

FIGURE 1. Wall-jet facility.

2. Experimental methods

2.1. *Experimental setup*

All experiments were conducted at Chalmers University of Technology in a wall-jet facility, which is schematically shown in figure 1. The wall jet is formed by the injection of air out of a slot and develops over a large horizontal flat plate of 2.1 m in length and 3.2 m in width. This plate is made of wood and coated with a thin plastic laminate. The height of the slot used is 3 mm and the width is 500 mm. A coordinate system is defined in figure 1 with the x-axis streamwise, y-axis normal to the wall and the z-axis in the spanwise direction. Equipped with a vertical back wall of 1.2 m height, located just above the inlet and sidewalls of the same height, the current wall jet can be considered to operate in quiescent surroundings, since the facility is located in a large hall ($15 \times 15 \times 8\,\text{m}^3$) with negligible room draught.

Air is supplied by a centrifugal fan to the settling chamber, which is equipped with flow straightening devices; namely, a baffle, perforated plate, honeycombs and screens. After the settling chamber, the flow enters two smooth contractions of total ratio 36:1. The measured turbulence level of the outlet flow is sufficiently low, less than 0.05% in the frequency range from 10 Hz to 10 kHz. During the measurements, the velocity in the middle of the nozzle, U_0, is checked by a Pitot–Prandtl tube. The manometer used, FSO510, is also equipped with sensors for temperature and absolute pressure readings.

The streamwise velocity component of the wall-jet flow field is measured by a hot wire, which is monitored by a DANTEC constant temperature anemometer. A tungsten single-wire boundary layer probe with a wire diameter and length of 5 μm and 0.7 mm, respectively, was operated at an overheat ratio of 1.8. The hot wire was calibrated in the jet outlet versus the Prandtl tube. Details on the experimental procedure as well as on the measurement equipment used can be found in Chernoray & Löfdahl (2003). Typically the calibration resulted in an error less than 0.5% for all points in the calibration range. The hot wire position traversing mechanism is computer controlled and can be completely automated for long experimental runs through the definition of a geometrical mesh of measurement points. Equipped with servo-motors it can sustain an absolute coordinate system with an accuracy of 10 μm in x and z, and 5 μm in y directions. The acquisition system is the IOTech Wavebook 516 sampling module with expansion unit, enabling 16-bit, 1 MHz sample and hold with full analogue and digital triggering options. The software used to control the sampling and saving of data files is linked into a program for automated, triggered flow measurements using the traverse system and a pre-defined mesh of sampling points. The distance between the hot wire and the wall was measured using an "electro-optical" method and was checked before every experimental run. To employ this method, a strip of electrically conductive foil was glued on the surface and when one probe prong touched the surface an electric circuit was closed. The distance between the wire and the wall when the prong touches the surface was measured optically in this position. It should be pointed out that the wall-distance measurements were performed before the hot wire calibration.

2.2. *Artificial disturbances*

To use the advantages of a controlled experiment and to study the development of two-dimensional waves and stationary longitudinal streaks in detail, disturbances were introduced in the flow artificially.

Time-periodic two-dimensional waves were excited by a loudspeaker situated about two meters downstream of the nozzle outlet. The signal for the loudspeaker of controlled frequency and amplitude was generated by an analogue output board in a computer and an external amplifier unit. The frequency of the artificial disturbances was chosen to be 1221 Hz, which is close to the natural flow frequency and detuned off 50 Hz of the power network. The measurement of the linear instability waves was performed in a region starting at about one hydrodynamic wavelength downstream of the nozzle outlet and prior to the downstream distance where significant nonlinear interactions occurred. Such recommendations can be found in the work by Ho & Huerre (1984) for shear layers and are based mostly on the fact that instability waves are influenced by the solid edge in a near-field region. Also in this work, it is recommended to have an acoustic wavelength large enough for the assurance of the wave two-dimensionality, and this length is about 0.3 m for the mentioned frequency of 1221 Hz. Before the experiment, the two-dimensionality of the base flow and that of the excited waves was carefully checked through measurements and visualizations. To obtain the amplitude and phase information of the signal, fast Fourier transform (FFT) was applied to the velocity time traces, see Chernoray & Löfdahl (2003) for details.

Stationary longitudinal streaks are introduced in the flow by fine roughness elements of controlled geometry and a typical height of 40 μm. The roughness elements are positioned at the orifice of the wall jet onto the inner surface of the top lip of the nozzle. To introduce a streaky pattern of a single spanwise scale,

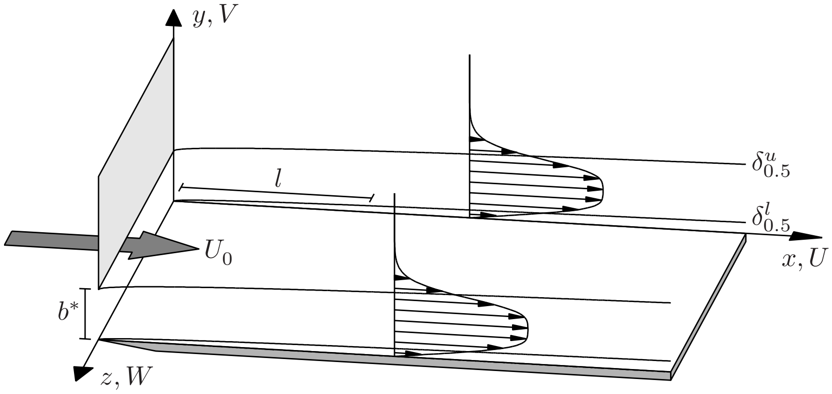

FIGURE 2. Plane wall-jet flow.

typically an array of five uniformly distributed roughness elements is used. It was decided to introduce five different streak scales, and accordingly five groups of humps were positioned on the nozzle. As a result, nearly sinusoidal mean flow modulation was obtained after a short distance downstream of the nozzle outlet. The evaluation of the streaks was performed by measurements of (y, z)-velocity planes of two or three spanwise wavelengths. A cross-sectional plane for each scale was taken with constant steps in the y direction of 0.15 mm and 0.5 mm in the z direction, and the corresponding number of points for each plane was 20 in the wall-normal extent and from 12 to 30 in the spanwise extent, depending on the spanwise streak scale. Subsequently, the undisturbed base flow was subtracted and the remaining stationary disturbance was decomposed into spanwise modes using FFT.

During the measurements, the output signal from the anemometer was amplified and digitized; post processing was done using the software package Matlab.

3. Numerical solution methods

3.1. *Scaling*

Consider an incompressible wall jet over a flat plate as illustrated in figure 2. Fluid with exit velocity U_0 is, through a slot with height b^*, blown tangentially along a wall. The scalings are originating from the boundary-layer approximations. The streamwise coordinate x is scaled with the length scale l, which is a fixed distance from the slot. The wall-normal and spanwise coordinates y and z, respectively, are scaled with the boundary-layer parameter $\delta = \sqrt{\nu l/U_0}$, where ν is the kinematic viscosity of the fluid. The streamwise velocity U is scaled with U_0, while the wall-normal and spanwise velocities V and W, respectively, are scaled with $U_0\delta/l$. The pressure P is scaled with $\rho U_0^2\delta^2/l^2$, where ρ is the density of the fluid, and the time t is scaled with l/U_0. The Reynolds numbers used here are defined as $Re_l = U_0 l/\nu$ and $Re_\delta = U_0\delta/\nu$. It is useful to note the relations $l/\delta = Re_\delta = \sqrt{Re_l}$.

3.2. *Linear disturbance equations*

The well-known parabolized-stability-equations (PSE) technique (Bertolotti *et al.* 1992; Herbert 1997) deals with the spatial evolution of exponentially growing eigenmodes. Those equations are scaled with a suitable scaling for modal waves, e.g. the streamwise and normal disturbance velocities are assumed to be of the same order. However, in the last decade there has been an increasing interest in the algebraically growing non-modal Klebanoff modes (Klebanoff 1971; Westin *et al.* 1994; Andersson *et al.* 1999). The two growth scenarios are associated with different scales. The governing equations for non-modal disturbances are scaled with the boundary-layer scaling, see Andersson *et al.* (1999). Here we summarize a set of stability equations valid for both algebraically and exponentially growing disturbances, given by Levin & Henningson (2003). For further details, the reader is referred to that investigation.

We want to study the linear stability of a high-Reynolds-number flow. The non-dimensional Navier–Stokes equations for an incompressible flow are linearized around a two-dimensional, steady base flow $\big(U(x,y),\ V(x,y),\ 0\big)$ to obtain the stability equations for the spatial evolution of three-dimensional, time-dependent disturbances $\big(u(x,y,z,t), v(x,y,z,t), w(x,y,z,t), p(x,y,z,t)\big)$. The disturbances, that are scaled as the base flow, are taken to be periodic in the spanwise direction and time, which allow us to assume solutions of the form

$$f = \hat{f}(x,y)\exp\left(\mathrm{i}Re_\delta\int_{x_0}^{x}\alpha(x)\,dx + \mathrm{i}\beta z - \mathrm{i}\omega t\right), \tag{1}$$

where f represents either one of the disturbances u, v, w or p. The complex streamwise wave number α captures the fast wave-like variation of the modes and is therefore scaled with $1/\delta$ and α itself is assumed to vary slowly with x. The x-dependence in the amplitude function $\hat{f}$ includes the weak variation of the disturbances. The real spanwise wave number β and the real disturbance angular frequency ω are scaled in a consistent way with z and t, respectively. Introducing (1) in the linearized Navier–Stokes equations and neglecting third order terms in $1/Re_\delta$ or higher, we arrive at the parabolized stability equations in boundary-layer scalings

$$\hat{u}_x + \mathrm{i}Re_\delta\alpha\hat{u} + \hat{v}_y + \mathrm{i}\beta\hat{w} = 0, \tag{2}$$

$$(U_x + \mathrm{i}Re_\delta\alpha U - \mathrm{i}\omega)\hat{u} + U\hat{u}_x + V\hat{u}_y + U_y\hat{v} + \frac{\hat{p}_x}{Re_\delta^2} + \frac{\mathrm{i}\alpha\hat{p}}{Re_\delta} = \hat{u}_{yy} - k^2\hat{u}, \tag{3}$$

$$(V_y + \mathrm{i}Re_\delta\alpha U - \mathrm{i}\omega)\hat{v} + U\hat{v}_x + V_x\hat{u} + V\hat{v}_y + \hat{p}_y = \hat{v}_{yy} - k^2\hat{v}, \tag{4}$$

$$(\mathrm{i}Re_\delta\alpha U - \mathrm{i}\omega)\hat{w} + U\hat{w}_x + V\hat{w}_y + \mathrm{i}\beta\hat{p} = \hat{w}_{yy} - k^2\hat{w}, \tag{5}$$

where $k^2 = \alpha^2 + \beta^2$. All the terms are generally of the first or the second order except the $\hat{p}_x/Re_\delta^2$ term, in (3), which is of the third order for the algebraic instability problem and the $V_x\hat{u}$ term, in (4), which is of the third order for the exponential instability problem. Both of those terms, however, have to be included in a general formulation of the problem. Unfortunately, the $\hat{p}_x/Re_\delta^2$ term introduces numerical instability, setting a lower limit of the streamwise step size, as is the case for all PSE formulations.

We are interested of solutions subject to no-slip conditions at the plate and vanishing at the wall-normal position $y_{\max}$ well outside the wall jet. The boundary conditions in the wall-normal direction can then be written

$$\begin{cases} \hat{u} = \hat{v} = \hat{w} = 0 \quad \text{at} \quad y = 0, \\ \hat{u} = \hat{v} = \hat{w} = 0 \quad \text{at} \quad y = y_{\max}. \end{cases} \tag{6}$$

The set of equations is nearly parabolic in the streamwise coordinate and are marched forward from an initial position x_0 to a final position x_1. Given the initial conditions

$$\hat{u} = \hat{u}_0(y), \quad \hat{v} = \hat{v}_0(y), \quad \hat{w} = \hat{w}_0(y) \quad \text{at} \quad x = x_0, \tag{7}$$

the wave number β and the angular frequency ω, the initial-boundary-value problem is solved from x_0 to x_1 to obtain the downstream development of the disturbance.

The disturbance growth is generally measured by the average change in the kinetic energy of the fluid. In spatially evolving investigations, a commonly used quantity to represent this change is the disturbance energy defined as

$$E(x, \beta, \omega, Re_l) = \int_0^{y_{\max}} (Re_l|u|^2 + |v|^2 + |w|^2)dy = \hat{E}e^{\theta}, \tag{8}$$

where

$$\hat{E} = \int_0^{y_{\max}} (Re_l|\hat{u}|^2 + |\hat{v}|^2 + |\hat{w}|^2)dy, \quad \theta = -2Re_\delta \int_{x_0}^{x} \alpha_{\mathrm{i}} dx. \tag{9}$$

3.2.1. *Exponential growth*

Here we consider solutions to (2–7) associated with wave-like disturbances, i.e. where α in the phase function in (9) is order unity. As both the amplitude and phase function depend on x, one more equation is required. We require that both the amplitude function and the wave number α change slowly in the streamwise direction, and specify a normalization condition on the amplitude function

$$\int_0^{y_{\max}} (Re_l\overline{\hat{u}}\hat{u}_x + \overline{\hat{v}}\hat{v}_x + \overline{\hat{w}}\hat{w}_x)dy = 0, \tag{10}$$

where the bar denotes complex conjugate. Other conditions are possible and are presented in the paper by Bertolotti *et al.* (1992). The normalization condition specifies how much growth and sinusoidal variation are represented by the amplitude and phase function, respectively. The stability problem (2–7) and (10) have to be solved iteratively in each streamwise step. The numerical method solving the stability equations is based on a spectral collocation method involving Chebyshev polynomials. Details about the numerical scheme can be found in the papers of Andersson *et al.* (1999) and Hanifi *et al.* (1996). The initial condition (7) is taken as the least stable eigenfunction of Orr–Sommerfeld and Squire equations with corresponding eigenvalue $\alpha(x_0)$. Since the initial condition do not capture non-parallel effects there will be a region in the beginning of the domain that includes some errors. The size of those errors and the length of that region is dependent of how non-parallel the base flow is.

3.2.2. *Optimal disturbances*

Now we consider solutions to (2–7) with $\alpha = 0$, giving rise to disturbances with weak streamwise variations. We are interested of maximizing the disturbance energy (8), in the downstream position x_1 by optimizing the initial disturbance at x_0 with given initial energy. That is, we want to maximize the disturbance growth defined by

$$G(x_0, x_1, \beta, \omega, Re_l) = \frac{E(x_1)}{E(x_0)}. \tag{11}$$

When going to the limit of large Reynolds number, the maximum growth will, because of the difference in order between the terms in the disturbance energy (8), be obtained for initial disturbances with a zero streamwise velocity component. Furthermore, provided that $\hat{u}_1$ is non-zero, $\hat{v}_1$ and $\hat{w}_1$ can be neglected and the Reynolds-number-independent growth can be simplified to

$$\overline{G} = \lim_{Re_l \to \infty} \frac{G}{Re_l} = \frac{\displaystyle\int_0^{y_{\max}} |\hat{u}_1|^2 dy}{\displaystyle\int_0^{y_{\max}} (|\hat{v}_0|^2 + |\hat{w}_0|^2) dy} = \frac{(\hat{u}_1, \hat{u}_1)_u}{(\boldsymbol{q}, \boldsymbol{q})_q}. \tag{12}$$

The last identity defines the appropriate inner products, where $\boldsymbol{q} = (\hat{v}_0, \hat{w}_0)^T$. The optimization problem in the large-Reynolds-number limit is defined by maximizing (12) and concerns the optimization of the initial disturbance $\boldsymbol{q}$ for given values of x_0, x_1, β and ω. Details about the derivation of the optimization procedure can be found in the appendix and in Levin & Henningson (2003) and details about the numerical scheme can be found in the papers of Andersson *et al.* (1999) and Hanifi *et al.* (1996). The numerical method solving the forward problem (2–7) and the backward problem (33–38) is based on a spectral collocation method involving Chebyshev polynomials.

3.3. *DNS techniques*

3.3.1. *Numerical methods*

The numerical code (see Lundbladh *et al.* 1999) uses spectral methods to solve the three-dimensional, time-dependent, incompressible Navier–Stokes equations. The discretization in the streamwise and spanwise directions make use of Fourier series expansions, which enforces periodic solutions. The discretization in the normal direction is represented with Chebyshev polynomial series.

A pseudo-spectral treatment of the nonlinear terms is used. The time advancement used is a second-order Crank–Nicolson method for the linear terms and a four-step low-storage third-order Runge–Kutta method for the nonlinear terms. Aliasing errors arising from the evaluation of the pseudo-spectrally convective terms are removed by dealiasing by padding and truncation using the 3/2-rule when the FFTs are calculated in the wall-parallel planes. In the normal direction, it has been found that increasing the resolution is more efficient than the use of dealiasing.

Flows such as boundary layers and wall jets are spatially growing and to fulfill the necessary periodic boundary condition in the streamwise direction, required by the spectral discretization, a fringe region (see Nordström *et al.* 1999) is added in the downstream end of the computational domain. In this region, the function $\lambda(x)$ is smoothly raised from zero and the flow is forced to a desired solution $\boldsymbol{v}$ in the following manner:

$$\frac{\partial \boldsymbol{u}}{\partial t} = NS(\boldsymbol{u}) + \lambda(x)(\boldsymbol{v} - \boldsymbol{u}) + \boldsymbol{g}, \tag{13}$$

$$\nabla \cdot \boldsymbol{u} = 0, \tag{14}$$

where $\boldsymbol{u}$ is the solution vector and $NS(\boldsymbol{u})$ the right-hand side of the (unforced) momentum equations. Both $\boldsymbol{g}$, which is a disturbance forcing, and $\boldsymbol{v}$ may depend on the three spatial coordinates and time. The forcing vector $\boldsymbol{v}$ is smoothly changed (blended) from the undisturbed wall-jet solution of the boundary layer equations at the beginning of the fringe region to the prescribed inflow velocity vector, which is the Blasius wall jet shown in figure 3(a). In the case of forcing a disturbance in the flow, it is also added to the forcing vector in the end of the fringe region. The fringe function is conveniently written as

$$\lambda(x) = \lambda_{\max}\left[S\left(\frac{x - x_{\text{start}}}{\Delta_{\text{rise}}}\right) - S\left(\frac{x - x_{\text{end}}}{\Delta_{\text{fall}}} + 1\right)\right], \tag{15}$$

where $\lambda_{\max}$ is the maximum strength of the damping, x_{start} and x_{end} are the start and end of the fringe region, respectively, and Δ_{rise} and Δ_{fall} are the rise and fall distance of the damping function. $S(\xi)$ is a smooth step function with continuous derivatives of all orders defined by

$$S(\xi) = \begin{cases} 0, & \xi \leqslant 0 \\ 1/\left[1 + \exp\left(\dfrac{1}{\xi - 1} + \dfrac{1}{\xi}\right)\right], & 0 < \xi < 1 \\ 1, & \xi \geqslant 1. \end{cases} \tag{16}$$

This method damps disturbances flowing out of the physical region and smoothly transforms the flow to the desired inflow state, with a minimal upstream influence.

At the wall, no-slip boundary condition is set and at the free-stream position $y_{\max}$, generalized boundary condition is applied in Fourier space with different coefficients for each wavenumber. It is non-local in physical space and takes the following form:

$$\frac{\partial \hat{\boldsymbol{u}}}{\partial y} + k\hat{\boldsymbol{u}} = \frac{\partial \hat{\boldsymbol{v}}_0}{\partial y} + k\hat{\boldsymbol{v}}_0, \tag{17}$$

where $\hat{\boldsymbol{u}}$ is the Fourier transform of $\boldsymbol{u}$. Here $\boldsymbol{v}_0$ denotes the blended wall-jet solution of the boundary layer equations taken as the initial condition and $\hat{\boldsymbol{v}}_0$ its Fourier transform. In the spanwise direction, periodic boundary condition is set.

3.3.2. *Disturbance generation and numerical parameters*

The present numerical implementation provides several possibilities for disturbance generation. Disturbances can be included in the desired solution $\boldsymbol{v}$, thereby forcing them in the fringe region, by a body force $\boldsymbol{g}$ and by blowing and suction at the wall through non-homogeneous boundary conditions. For the wall jet, we make use of a body force trip strip to introduce random motions and forcing of controlled streaks and waves in the fringe region. The trip can be used to generate turbulence or at lower amplitude levels to introduce three-dimensionality. Random noise is introduced in the flow by a body force, which is directed normal to the wall, see Lundbladh *et al.* (1999).

To study the instability and interaction of time-periodic two-dimensional waves $\boldsymbol{v}_w$ and stationary longitudinal streaks $\boldsymbol{v}_s$, the velocity fields are added to the blended Blasius wall-jet solution $\boldsymbol{v}_0$ to give a forcing vector of the form $\boldsymbol{v} = \boldsymbol{v}_0 + \boldsymbol{v}_w + \boldsymbol{v}_s$. The two-dimensional waves $\boldsymbol{v}_w = (u, v, 0)$ are taken from solutions of the parabolized stability equations (2–5) with $\beta = 0$. The vector, which can be derived from (1) takes the form

$$\boldsymbol{v}_w = \boldsymbol{f}_c \cos\omega t + \boldsymbol{f}_s \sin\omega t, \tag{18}$$

where

$$\boldsymbol{f}_c = (\hat{\boldsymbol{f}}_{\mathrm{r}} \cos a_{\mathrm{r}} - \hat{\boldsymbol{f}}_{\mathrm{i}} \sin a_{\mathrm{r}})e^{-a_{\mathrm{i}}}, \quad \boldsymbol{f}_s = (\hat{\boldsymbol{f}}_{\mathrm{r}} \sin a_{\mathrm{r}} + \hat{\boldsymbol{f}}_{\mathrm{i}} \cos a_{\mathrm{r}})e^{-a_{\mathrm{i}}} \tag{19}$$

and

$$a_{\mathrm{r}} = \int_{x_0}^{x} \alpha_{\mathrm{r}} dx, \quad a_{\mathrm{i}} = \int_{x_0}^{x} \alpha_{\mathrm{i}} dx, \tag{20}$$

where the subscripts $_{\mathrm{r}}$ and $_{\mathrm{i}}$ denote real and imaginary part, respectively. The spanwise periodic streaks are taken from optimized solutions of the stability equations (2–5) with $\omega = 0$ and $\alpha = 0$. The forcing vector takes the form

$$\boldsymbol{v}_s = (\hat{u}_{\mathrm{r}} \cos\beta z,\ \hat{v}_{\mathrm{r}} \cos\beta z,\ -\hat{w}_{\mathrm{i}} \sin\beta z). \tag{21}$$

The size of the computational box used for the simulation presented in this paper was $(xl \times yl \times zl) = (3.09 \times 206 \times 29.8)$. The width of the box was set to fit one spanwise wavelength of the forced streaks. The Reynolds number at the initial location of the box at $x = 1$ was $Re_\delta = 173$. The resolution was $(nx \times ny \times nz) = (540 \times 541 \times 64)$. Dealiasing was activated in the streamwise and spanwise directions. The parameters for the fringe region were $x_{\mathrm{start}} = 3.49$, $x_{\mathrm{end}} = 4.09$, $\Delta_{\mathrm{rise}} = 0.199$, $\Delta_{\mathrm{fall}} = 0.0996$ and $\lambda_{\max} = 1.0$.

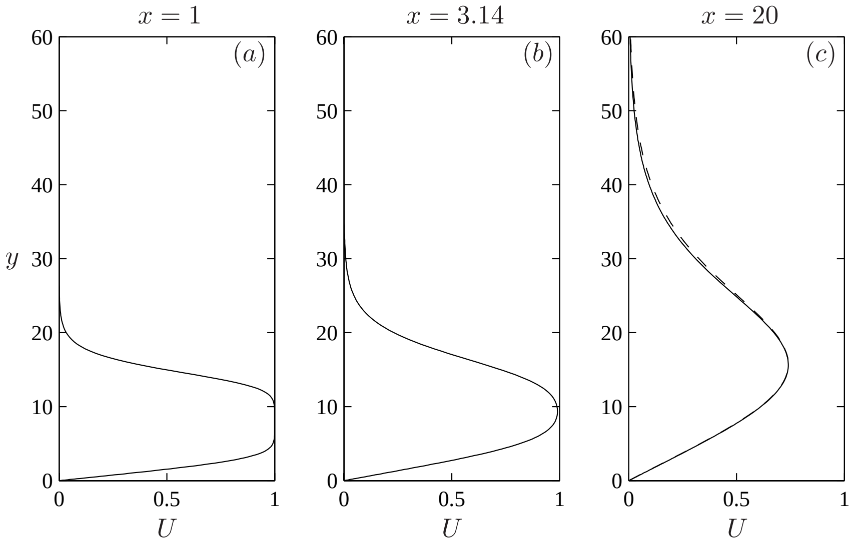

FIGURE 3. Streamwise development of the Blasius wall jet calculated with the boundary layer equations. Far downstream, the solution approaches a Glauert similarity solution evolving from a different virtual origin. The Glauert solution (− − −) is shown for comparison in (*c*).

The random noise was forced to introduce three-dimensionality to the initial field. However, the trip was turned off well before the forced waves and streaks were studied. The waves and streaks were forced in the fringe region in a similar manner as by Brandt & Henningson (2002), who made use of the same spectral code to study the transition of streamwise streaks in Blasius boundary layer. The forcing was turned on smoothly in both space and time. The amplitudes of the waves and streaks were prescribed at the end of the fringe region to 0.001 and 0.03, respectively.

4. Results

4.1. *Matching the base flow*

Most of the numerical studies of the wall jet have concerned the similarity solution of Glauert (1956), which is an asymptotic solution. A consideration of the near field of the wall jet in our investigation shows that the flow has not achieved the self-similar Glauert profile. The Glauert wall jet only exists for small Reynolds numbers or far downstream of the slot where a real flow can not be treated as laminar. To investigate the flow close to the slot at a rather high Reynolds number, it is necessary to find another base flow more suitable to match with the experiment.

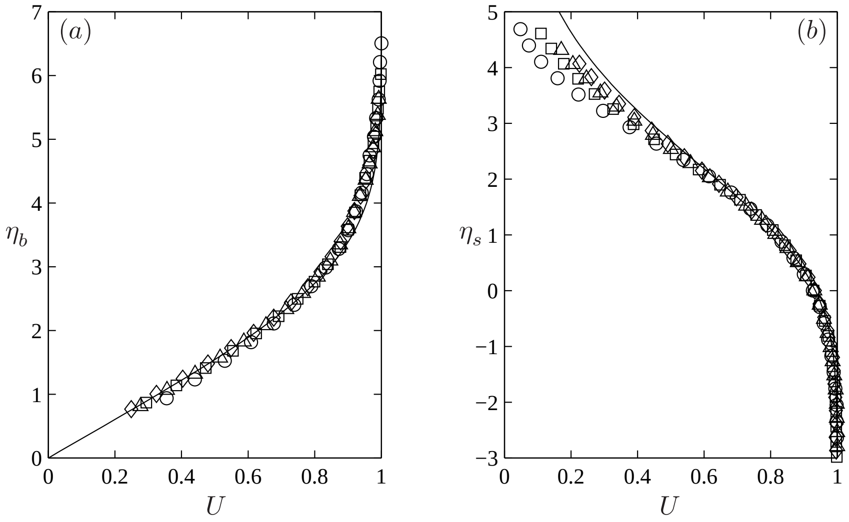

FIGURE 4. Comparison of the computed base flow (—) for $Re_\delta = 173$ with experimental results at 1 mm (○), 6 mm (□), 11 mm (△) and 16 mm (◊) downstream of the nozzle outlet. The experimental data are scaled with the local boundary layer parameter δ and local maximum velocity U_m and fitted to the computed similarity solutions with $l = 29$ mm and $b^* = 2.06$ mm. (*a*) Boundary layer region. (*b*) Shear layer region.

Consider a top-hat profile through a slot with height b located at $x = 0$, see figure 2. Immediate downstream of the slot, a boundary layer will develop at the wall and a shear layer will develop in the upper part of the top-hat profile, independently of each other. Further downstream, the boundary layer and the shear layer will begin to interact and the local maximum velocity will slow down. Our solution consists of a coupling of Blasius boundary layer and shear layer as an initial condition to the boundary layer equations. The two solutions, which both are similarity solutions to the Blasius equation with different boundary conditions, are discussed in the book of Schlichting (1979). In the boundary-layer scalings, Blasius similarity equation reads

$$2f''' + ff'' = 0, \tag{22}$$

where $f(\eta)$ is the non-dimensional stream function and the prime denotes derivatives with respect to the similarity variable η. The base flow can then be written

$$U = f', \quad V = \frac{1}{2}\big(\eta f' - f\big). \tag{23}$$

For the boundary layer, the similarity variable η_b relates to the non-dimensional coordinates as $y = \sqrt{x}\eta_b$ and the boundary conditions read

$$\eta_b = 0 : \quad f = 0, \quad f' = 0; \qquad \eta_b \to +\infty : \quad f' = 1. \tag{24}$$

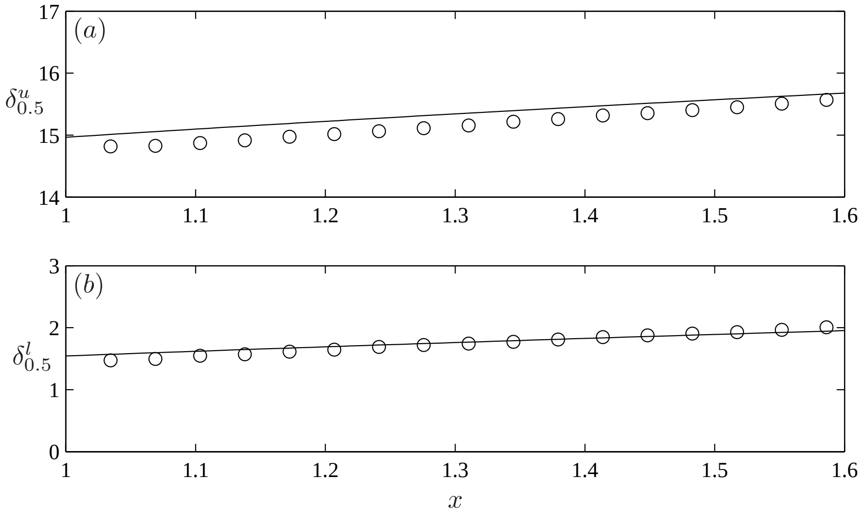

FIGURE 5. Comparison of the computed base flow (—) for $Re_\delta = 173$ with experimental results (○). The graphs show the upper, (*a*), and lower, (*b*), jet half-widths $\delta^u_{0.5}$ and $\delta^l_{0.5}$, respectively.

The shear layer has the displaced similarity variable $\eta_s = \eta_b - b$ and is subject to the boundary conditions

$$\eta_s \to -\infty: \quad f = \eta_s - 2V_b, \quad f' = 1; \qquad \eta_s \to +\infty: \quad f' = 0, \tag{25}$$

where V_b is the free-stream normal velocity taken from the boundary layer similarity solution, to fulfill continuity in the normal velocity throughout the wall jet. The two similarity solutions are connected to each other at the location $x = 1$ and form the boundary layer and shear layer regions in the Blasius wall jet. The downstream development is computed with the boundary layer equations. Figure 3 shows the Blasius wall jet and its streamwise development calculated with the boundary layer equations. The location in figure 3(*a*) corresponds to the initial condition at $x = 1$. Figure 3(*b*) shows the location $x = 3.14$, where the interaction of the boundary layer and the shear layer has just began and the maximum velocity is $U_m = 0.99U_0$. Far downstream at the location $x = 20$ in figure 3(*c*), the flow approaches the Glauert solution (Glauert 1956) shown as the dashed line.

In the experiment, thin boundary layers are formed already in the nozzle. Therefore, the virtual slot is placed a distance l upstream of the nozzle outlet with a virtual slot height b^*, different from the experimental nozzle opening height. In order to match the theoretical base flow to the experiment, l, which is taken as the streamwise scale, and b^* have to be chosen. To do so, the boundary layer and shear layer regions of the measured wall jet are scaled with local scalings and compared to the Blasius boundary and shear layer

x:	1.0	1.03	1.21	1.38	1.55	3.14	20.0
$x^* - l$:	0 mm	1 mm	6 mm	11 mm	16 mm	62 mm	551 mm

Table 1. Streamwise locations with the corresponding dimensional distances downstream of the experimental nozzle outlet.

similarity solutions, see figure 4. The experimental data are taken from 1 mm, 6 mm, 11 mm and 16 mm downstream of the nozzle outlet. The streamwise locations and their corresponding dimensional distances downstream of the experimental nozzle outlet used for the measurements are summarized in table 1. The maximum outlet velocity is $U_0 = 15.4\,\mathrm{m\ s}^{-1}$, corresponding to the Reynolds number $Re_\delta = 173$. The best matching is achieved for $l = 29\,\mathrm{mm}$ and $b^* = 2.06\,\mathrm{mm}$ corresponding to the non-dimensional virtual slot height $b = 12.3$. The normal scale is $\delta = \sqrt{\nu l/U_0} = 0.168\,\mathrm{mm}$.

The Blasius wall jet can be made independent of the slot height b, downstream of the point of interaction of the shear layer and the boundary layer, by introducing the coordinates

$$\zeta = \frac{y}{b}, \quad \xi = \frac{x}{b^2}. \tag{26}$$

If we re-scale the downstream distance measured from the experimental nozzle opening with the slot height, locations downstream of the point of interaction may be written

$$\frac{x^* - l}{b^*} = Re_\delta \left(b\xi - \frac{1}{b} \right), \tag{27}$$

where the star denotes dimensional variables. Inserting the value of the slot height used for our Blasius wall jet, the value of the right hand side of equation (27) is $1.55 Re_\delta$ at the location shown in figure 3(*c*). Hence, given the top-hat profile blowing out from a slot, the Glauert wall jet is reachable only many slot height distances downstream of the slot in the case when the flow Reynolds number is high. As the flow Reynolds number decreases, the distance needed to approach this solution also decreases.

It can be seen in figure 4(*b*) that the agreement between the experiment and the theory near the jet core in the shear layer region is excellent. A slight difference in the upper part of the boundary layer region in figure 4(*a*) remains as the flow evolves downstream. The measured flow close to the wall and the upper part of the shear layer region is however, approaching the theoretical solution. There are two reasons for the disagreement in the upper part of the wall jet. First, a jump of the boundary conditions occur on the top lip of the nozzle as the flow leaves and a kink in the experimental velocity data can be observed. With increased downstream distance, the influence of the nozzle disappears and the agreement becomes better. Secondly, a secondary flow is set up in the experiment, which is not taken into account in the computed base flow. Additionally, it can be mentioned that the best matching for the boundary layer

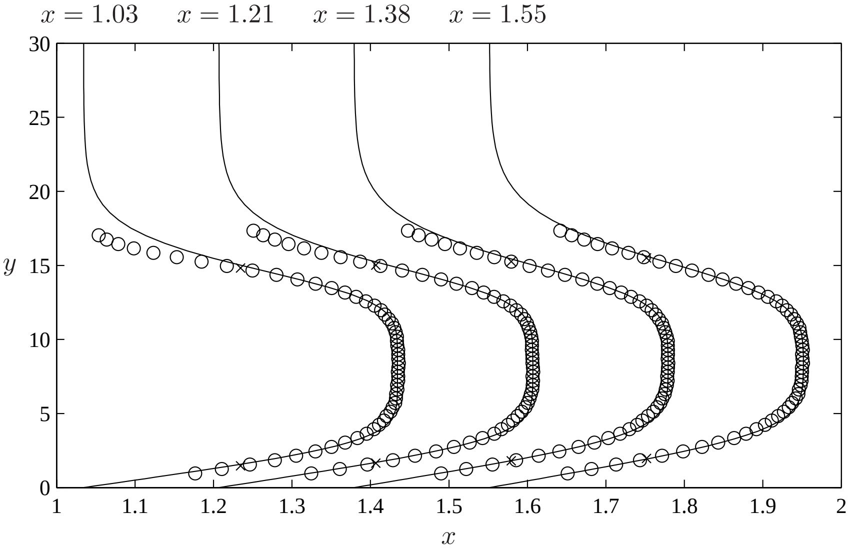

Figure 6. Comparison of the computed base flow (—) for $Re_\delta = 173$ with experimental results (○) at 1 mm, 6 mm, 11 mm and 16 mm downstream of the nozzle outlet (the non-dimensional locations are indicated in the figure). (×): The upper and lower jet half-widths.

region is achieved for a slightly larger virtual distance ($l = 43$ mm) indicating that the lower boundary layer in the nozzle is thicker than the upper, thus experimental symmetry is not perfect. However, a priority is given to match the shear layer region of the wall jet.

Figures 5(*a*) and 5(*b*) show the streamwise development of the upper and lower jet half-widths $\delta^u_{0.5}$ and $\delta^l_{0.5}$, respectively, which are the distances from the wall where the velocity reaches one half of the local maximum velocity. The experimental data are measured with 1 mm steps to 17 mm downstream of the nozzle outlet. The whole scaled flow is shown in figure 6 for four downstream locations $x = 1.03, 1.21, 1.38, 1.55$ and the measured upper and lower jet half-widths are indicated with crosses.

4.2. *Linear stability analysis*

In the following section, the stability of the computed base flow at $Re_\delta = 173$ is investigated by means of the linear parabolized stability equations and the results are compared with the measurements. The instability with respect to two-dimensional eigenmodes and non-modal streaks is investigated.

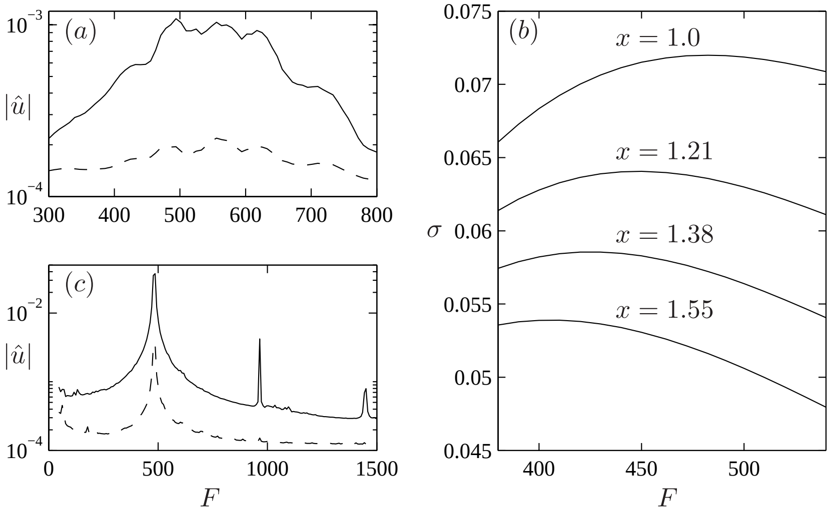

FIGURE 7. Frequency spectra at $x = 1.38$ (– – –) and $x = 1.55$ (—) for natural case (a) and forced by a loudspeaker at 1221 Hz ($F = 482$) with amplitude 4% at $x = 1.55$ (c). (b) Computed growth rates σ for $Re_\delta = 173$ at different streamwise locations corresponding to 0 mm, 6 mm, 11 mm and 16 mm downstream of the nozzle outlet (the non-dimensional locations are indicated in the figure).

4.2.1. *Two-dimensional waves*

The natural spectra of the streamwise velocity component obtained in the position of maximum disturbance in the wall-normal direction is shown, at $x = 1.38$ (– – –) and $x = 1.55$ (—), in figure 7(a). The reduced frequency is defined by $F = 10^6\omega/Re_l$. It is clear that under natural conditions, the wall jet operates in unforced mode and a broad band of frequencies amplifies. The root mean square of the broadband disturbance amplitude at $x = 1.55$ is approximately 0.5% of the jet exit velocity. That allow us to consider the flow to be laminar down to this location under natural conditions. In figure 7(b), the computed physical growth rate defined as

$$\sigma(x) = \frac{1}{Re_\delta}\frac{1}{\sqrt{\hat{E}}}\frac{\partial\sqrt{\hat{E}}}{\partial x} - \alpha_{\rm i}, \tag{28}$$

is shown as predicted by the linear theory. It is clearly visible that in the theory, as well as in the experiment, the most amplified frequency decreases with increased streamwise location. The most amplified frequency of Blasius shear layer predicted by the inviscid stability theory of Monkewitz & Huerre (1982) is about 480, which is very close to the peak observed for the location

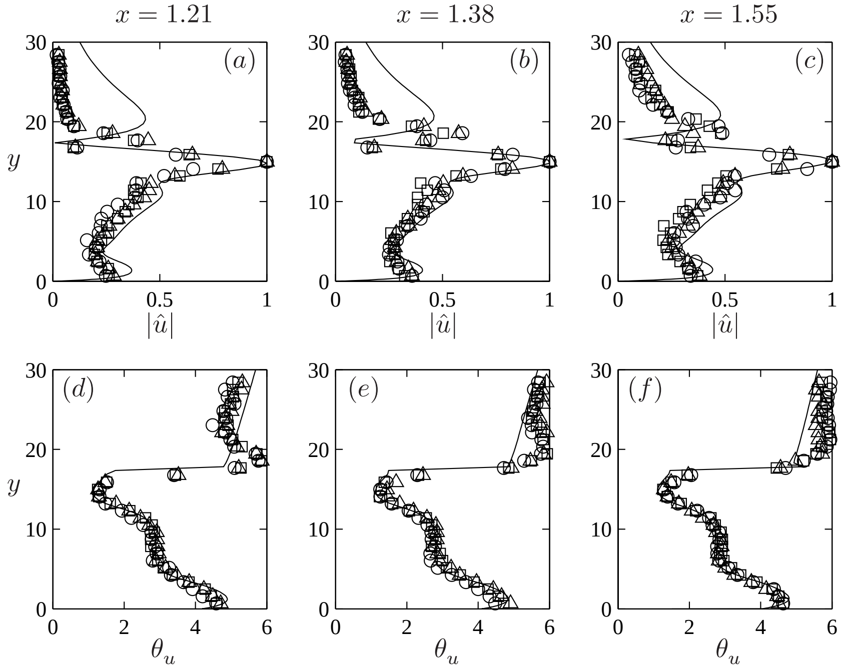

FIGURE 8. Comparison of the computed (—) u-velocity amplitude, normalized with its maximum value, and phase distribution θ_u, for $Re_\delta = 173$ and $F = 482$ with experimental results at $x = 1.21, 1.38, 1.55$. The disturbance are triggered by a loudspeaker at 1221 Hz and have the amplitudes 0.3% (○), 1.1% (□) and 1.7% (△) at $x = 1.55$.

$x = 1$ in figure 7(b). That suggests that the wall jet operates in the shear layer mode.

Subsequently, the flow was artificially forced in the experiment and characteristics of the instability waves under controlled conditions are studied. The frequency of the artificial disturbances was chosen close to the natural dominating flow frequency, which led to the breakdown, namely the selected value was 1221 Hz corresponding to $\omega = 14.4$, or $F = 482$. In figure 7(c), the forced spectra, for a relatively large forcing amplitude (4% at $x = 1.55$) is shown for the same streamwise locations as the natural spectra. At the location $x = 1.55$, nonlinear effects start to be apparent and peaks of higher harmonics of the main frequency can be seen in the spectra. The first superharmonic has about 10% of the main harmonic. The forcing of the flow leads to a strong coherence of the disturbance around the excitation frequency, as also can be seen for free shear layers.

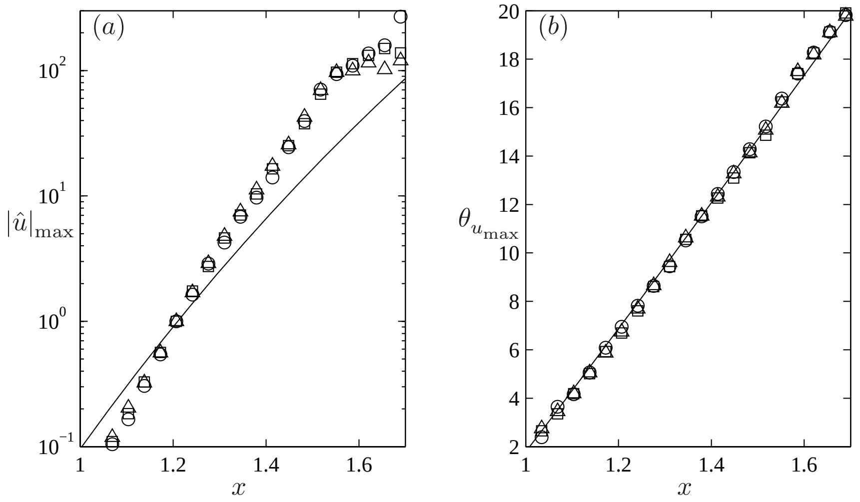

FIGURE 9. Comparison of the computed (—) maximum u-velocity amplitude (a) and phase (b) amplification for $Re_\delta = 173$ and $F = 482$ with experimental results. The disturbance is triggered by a loudspeaker at 1221 Hz and have the amplitudes 0.3% (○), 1.1% (□) and 1.7% (△) at $x = 1.55$.

Figure 8 shows the amplitude and phase distribution at three downstream locations $x = 1.21, 1.38, 1.55$ for the three different forcing amplitudes 0.3% (○), 1.1% (□) and 1.7% (△) compared with the computed results (—). The three experimental amplitude values are measured at the streamwise location $x = 1.55$. It can be noted that the agreement between the experiment and the linear stability computation is very good apart from the upper part of the shear layer region. The deviation there is most likely due to the difference in the base flow and because the waves in the experiment are not fully developed eigenmodes so close to the nozzle outlet. However, the agreement improves downstream. Furthermore, the agreement in the results between the different forcing amplitudes indicates the linearity of the disturbance. The disturbance has a very typical shape and the peak in the shear layer part is in antiphase to the peak near the wall.

The downstream development of the disturbances is demonstrated in figures 9(a) and 9(b), where the maximum u-velocity amplitude and phase, respectively, are shown versus streamwise coordinate. The three cases of forcing are compared with the computation and the same symbols are used as in figure 8. The demonstrated amplitude data are normalized with the amplitude at the location $x = 1.21$, and the disturbance phase θ_u is shown in radians. This figure additionally supports the conclusion made on the linearity of disturbances in the experiment. An indication of the nonlinear effects appear just after the location $x = 1.55$ where it shows up as a lower amplification for the larger forcing amplitudes. The difference of the slopes of the amplitude curves implies that in overall the growth rate in the experiment is about 40% higher. This fact can be expected as the base flow is not precisely the same and the experimental waves differ from the stability eigenmodes. Additional numerical tests have revealed that the latter effect mostly causes the disagreement. For a rapidly changing disturbance, it seems like even a slight deviation of the disturbance from the eigenmode is crucial. At the same time, the phase distribution is predicted very well. The observed average phase velocity of the disturbance coincides very well in the experiment and the linear theory.

4.2.2. *Stationary longitudinal streaks*

The exponentially growing disturbances studied in the previous section are the dominating instabilities of flows having a point of inflection. This is true for the wall jet as well as for free shear layers operated at a low disturbance environment. On the other hand, numerous studies of wall bounded shear flows show that three-dimensional disturbances of a different type may dominate in the breakdown process, especially when the flow is highly disturbed, see e.g. Westin *et al.* (1994). The dominating role of the longitudinal disturbances has been clarified recently by Balaras *et al.* (2001) for highly disturbed free shear layers. As it was mentioned in the introduction, intermediate states when both two- and three-dimensional disturbances exist are also possible for the free shear layers. A similar behavior is expected in the wall jet and the growth of longitudinal streaks is studied.

An idea of how the steady perturbations are selected in the wall-jet flow is directly obtained by considering a plot of the maximized disturbance growth $G_{\max}$ versus wavenumber. In figure 10(*b*), the computed optimal growth for $\omega = 0$, $x_0 = 0.403$ and $x_1 = 1.55$ is shown as a function of spanwise wave number. The most growing spanwise scale is approximately $\beta = 0.29$. In calculations with fix x_1, the optimal spanwise wave number increases slightly with increased x_0. However, for practical reasons, to obtain an initial disturbance in the subsequently described DNS, the initial position was set equal to the starting position of the fringe region.

In the corresponding experiment, stationary longitudinal streaks are introduced in the flow by periodically distributed roughness elements that are positioned onto the top lip of the orifice. In separate runs, five spanwise scales are generated corresponding to β from 0.175 to 0.574 by the roughness elements of corresponding width from 3 to 1 mm. In figure 10(*a*), the spectral decomposition of the maximum streak amplitude for the three largest spanwise scales, $\beta = 0.264$ ($\circ$), $\beta = 0.218$ ($\square$) and $\beta = 0.176$ ($\triangle$), at the streamwise location $x = 1.55$ is shown. The other two smallest scales were decaying in the experiment. One of the introduced scales, $\beta = 0.218$, leads to the largest amplitude disturbance and is optimal in this sense. Streaks of approximately this scale were also visible for roughness-unforced flow in the nonlinear stage

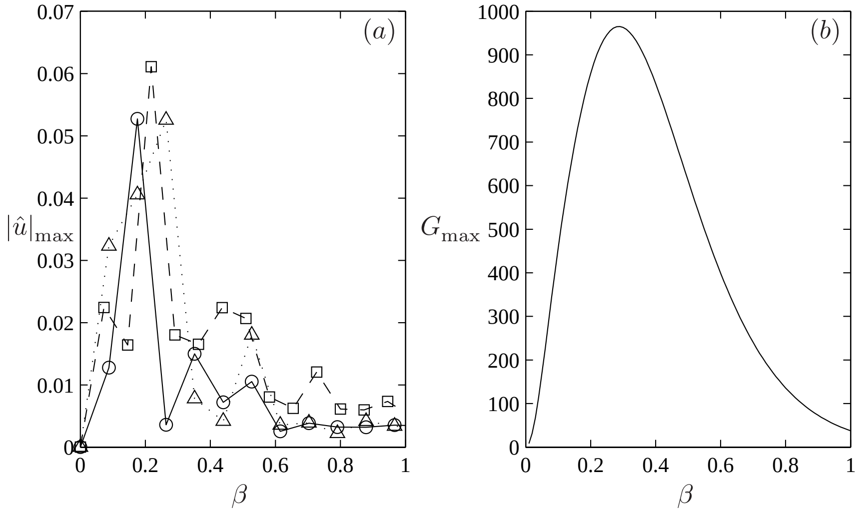

FIGURE 10. (*a*) FFT of three spanwise wave lengths behind arrays of even distributed roughness elements with width (half wave length) 3 mm (○), 2.5 mm (□) and 2 mm (△) from measured streamwise disturbance at $x_1 = 1.55$. (*b*) Computed optimal growth for $\omega = 0$, $x_0 = 0.403$ and $x_1 = 1.55$. $Re_l = 173^2$ is used as the scale factor.

(see figure 12). From the comparison of the computed and experimental optimal spanwise scales in figure 10, it can be observed that the computed scale is somewhat smaller, however close to the observed in the experiment.

In figure 11(*b*), the computed (—) normalized streamwise amplitude distribution at $x_1 = 1.55$ is compared with the measured results. For calculations with different spanwise wave number, β, and initial position, x_0, the shape of the amplitude function is very similar. The similarity between the amplitude functions for the three largest scales in the experiment is also evident in figure 11(*b*). The very good agreement and the fact that the computation contained an optimization procedure while the experiment did not, indicate that a fundamental mode is triggered in the flow. That has also been observed by e.g. Andersson *et al.* (1999) and Westin *et al.* (1994) in the flat-plate boundary layer. These non-modal growth mechanisms are referred to as algebraic growth. In the present work, disturbances are triggered by the surface roughness, however free-stream turbulence is also a possible triggering mechanism, see e.g. Westin *et al.* (1994) for the flat-plate boundary layer results. The optimal disturbance from the computation at $x = 1$ is shown to the left in figure 11 in more detail, where one spanwise wave length of the disturbance is depicted. In figure 11(*a*), the cross-flow velocity components are represented with arrows and in figure 11(*c*), the streamwise velocity is shown as contours. Positive values of disturbance velocity are shown by solid lines and the dashed

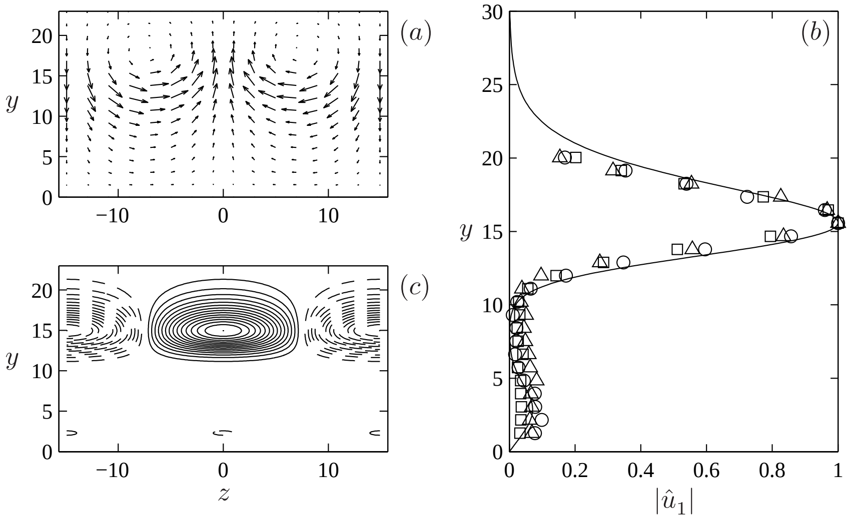

FIGURE 11. Computed optimal disturbance at the cross-flow plane at $x = 1$ for $\beta = 0.211$, $\omega = 0$, $x_0 = 0.403$ and $x_1 = 1.55$. Arrows represent cross-flow velocity components (*a*) and contours show constant positive (—) and negative (− − −) streamwise velocity (*c*). (*b*) Computed final streamwise amplitude velocity distribution (—), normalized with its maximum value, compared with experimental results for $\beta = 0.176$ (○), $\beta = 0.218$ (□) and $\beta = 0.264$ (△).

lines represent negative values. The optimal disturbance consists of streamwise vortices developing into streamwise streaks. At the spanwise location $z = 0$, high-momentum fluid is moved up from the jet core, producing a high-velocity streak in the shear layer region. An opposite motion is observed at the edges of the plot, half a wavelength away, where low-momentum fluid is moved down from the upper velocity field and low-velocity streaks are formed in the shear layer region. Additionally, in the boundary layer region, a weak low-velocity streak is formed below the high-velocity streak at $z = 0$, since the upward motion of fluid there carries low-momentum fluid from the wall region. In a similar way, weak high-velocity streaks are formed in the boundary layer region on the sides. Thus, the more complicated overall character of the disturbance as compared to e.g. the flat-plate boundary layer is explained by rather simple mechanisms, which in general are similar in the single-shear flow of the flat plate and in the wall jet studied here.

4.3. *Towards transition to turbulence*

4.3.1. *Overview of the transition process*

The importance of the three-dimensional effects during flow breakdown is clearly demonstrated by the performed flow visualizations, which are shown in figure 12. Two-dimensional waves were excited by the loudspeaker and can be observed to develop parallel to the nozzle edge. A laser sheet was pulsing, synchronized with the wave frequency while smoke was provided into the inlet of the facility driving fan. With this technique, the flow modulation can be visualized only in the top shear layer, where the difference in the smoke concentration is clear. No special forcing was applied to generate three-dimensional disturbances, which appeared naturally from existing irregularities. Nevertheless, well-defined and nearly uniform streamwise vortices and streaks are visible forming in the flow. In figure 12(*b*), the braid region of the wave is shown, which corresponds to approximately the middle streamwise location of figure 12(*a*). In the braids, the streaks are well pronounced and they attain a typical mushroom shape. Also, moving the visualization plane further from the wall, regions can be reached where streak tips exist, while waves do not. As it is possible to see in figure 12(*a*), the waves are dominating initially and the streaks are rather weak. Further downstream, the streaky structures become dominating. In fact, the current visualizations demonstrate a very similar phenomenon as was observed by Bernal & Roshko (1986) and Lasheras *et al.* (1986) in free shear layers. The streaks in the present case are generated by irregularities in the facility. It is clear that disturbances associated with the streaks are amplified from their upstream origin as the flow develops.

4.3.2. *Spectral analysis*

In the previous section we saw that the role of the initial conditions for the development of the wall jet is essential. To investigate the process of the breakdown in this flow carefully and understand the nonlinear interactions involved, a direct numerical simulation is necessary. A numerical study conducted in a highly controlled environment is free from various uncontrollable parameters, which make the analysis of the experiment difficult, and the numerical results are more straightforward to interpret. Two instability modes, the two-dimensional waves and the streamwise streaks are observed to trigger the breakdown of the wall jet to turbulence. These disturbances were excited in the DNS in a controlled manner, as described in § 3.3.2, and the forcing functions were taken from the previously obtained linear theory computations (see figures 8 and 11). The amplitudes of the waves and streaks were prescribed in the beginning of the computational box to 0.1% and 3% of the wall-jet core velocity, respectively.

The streamwise development of the initially generated modes and the thereafter exited modes of nonlinear interaction can be seen by looking at the development of the Fourier components shown in figure 13. In this figure, the velocity

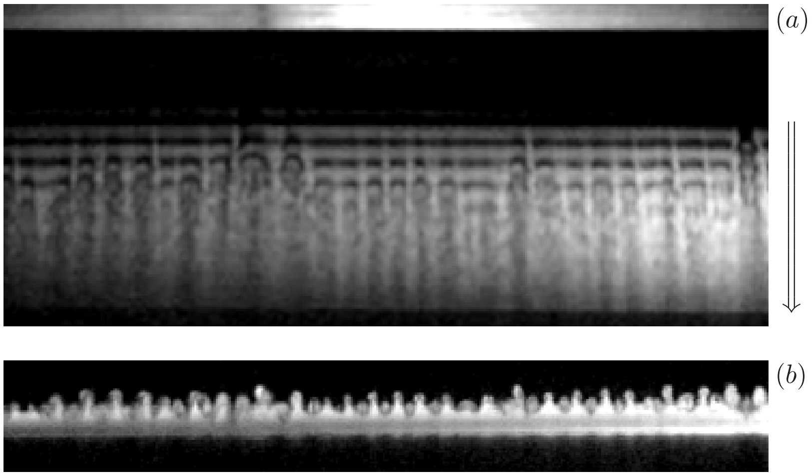

FIGURE 12. Visualization of the nonlinear structures in the wall jet. (*a*) Light sheet is placed parallel to the wall at about 5 mm from it ($y = 30$). The flow direction is down. (*b*) Light sheet is perpendicular to the flow.

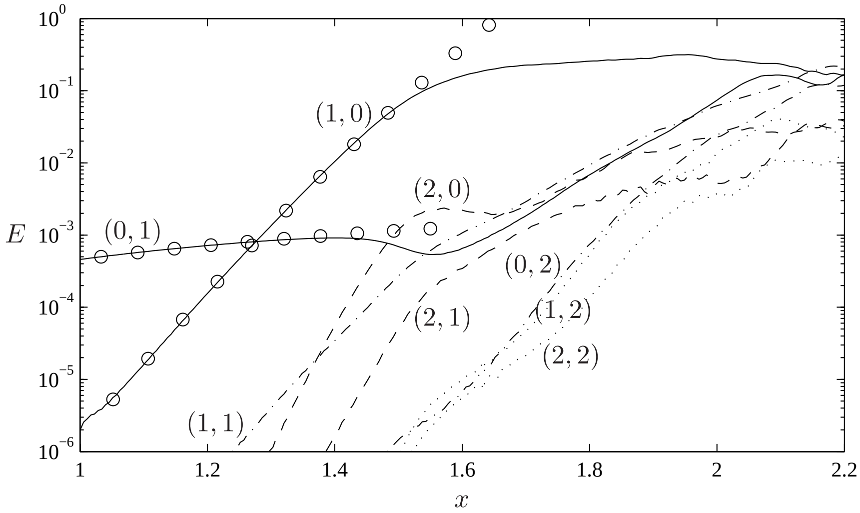

FIGURE 13. Energy in different Fourier modes (ω, β) from the DNS. The initially excited modes (waves and streaks) are shown by solid lines, the nonlinearly generated modes are shown by dashed and dotted lines. The modes are indicated in the figure. Results from the PSE (○) are shown for comparison.

fields are Fourier transformed in time and in the spanwise direction and the notation (ω, β), where ω and β are the frequency and spanwise wavenumber, each normalized with the corresponding fundamental frequency and wavenumber, is used. Thus, the waves and the streaks are represented by $(1, 0)$ and $(0, 1)$, respectively, the solid lines in figure 13. Without nonlinear interactions, the instability modes should amplify in agreement with the linear theory and this is observed in the beginning of the computational box, where the waves grow exponentially and the streaks have an algebraic growth. The results from the PSE ($\circ$) are shown for comparison and the agreement is excellent. The waves grow according to the linear theory for surprisingly large amplitudes while the nonlinear interactions for the streaks is encountered earlier. It is evident that close to the nozzle, the two-dimensional effects are dominating and soon taking over the stronger forced stationary streaks. At about $x = 1.3$ to $x = 1.4$, nonlinear effects start to be apparent when energy is transferred to the modes $(1, 1)$, $(2, 0)$ and $(2, 1)$. Further downstream, the streak mode $(1, 0)$ is decaying and a dip in the energy can be observed at approximately $x = 1.55$. At that location, the time-periodic mode $(1, 0)$ starts to saturate and an abrupt change of the breakdown process happens, namely, an exponential growth of the streak mode.

There are two possible secondary instabilities on two-dimensional vortices generated by inflectional shear flow instabilities, a subharmonic one leading to vortex pairing, and a three-dimensional one leading to spanwise modulation of the vortices, see e.g. Metcalfe *et al.* (1987). In low disturbance environments, the predominant secondary instability is associated with vortex pairing. If the initial three-dimensional excitation is large enough, the three-dimensional secondary instability is predominant. The end result is the growth of a spanwise modulation of the vortices into streamwise vortices and resulting suppression of the vortex pairing. This is what is observed in the current numerical simulation. We have seen that the exponentially growing two-dimensional waves break down due to what appears to be a three-dimensional secondary instability triggered by the presence of the streaks. In order to asses if the pairing mode is present in our simulation, we evaluated the energy content in this subharmonic frequency. In all cases considered, we found evidence of the exponentially growing pairing mode. However, since this mode is not forced (in the fringe), but only grows out of numerical noise, which change with time, the amplitude of this mode is not constant.

4.3.3. *Flow structures*

From the performed numerical simulation, structures appearing in the flow can be visualized and contribute to an increased understanding of the transition process, complementing the above discussion. In figure 14(a), positive and negative isosurfaces of the instantaneous streamwise disturbance velocity are displayed in medium grey and light grey, respectively. Vortical structures can be identified in the flow by plotting regions where the second largest eigenvalue

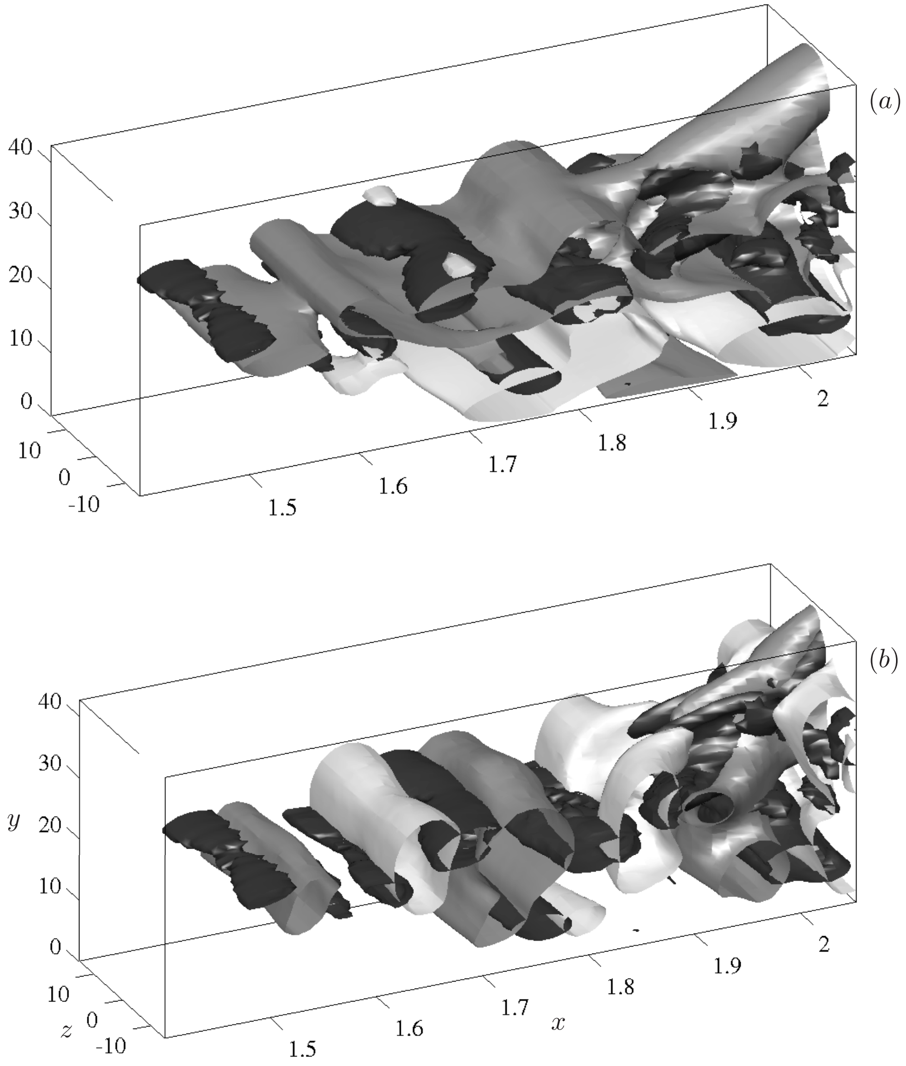

FIGURE 14. Isosurfaces of positive disturbance velocity (medium grey), negative disturbance velocity (light grey) and λ_2 (dark grey). (*a*) Streamwise disturbance velocity. (*b*) Normal disturbance velocity. The waves and streaks are forced with initial amplitudes 0.1% and 3%, respectively, in the Blasius wall jet at $Re_\delta = 173$. The levels of the isosurfaces are 0.15, -0.15 and -0.005, respectively.

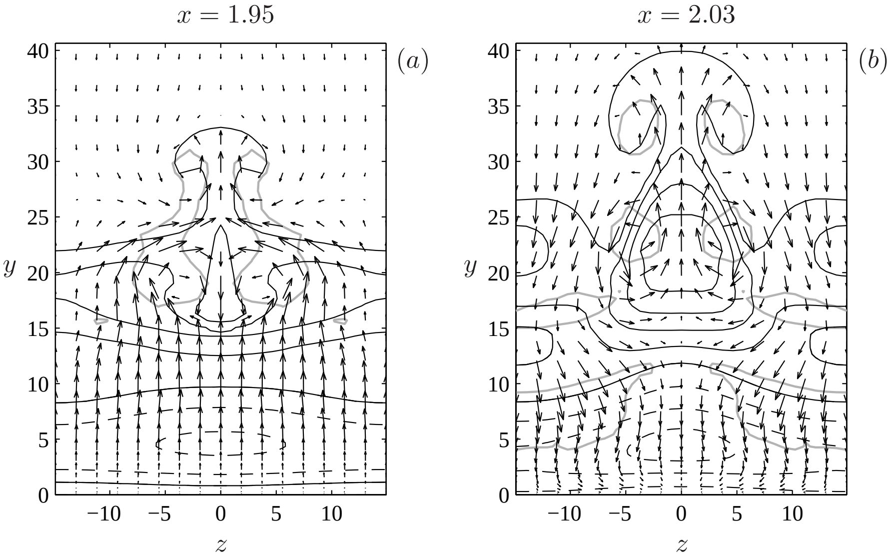

FIGURE 15. Vertical cross-flow planes at two streamwise locations $x = 1.95$ (*a*) and $x = 2.03$ (*b*) for the same flow case as in figures 14. The arrows represent the cross-flow disturbance velocity while the streamwise disturbance velocity is shown by contours of positive (—) and negative (− − −) constant values with spacing of 0.2. The thick grey lines show the core of vortical structures where $\lambda_2 = -0.005$.

λ_2 of the Hessian of the pressure assumes negative values (Jeong *et al.* 1997). The vortical structures in figure 14 are represented by dark grey isosurfaces displaying a constant negative value of λ_2. The corresponding visualization for the wall-normal disturbance velocity is depicted in figure 14(*b*). At the instantaneous moment shown in the figures, the waves are most pronounced in the beginning of the box, which shows the highly nonlinear region where the waves already have started to saturate. At about $x = 1.9$, the high-velocity streak becomes dominant and is lifted up from the shear layer region forming a mushroom-shaped structure. Such structures were also observed by e.g. Wernz & Fasel (1996, 1997) and Gogineni & Shih (1997). Additional details of the visualization of the nonlinear interaction between the streaks and the waves in that region are shown in figure 15 by two cross-flow slices. In this figure, the arrows represent the cross-flow disturbance velocity while the streamwise disturbance velocity is shown by contours of positive (—) and negative (− − −) constant values. The thick grey lines show the core of vortical structures at the same level as figures 14. The coincidence of the numerical visualization with the experimental visualizations of figure 12 is remarkable. Namely, it is obviously seen that in the outer region of the wall jet, the large amplitude streak structures dominate the late stage of flow breakdown. Both in the computations (figure 15(*b*)) and in the experiments (figure 12(*b*)), a staggered formation of streaks can be observed. The strong three-dimensionality is formed only a certain distance from the nozzle outlet. An other interesting phenomenon is observed close to the wall, in the boundary layer region of the flow. It can be seen that strong vortical motion of the outer region of the wall jet induces vortices near the wall as well. This demonstrates the interaction of the inner and outer regions of the wall jet and the interaction takes place both for two- and three-dimensional motion. Furthermore, the two layers of the wall jet exhibit interaction down to the latest stages of the breakdown.

5. Summary and conclusion

The dynamics of a plane wall jet has been studied and the theory and numerical simulation were compared with experimental studies. It was found that a laminar wall jet can be successfully described by the solution of the boundary layer equations. This solution, the so-called Blasius wall jet, which was matched to the experimental data, is valid in the nearby downstream field of the nozzle in contrast to the well-known Glauert similarity solution. The linear stability mechanism of the wall jet was investigated theoretically and experimentally. Comparison of the results of the linear stability calculations with the experiment shows that the linear stability theory is able to predict the most amplified frequency of the periodical waves and the most amplified scale of the streaks. The agreement between the computed eigenmodes and the measured waves is very good apart from the upper part of the shear layer, where the difference in the theoretical and experimental base flows and the fact that the measured waves not are fully developed eigenmodes, causes a deviation. Furthermore, linear stability theory demonstrates a rather high instability of the flow to non-modal streaks and it seems that this mechanism is responsible for the generation of initial three-dimensionality of the jet breakdown. An additional support of this conclusion is an excellent agreement of the theoretical and experimental amplitude functions of the streak. An optimal, most amplified scale exists for the stationary streaks as it was observed both in the theory and the experiment. The theory indicates that the optimal disturbances represent streamwise vortices, which cause the formation of streaks by the so-called lift-up effect.

Finally, the nonlinear stage of the laminar flow breakdown is studied with DNS and experimentally visualized. The three-dimensional simulations with coherent forcing are performed and the simulation clearly demonstrates that growing streaks are important for the breakdown process. It was found that the forcing of streamwise streaks feed into the three-dimensional secondary instability preceding the flow breakdown. As a result, the three-dimensionalities in the flow is enhanced and the other possible secondary instability of the flow, namely the subharmonic pairing of the vortices, is suppressed. As both the experiment and simulation show, a very strong amplification of streaks occurs at the stage of the nonlinear interaction between the streaks and the two-dimensional waves. The high-velocity streaks are lifted up from the shear layer and form mushroom-shaped structures appear. It was also observed that an interaction of the inner and outer regions of the wall jet takes place down to the latest stages of the breakdown. However, a detailed study of the nonlinear interaction and wall-jet flow structures is beyond the scope of the work in this paper and motivates a continuing research.

This work was funded by the Swedish Energy Agency (Energimyndigheten). Many thanks to Mattias Chevalier for the help with various modifications of the spectral code and to Professor Victor Kozlov for the help with the smoke visualizations and for the loan of the laser.

Appendix. Optimization procedure

In this appendix, the optimization procedure for the optimal disturbances in the algebraic instability problem is derived. We adopt an input-output formulation of the initial-boundary-value problem (2–7)

$$\hat{u}_1 = \mathcal{A}\boldsymbol{q}, \tag{29}$$

where $\mathcal{A}$ is a linear operator. The maximum Reynolds-number-independent growth may then be written

$$\overline{G}_{\max} = \max_{\boldsymbol{q}\neq 0} \frac{(\hat{u}_1, \hat{u}_1)_u}{(\boldsymbol{q}, \boldsymbol{q})_q} = \max_{\boldsymbol{q}\neq 0} \frac{(\mathcal{A}^*\mathcal{A}\boldsymbol{q}, \boldsymbol{q})_q}{(\boldsymbol{q}, \boldsymbol{q})_q}. \tag{30}$$

Here $\mathcal{A}^*$ denotes the adjoint operator to $\mathcal{A}$ with respect to the chosen inner product. The maximum of $(\mathcal{A}^*\mathcal{A}\boldsymbol{q}, \boldsymbol{q})/(\boldsymbol{q}, \boldsymbol{q})$ is attained for some vector $\boldsymbol{q}$, which is the eigenvector corresponding to the largest eigenvalue of the eigenvalue problem

$$\mathcal{A}^*\mathcal{A}\boldsymbol{q} = \lambda\boldsymbol{q}, \tag{31}$$

where $\overline{G}_{\max}$ is the maximum eigenvalue $\lambda_{\max}$, necessarily real and non-negative. The most natural attempt to calculate the optimal initial disturbance and its associated maximum Reynolds-number-independent growth is by power iterations

$$\boldsymbol{q}^{n+1} = \mathcal{A}^*\mathcal{A}\boldsymbol{q}^n, \tag{32}$$

where the initial disturbance is scaled to the given initial energy in each iteration. To be able to perform the power iterations, we need to know the action of the adjoint operator on $\hat{u}_1$. The following adjoint system can be derived from (2–7) with $\alpha = 0$ and $\hat{p}_x = 0$, by integration by parts

$$-v_y^* + \mathrm{i}\beta w^* = 0, \tag{33}$$

$$-\mathrm{i}\omega u^* - U u_x^* - V_y u^* - V u_y^* + V_x v^* - p_x^* = u_{yy}^* - \beta^2 u^*, \tag{34}$$

$$-\mathrm{i}\omega v^* - U v_x^* - U_x v^* - V v_y^* + U_y u^* - p_y^* = v_{yy}^* - \beta^2 v^*, \tag{35}$$

$$-\mathrm{i}\omega w^* - U w_x^* - V w_y^* + \mathrm{i}\beta p^* = w_{yy}^* - \beta^2 w^*, \tag{36}$$

where $p^*(x,y)$, $u^*(x,y)$, $v^*(x,y)$ and $w^*(x,y)$ are the adjoint variables with boundary conditions

$$\begin{cases} \overline{u}^* = \overline{v}^* = \overline{w}^* = 0 & \text{at} \quad y = 0, \\ \overline{u}^* = \overline{w}^* = \overline{p}^* + 2V\overline{v}^* = 0 & \text{at} \quad y = y_{\max}. \end{cases} \tag{37}$$

The x-derivative in the parabolic set of equations (33–36) has opposite sign compared to (2–5) and has to be solved in the backward direction from the final position x_1 to the initial position x_0. Therefore the initial condition is specified at x_1

$$\begin{cases} U_1 u_1^* + p_1^* = \hat{u}_1(y) & \text{at} \quad x = x_1, \\ v_1^* = w_1^* = 0 & \text{at} \quad x = x_1. \end{cases} \tag{38}$$

The action of the adjoint operator is given by

$$\begin{cases} \hat{v}_0 = U_0(y) v_0^*(y) & \text{at} \quad x = x_0, \\ \hat{w}_0 = U_0(y) w_0^*(y) & \text{at} \quad x = x_0. \end{cases} \tag{39}$$

The adjoint-based optimization algorithm is very efficient and converges often within three to four iterations, indicating the existence of a well-separated dominating mode.

References

Amitay, M. & Cohen, J. 1993 The mean flow of a laminar wall-jet subjected to blowing or suction. *Phys. Fluids A* **5** (8), 2053–2057.

Amitay, M. & Cohen, J. 1997 Instability of a two-dimensional plane wall jet subjected to blowing or suction. *J. Fluid Mech.* **344**, 67–94.

Andersson, P., Berggren, M. & Henningson, D. 1999 Optimal disturbances and bypass transition in boundary layers. *Phys. Fluids* **11** (1), 134–150.

Bajura, R. A. & Catalano, M. R. 1975 Transition in a two-dimensional plane wall jet. *J. Fluid Mech.* **70** (4), 773–799.

Bajura, R. A. & Szewczyk, A. A. 1970 Experimental investigation of a laminar two-dimensional plane wall jet. *Phys. Fluids A* **13** (7), 1653–1664.

Balaras, E., Piomelly, U. & J.M., W. 2001 Self-similar states in turbulent mixing layers. *J. Fluid Mech.* **446**, 1–24.

Bernal, L. P. & Roshko, A. 1986 Streamwise vortex structure in plane mixing layers. *J. Fluid Mech.* **170**, 499–525.

Bertolotti, F. P., Herbert, T. & Spalart, P. R. 1992 Linear and nonlinear stability of the Blasius boundary layer. *J. Fluid Mech.* **242**, 441–474.

Brandt, L. & Henningson, D. S. 2002 Transition of streamwise streaks in zero-pressure-gradient boundary layers. *J. Fluid Mech.* **472**, 229–261.

Chernoray, V. & Löfdahl, L. 2003 A hot wire visualization study of K-type breakdown in adverse pressure gradient boundary layer. *Exps. Fluids* To appear.

Chun, D. H. & Schwarz, W. H. 1967 Stability of the plane incompressible viscous wall jet subjected to small disturbances. *Phys. Fluids A* **10** (5), 911–915.

Cohen, J., Amitay, M. & Bayly, B. J. 1992 Laminar-turbulent transition of wall-jet flows subjected to blowing and suction. *Phys. Fluids A* **4** (2), 283–289.

Glauert, M. B. 1956 The wall jet. *J. Fluid Mech.* **1**, 625–643.

Gogineni, S. & Shih, C. 1997 Experimental investigation of the unsteady structure of a transitional plane wall jet. *Experiments in Fluids* **23**, 121–129.

Gogineni, S., Shih, C. & Krothapalli, A. 1993 PIV study of a two-dimensional transitional wall jet. *AIAA Paper* 93-2913.

Gogineni, S., Visbal, M. & Shih, C. 1999 Phase-resolved PIV measurements in a transitional plane wall jet: a numerical comparison. *Experiments in Fluids* **27**, 126–136.

Hanifi, A., Schmid, P. & Henningson, D. 1996 Transient growth in compressible boundary layer flow. *Phys. Fluids* **8** (3), 826–837.

Herbert, T. 1997 Parabolized stability equations. *Annu. Rev. Fluid Mech.* **29**, 245–283.

Ho, C. & Huerre, P. 1984 Perturbed free shear layers. *Annu. Rev. Fluid Mech.* **16**, 365–424.

Jeong, J., Hussain, F., Schoppa, W. & Kim, J. 1997 Coherent structures near the wall in a turbulent channel flow. *J. Fluid Mech.* **332**, 185–214.

Klebanoff, P. 1971 Effect of freestream turbulence on the laminar boundary layer. *Bull. Am. Phys. Soc.* **10**, 1323.

Lasheras, J. C., Cho, J. S. & Maxworthy, T. 1986 On the origin and evolution of streamwise vortical structures in a plane, free shear layer. *J. Fluid Mech.* **172**, 231–258.

Levin, O. & Henningson, D. S. 2003 Exponential vs algebraic growth and transition prediction in boundary layer flow. *Flow, Turbulence and Combustion* To appear.

Lundbladh, A., Berlin, S., Skote, M., Hildings, C., Choi, J., Kim, J. & Henningson, D. S. 1999 An efficient spectral method for simulation of incompressible flow over a flat plate. *Tech. Rep.*. KTH, Department of Mechanics, Stockholm.

Mele, P., Morganti, M., Scibilia, M. & Lasek, A. 1986 Behavior of wall jet in laminar-to-turbulent transition. *AIAA Journal* **24** (6), 938–939.

Metcalfe, R. W., Orszag, S. A., Brachet, M. E., Menon, S. & Riley, J. J. 1987 Secondary instability of a temporally growing mixing layer. *J. Fluid Mech.* **184**, 207–243.

Monkewitz, P. A. & Huerre, P. 1982 Influence of the velocity ratio on the spatial instability of mixing layers. *Phys. Fluids* **25** (7), 1137–1143.

Nordström, J., Nordin, N. & Henningson, D. S. 1999 The fringe region technique and the fourier method used in the direct numerical simulation of spatially evolving viscous flows. *SIAM J. Sci. Comput.* **20** (4), 1365–1393.

Schlichting, H. 1979 *Boundary-Layer Theory*, 7th edn. Mc-GRAW HILL.

Seidel, J. & Fasel, H. F. 2001 Numerical investigations of heat transfer mechanisms in the forced laminar wall jet. *J. Fluid Mech.* **442**, 191–215.

Tumin, A. & Aizatulin, L. 1997 Instability and receptivity of laminar wall jets. *Theoret. Comput. Fluid Dynamics* **9**, 33–45.

Visbal, M. R., Gaitonde, D. V. & Gogineni, S. P. 1998 Direct numerical simulation of a forced transitional plane wall jet. *AIAA Paper* 98-2643.

Wernz, S. & Fasel, H. F. 1996 Numerical investigation of unsteady phenomena in wall jets. *AIAA Paper* 96-0079.

Wernz, S. & Fasel, H. F. 1997 Numerical investigation of forced transitional wall jets. *AIAA Paper* 97-2022.

Westin, K., Boiko, A., Klingmann, B., Kozlov, V. & Alfredsson, P. 1994 Experiments in a boundary layer subjected to free stream turbulence. Part 1. Boundary layer structure and receptivity. *J. Fluid Mech.* **281**, 193–218.